Dual Antenna Design for a Novel Airborne Probe

by

Johnathon Craig Prather

A thesis submitted to the Graduate Faculty of
Auburn University
in partial fulfillment of the
requirements for the Degree of
Master of Science

Auburn, Alabama
December 10, 2016

Keywords: Antenna, PIFA, HFSS

Approved by

Mark Adams, Chair, Assistant Professor of Electrical and Computer Engineering
Stuart Wentworth, Associate Professor of Electrical and Computer Engineering
Lloyd Riggs, Professor of Electrical and Computer Engineering

Abstract

This work outlines the design, simulation, and testing of a dual antenna design for a novel airborne probe. The airborne probe is known as the Global Sense eMote and is designed to collect in-situ atmospheric data and transmit the data back to a receiver base station. The eMote operates in the industrial, scientific, and medical band, 902 – 928 MHz. The eMote is designed to replace the larger, more costly current environmental data collection devices currently on the market. The final antennas designed were two planar inverted-F antennas on a compact, circular FR-4 printed circuit board. This work outlines the methodologies used to select and design the antennas. The antennas were simulated and designed in ANSYS HFSS and ANSYS Electronics Desktop. The fabricated antennas were then tested to determine how well their performance correlated with the simulated antennas. The antennas did not perform as well as the simulation implied so the causes were determined and the process to extract the differences was detailed. Finally, potential antenna improvements and future work are presented.

Contents

List of Figures

<div align="center">List of Tables</div>

List of Abbreviations

Γ Reflection coefficient

λ Wavelength

CAD   Computer Aided Design

COTS   Commercial Off-the-Shelf

CP   Circularly Polarized.

dB   Decibels

DUT   Device Under Test

ESA   Electrically Small Antenna

FCC   Federal Communications Commission

FEC   Forward Error Correction

GPS   Global Positioning System

HFSS   High Frequency Simulation Solver

ISM   Industrial Scientific and Medical

PCB   Printed Circuit Board

RHCP   Right-Hand Circularly Polarized.

SOTA   State-of-the-Art

Chapter 1

Introduction

In contemporary society, evolving communications systems drive a constant need for more advanced antenna designs. Often, antennas must be miniaturized to be used in compact devices where there is often little space to spare. These compact antennas are called electrically small antennas, ESA, as their physical dimensions are smaller than a typical antenna design which is often a significant fraction of the free space wavelength, in size, at the design frequency.

1.1 Design Justification

Atmospheric researchers have come to rely heavily on remote sensing technologies such as satellites and radar to monitor and predict the weather. However, additional in-situ measurements are needed to improve weather models and create more accurate forecasts. Current in-situ measurements for hurricane reconnaissance primarily rely on devices known as dropsondes. The dropsondes have a terminal velocity of 11 m/s at sea level, and approximately 21 m/s at a 12 km altitude [1]. For more quiescent conditions, weather balloons carrying radiosondes [2] are launched around the globe every day to measure the properties of the atmosphere.

There is a need to make smaller, cheaper devices that can be employed in larger numbers to make these measurements. One of the major complications with making these devices smaller is the limitation in appropriate antenna designs. This is the driving force for the antenna design process presented in this thesis.

1.1.1 Global Sense eMote

The antennas were designed for a device known as an environmental mote or eMote. The project is known as the GlobalSense eMote and it is a continuation of the work started by Dr. John Manobianco [3, 4] for large scale environmental sensing. The device is designed as a small, light-weight, <8 g, energy-efficient, environmental probe. The eMote will collect ambient data from pressure, temperature, and humidity sensors along with GPS position and velocity information and will then transmit this data back to a receiver base station. The base station will be configured to collect data from more than a hundred eMotes simultaneously. The eMote is designed to have a low terminal velocity <5 $\frac{m}{s}$ which provides greater dwell time in the atmosphere. The low-mass and slower terminal velocity ensure that the eMote will not damage any objects that it interacts with. The final design goal is to have a device with a mass of ≤1 g and a terminal velocity ≤1 $\frac{m}{s}$. It is designed for varied weather environments and can be deployed from either the ground via balloon or dropped from an aircraft, manned or unmanned. A CAD drawing of the eMote can be seen in Figure 1.1.
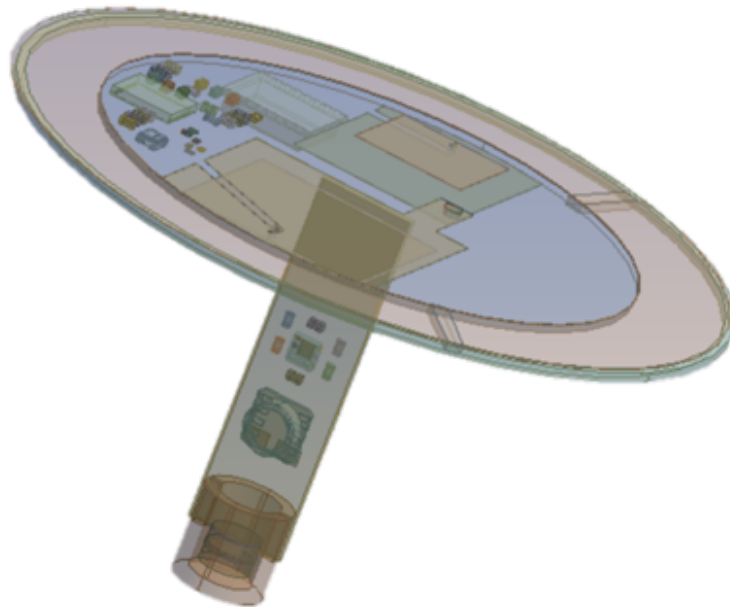
Figure 1.1: CAD drawing of the eMote

In Figure 1.1, one can see the eMote is a cap-and-stem design. The stem contains the sensors, currently Sensirion's SHT25 and Measurement Specialties's MS5803-01BA07, and the batteries. The cap contains the microcontroller and GPS receiver which are Texas Instrument's CC430F5137 and U-blox's MAX-M8Q, respectively. The cap also contains the designed microstrip antennas and supportive passive components. The sensors communicate with the microcontroller via the inter-integrated circuit, I^{2}C, communication protocol so the stem and components can easily be interchanged. The eMote has two antennas where one is a GPS L1 band antenna and the other is an antenna tuned to the 915 MHz industrial, scientific, and medical radio, ISM, band. The eMote will transmit at a low power in the ISM band so it will not require FCC licensing. The work presented in this thesis primarily focuses on the antenna design.

1.2   Research Methodology

The problem solving approach began with a review of current commercial off-the-shelf components and a review of the state-of-the-art in antenna literature. When it was noted that ideal commercial off-the-shelf components did not exist, a literature review was started. Following this review, the most applicable antenna design techniques were then modified to match the operational frequencies and desired substrate size. These designs were then simulated in ANSYS's HFSS v.15 [5] and Electronics Desktop [6] in an iterative fashion until they were tuned to the design frequency and the most promising options were then pursued. Intermediate designs were fabricated in-house using an LPKF ProtoMat S62 [7]. The final design was then manufactured by a boardhouse and tested in-house. The in-house test equipment was comprised of a network analyzer, Keysight FieldFox N9918A [8], and a spectrum analyzer, Tektronix RSA306B [9]. Antennas were connected to the network analyzer to measure network parameters and the voltage standing wave ratio, VSWR. Then the antennas were tested in an anechoic chamber utilizing the spectrum analyzer. Figure 1.2 presents a flowchart of the research methodology.
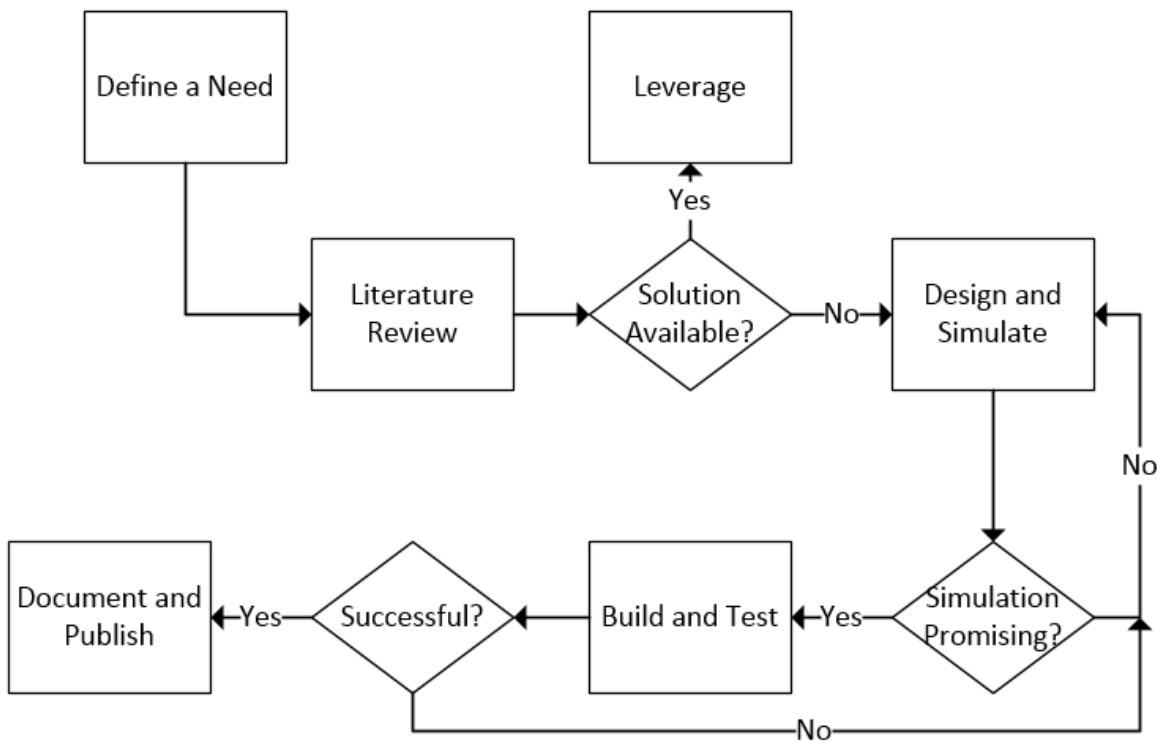
Figure 1.2: Flowchart of Research Methodology

Chapter 2

Background

2.1 Antenna Parameters

For a given antenna application, performance criteria must be established to validate a successful design. This chapter outlines the parameters of interest to the validation criteria. Since there are a multitude of antenna designs, the criteria will not be the same for all valid designs. Several of the more prominent parameters are discussed in this section. For a more detailed discussion on basic electromagnetic principles see Wentworth [10], Arthur [11], or Inan, Inan, and Said [12].

2.1.1 S-parameters

Unlike relatively low frequency systems, it becomes increasingly difficult to measure voltages and currents of systems as the frequency increases since direct measurements involve the magnitude and phase of the traveling or standing wave [13]. Since these measurements become progressively more difficult to infer, it is convenient to discuss the network parameters as scattering parameters or S-parameters. S-parameter measurements employ easily realizable matched loads for characterization [10]. Scattering matrices are often used to characterize multiport networks, particularly at high frequencies, and as such are useful ways to characterize microwave components such as amplifiers, circulators, and oscillators. S-parameters can be easily related to the concepts of reflection, gain, loss, and isolation [10]. The equation below shows the scattering matrix for a two port network.

Equation 2.1 *Two port scattering matrix*

$$\begin{bmatrix} V_1^- \\ V_2^- \end{bmatrix} = \begin{bmatrix} S_{11} & S_{12} \\ S_{21} & S_{22} \end{bmatrix} \begin{bmatrix} V_1^+ \\ V_2^+ \end{bmatrix}$$

Equation 2.2 *Abbreviated two port scattering matrix*

$$\begin{bmatrix} V \end{bmatrix}^- = \begin{bmatrix} S \end{bmatrix} \begin{bmatrix} V \end{bmatrix}^+$$

A S-parameter, S_{ab}, is defined as the fraction of the voltage entering port b that exits port a [10]. For the purposes of antenna design, there are two S-parameters that are of particular interest. One S-parameter that is critical to the design of an antenna is S_{11}. This term, S_{11}, is the same as the reflection coefficient for a single port system, such as an antenna. The reflection coefficient can be defined as the amount of the electromagnetic wave that is reflected due to an impedance mismatch. The derivation can be seen below. Γ is the reflection coefficient which is defined in terms of characteristic impedance, Z_0, and load impedance, Z_L.

Equation 2.3 *Reflection Coefficient*

$$\Gamma = \frac{Z_L - Z_0}{Z_L + Z_0}$$

The load impedance can be calculated in terms of S_{11} and characteristic impedance.

Equation 2.4 *Impedance of Load*

$$Z_L = \frac{1 + S_{11}}{1 - S_{11}} Z_0$$

Equation 2.5 S_{11} *for a one port network*

$$S_{11} = \frac{Z_L - Z_0}{Z_L + Z_0} = \Gamma$$

By the conservation of energy, the power that is not transmitted is either transferred to heat, resistive loss, or radiated by the antenna. S-parameters are typically represented in dB. S_{11} values of less than -6 dB are commonly used to define the effective bandwidth of an antenna. The other S-parameter of interest to this dual antenna design is S_{12} or S_{21}. This parameter shows the isolation between the antennas. The lower the value at the frequency of interest, the better the isolation is between devices. A value below -30 dB is defined as well isolated.

The parameters are measured using network analyzers. For S_{11} measurements, a single port is measured. This is accomplished by connecting a single port of a carefully calibrated network analyzer to the device under test. For S_{12} or S_{21} measurements, the network analyzer undergoes a careful calibration on both ports. The two ports are then connected to the two ports of the device under test, for this thesis both antennas, and then the parameters are calculated.

2.1.2   VSWR

The voltage standing wave ratio (VSWR) is "superposition of the incident and reflected waves" [10] that creates a standing wave pattern.

Equation 2.6 *Extrema of Vmax*

$$V_{max} = 1 + |\Gamma_L|$$

$$V_{min} = 1 - |\Gamma_L|$$

The ratio of the maximum and minimum amplitudes is the voltage standing wave ratio.

Equation 2.7 *VSWR Definition*

$$VSWR = \frac{V_{max}}{V_{min}} = \frac{1 + |\Gamma_L|}{1 - |\Gamma_L|}$$

The magnitude of the reflection coefficient, Γ_L, can range from 0 to 1, therefore VSWR can range from 1 to infinity. This parameter is used, similar to S_{11}, to calculate the effective bandwidth of the designed antenna. The ideal value for the VSWR is at or near 1 indicating very little reflected wave. For an antenna, this means most of the power is being radiated. The antenna is typically deemed to operate in the desired frequency band if the VSWR is less than 3.

2.1.3 Radiation Pattern

A radiation pattern, or antenna pattern, is used to visualize how an antenna radiates in a 3 dimensional space. The radiation pattern is often denoted as the far-field pattern as it is the representation of the far-field radiation properties. It does not include the near-field reactive properties. The typical analogy used to describe the radiation pattern is a ball of modeling clay [14]. A perfect sphere of modeling clay would represent an isotropic radiation pattern because it radiates the same in all directions. If the sphere is squeezed without adding or removing any clay, then a new pattern is created through the distortion of the clay. To continue the analogy, there is the same amount of clay, but there is more in certain areas than others. Similarly, for an antenna, the total power radiated is the same, but there is more power density in certain areas than others. The radiation pattern can be expressed in the electric field, E-plane, or the magnetic field, H-plane. The H-plane and E-plane are perpendicular to one another. Figure 2.1 shows the 3 dimensional and 2 dimensional radiation pattern of an antenna simulated in HFSS.
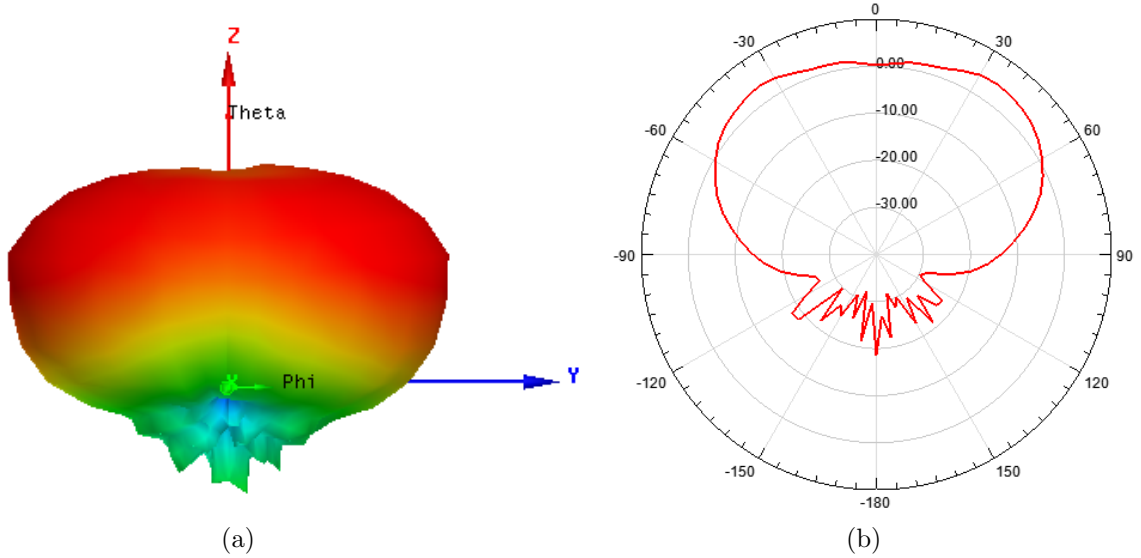
Figure 2.1: Simulated Antenna Patterns (a) 3D Plot (b) 2D Polar Plot

2.1.4 Directivity and Gain

The directivity of an antenna can be defined as how much the antenna concentrates its radiated energy in a preferred direction, or as defined by Stutzman: "the ratio of the radiation intensity in a certain direction to the average radiation intensity" [14]. When the directivity of an antenna is discussed, it is typically defined as the direction of maximum radiation. Directivity of an antenna would be equal to gain if the antenna was a perfectly efficient radiator. In order to properly define directivity of an antenna, the beam solid angle, Ω_A, has to be defined.

Equation 2.8 *Beam Solid Angle*

$$\Omega_A = \int\int_{sphere} |F(\theta,\phi)|^2 d\Omega$$

The beam solid angle is the surface integral of the radiation pattern, $F(\theta,\phi)$. The radiation pattern is the angular variation of radiation around the antenna [14]. This includes directional patterns, shaped main beams, and omnidirectional patterns.

Equation 2.9 *Directivity*

$$D = \frac{4\pi}{\Omega_A}$$

Directivity is dependent entirely on the shape of the radiation pattern. To find the directivity as a function of the pattern angle, the directive gain is used. The maximum value of $|F(\theta, \phi)|$ is unity, the maximum value of directivity as a function of the angle is D [14].

Equation 2.10 *Directive Gain*

$$D(\theta, \phi) = D|F(\theta, \phi)|^2$$

Unlike directivity, gain is defined by more than just the radiation pattern of the antenna. Gain is defined as the amount of power radiated in a certain direction compared to the amount of power radiated by a perfect isotropic radiator. This takes into account the efficiency and directivity of the antenna. Gain measurements of an antenna do not typically take into account the impedance mismatch or the polarization mismatch [14]. Gain can can be empirically defined as:

Equation 2.11 *Gain*

$$G = \frac{4\pi U_m}{P_m}$$

where U_m and P_m are the maximum radiation intensity and the net power accepted by the antenna from the transmitter [14]. When a direction is not given, the gain of an antenna is typically stated as the maximum gain.

Most antennas are highly efficient radiators, with the exception of electrically small antennas. Radiation efficiency e_r is between 0 and 1 and is defined in Equation 2.12.

Equation 2.12 *Radiation Efficiency*

$$e_r = \frac{P_{radiated}}{P_{input}}$$

Since electrically small antennas are not as efficient radiators, the radiation efficiency must be considered when calculating gain. Therefore, the gain can be approximated as the radiation efficiency multiplied by the directivity [14].

Equation 2.13 *Gain*

$$G = e_r D$$

The values for the gain and directivity of an antenna are typically expressed with the unit dB. For an antenna, they are calculated as the gain or directivity relative to an ideal isotropic radiator (dBi), but are generally just shortened to dB.

2.2 Microstrip Antennas

A popular electrically small antenna is the microstrip, or patch, antenna. This type of antenna is commonly a thin strip of copper on a printed circuit board, PCB, substrate. Since the radiating element is on the substrate, the intrinsic parameters of the substrate modify the behavior of the radiating element. The permittivity, ϵ_r, called by boardhouses and manufacturers the "dielectric constant, D_k," is a critical parameter to the design of a microstrip antenna. Typical permittivity values of PCB substrates range from 1 to 10 depending on the material, and the permittivity of air is approximately 1. The effective wavelength of the antenna depends on the permittivity of the substrate. Increasing the permittivity of the substrate decreases the effective wavelength which leads to a decrease in the size of a microstrip patch antenna. However, increasing the permittivity will decrease the bandwidth of the antenna if the other design factors are held constant. The bandwidth reduction can be compensated for by increasing the thickness of the substrate [14]. Further decreases in the resonant frequency can be obtained by increasing the permeability of the substrate, up to 30% [15], but higher permeability substrates are not as readily available for PCB design. The choice of substrate type and permittivity provides the antenna designer with another parameter to modify in the antenna design process. A precise value of ϵ_r is

needed to allow optimal antenna design. A method for measuring ϵ_r is described in Section 4.2.

There are many common designs and variations of the microstrip antenna. The simplest design is the $\frac{\lambda}{2}$ rectangular patch [10]. This is a simple design that is easy to implement. More complex designs often necessitate the use of a modeling software [10] such as ANSYS's HFSS or Keysight's Momentum 3D Planar EM Simulator [16]. An antenna simulated in Keysight's Momentum software is shown in Figure 2.2. The current intensities are shown on the antenna where red is the most intense and blue is the least intense.
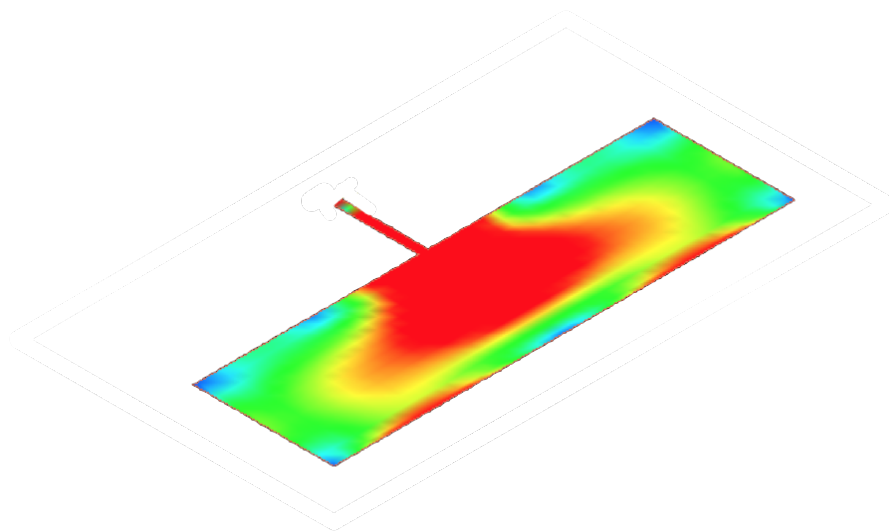
Figure 2.2: $\frac{\lambda}{2}$ Microstrip Patch Antenna Simulated in Keysight's Momentum

2.3 ESA

An electrically small antenna, ESA, is defined as an antenna that is contained within a sphere of radius $\leq 0.16\lambda$ [14]. ESAs have several shortcomings which include poor directivity, large input resistance and reduced radiation efficiency. When size is not a critical issue, it is preferable to create a resonant sized antenna. When size is a driving issue, then an ESA must be considered even though it is less efficient. Careful design of a feeding structure can minimize the issues encountered with the high input resistance typical to an electrically

small antenna. When using an ESA, the designer has to consider the losses associated with the lower radiation efficiency compared to resonant antenna designs.

2.4 The Design Frequency Bands

2.4.1 GPS

The GPS antenna was designed to operate at the GPS L1 band which is centered at 1575.42 MHz [17]. This band was chosen over the L2C centered at 1227.60 MHz [17] and L5C centered at 1176.45 MHz [18] bands as it is the highest frequency band provided, which leads to a smaller final antenna design. Choosing this frequency provides an additional benefit as it is commonly used and there are many commercial off-the-self receivers available.

The bandwidth of the L1 band is 20.46 MHz centered at 1575.42 MHz. Therefore, the antenna needs to be resonant between 1565.17 and 1585.63 MHz [17]. The GPS L1 signal is right hand circularly polarized, RHCP [17] so any system designed to receive GPS L1 frequencies will need a RHCP antenna or accept the the loss due to a polarization mismatch. The loss due to a linearly polarized antenna receiving a circularly polarized signal is 3 dB [19].

2.4.2 ISM

The FCC offers several unlicensed industrial, scientific, and medical, ISM, bands where users can transmit without seeking licensing if the output is sufficiently low [20]. The ISM band that the eMote system was designed to use is the $902 - 928$ MHz band. For the ISM band transmission, the output of a spread spectrum has to be less than 1 mW (FCC regulation 15.247) [21]. The antenna must be fixed to the system and cannot be replaced with another antenna after the device has been verified to meet the transmitting requirements. The unlicensed ISM systems are provided no regulatory protection from interference. The maximum field strength at 3 meters is 50 $\frac{mV}{m^2}$ for quasi-peak measurements with the harmonics below $500\frac{\mu V}{m^2}$ (FCC regulation 15.249) [21].

2.5   Literature Review

At the onset of the project, a literature review of the state of the art research was completed as there are no commercial-off-the-shelf small antennas available that would fit the needs of this design. Several textbooks were referenced [10, 14, 22, 23] initially to verify the fundamental understanding of electromagnetics and the antenna design process. In the texts, there were several types of antennas referenced that led to the begining of the design process. The first antenna types researched and simulated were the basic $\frac{\lambda}{2}$ [14] and $\frac{\lambda}{4}$ [24] patch antennas. These designs were quickly ruled out because of the large area required for both ground plane and patch element; therefore, this research focused on finding a smaller antenna to minimize the mass and size of the board.

The preliminary design focused on a RHCP GPS L1 band antenna. The first such antenna investigated was the circularly polarized, CP, microstrip antenna by Hisao Iwasaki [25]. This antenna design did not radiate at the correct frequency and had a small bandwidth. It was deemed, based off of the research presented in the paper, that modifying the operating frequency of the antenna would not provide a large enough bandwidth for successful GPS operation. Similarly, other designs did not have a large enough circularly polarized bandwidth [26, 27, 28]. Research shifted to antennas with a sufficiently large bandwidth for operation. Antennas were considered that did not operate at the desired frequency, as modifications could be made to the antennas to change the resonant frequency. Several designs were found, but most were either too large [29, 30, 31, 32], used special substrate structures not practical for manufacturing [33, 34], or had large air-gaps difficult to implement in an airborne probe [35, 36]. The final design that had the best compromise of bandwidth, ease of fabrication, and practicality was the antenna designed by Chen [37]. Chen's design was not resonant at the GPS L1 frequency band, but was modified to operate at the correct frequency.

For the ISM band antenna, a linearly polarized design was chosen to minimize antenna size. Several types of antennas were found that could radiate at the desired frequency ranges. The first was a dielectric resonator antenna[38, 39]. This antenna was very interesting and

14

could allow good performance, but the dielectric material adds too much mass and would be difficult to manufacture. Wire antennas were also considered, but they were quickly discredited as vulnerable to damage during probe operation if made of thin gauge wire, and too heavy at larger gauges.

Based on the above considerations, the planar inverted-F antenna, PIFA, was chosen. This type of antenna has been utilized in many devices and configurations. The PIFA is commonly found in cell phones and designed for cell phone bands [40, 41, 42, 43]. Many modifications of the PIFA have been documented [44, 45] which led to the selection of the PIFA as the basis of design for the ISM band transmitter. The antenna design was started with the design by Stuzman [14], but was modified to fit the requirements of the device.

Chapter 3

Design and Simulation

3.1 Preliminary GPS Antenna Design

As with many initial designs, the preliminary GPS antenna design did not perform as well as desired. Since the GPS signal is RHCP, the goal was to create a RHCP antenna to prevent the 3 dB loss due to polarization mismatch.

The initial design was based on the antenna developed and described by Chen [37] shown in Figure 3.1. This antenna was designed to create a reduced size, rectangular, CP patch antenna with an inset microstrip feed at the 1653 MHz to 2183 MHz frequencies. It was constructed on 1.6 mm thick FR-4 substrate. The key features of the antenna are the polarization, easily matched feed structure, and reduced size based off the typical corner truncated patch antenna. The key dimensions of Chen's antenna are shown in Table 3.1. The slots are a way of increasing pathlinks, due to the meandering current path, in the antenna so that the overall size can be decreased, and the slots create two orthogonal near-degenerate resonant modes for CP radiation [37]. The truncated edges of the antenna help promote the two orthogonal resonant modes and are typical in probe feed CP patch antennas [26].

The antennas designed by Chen, depending on the slit structure, were resonant at frequencies between 1.653 GHz and 2.183 GHz which are too high for the GPS L1 band; therefore, the design was modified to be resonant at the GPS L1 band, 1575 MHz, see Tables 3.1 and 3.2. The antenna was modified by changing the dimensions of the slits, gaps, and corner truncations. This resulted in a 59 percent reduction in size compared to a conventional RHCP patch antenna which was an improvement over the 55 percent maximum reduction predicted by Chen [37]. The designed antenna was then implemented on the 70 mm circular substrate in HFSS as can be seen in Figure 3.2. Figure 3.3 shows the designed antenna

16

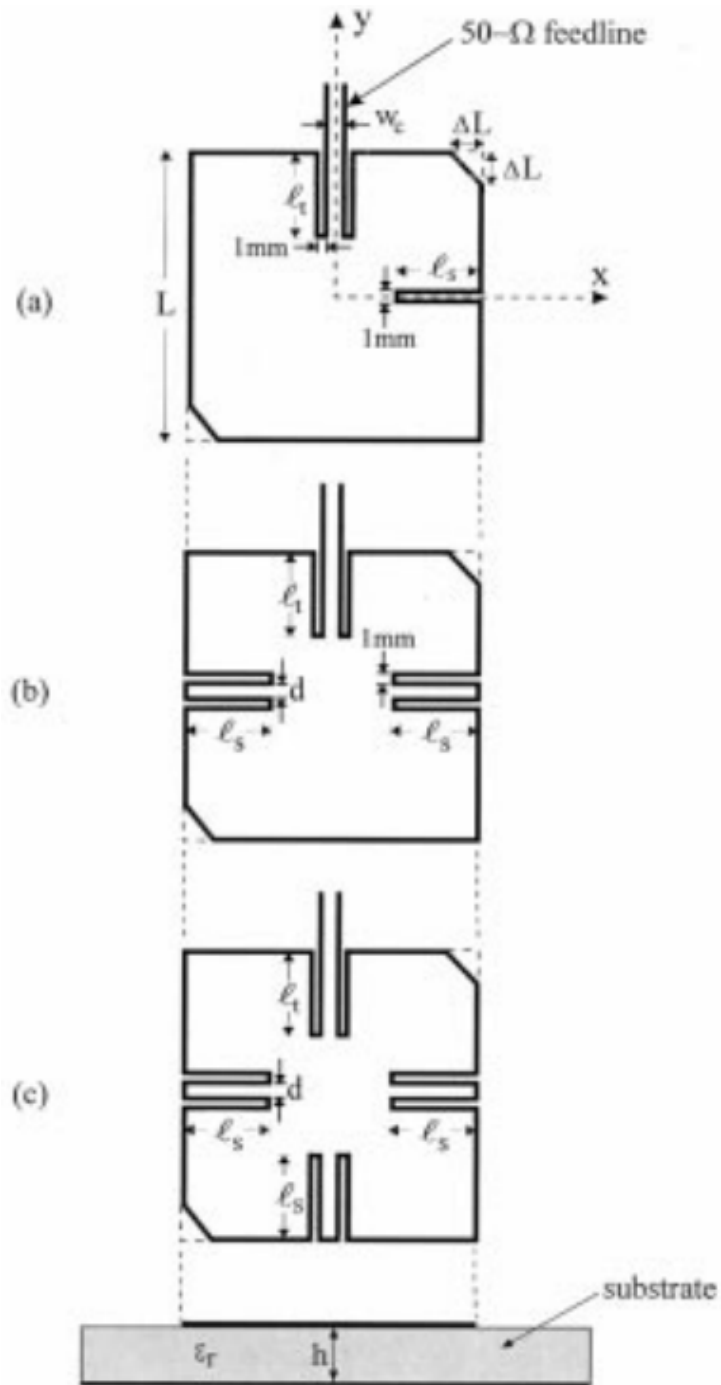with additional key dimensions labeled. Figures 3.4 and 3.5 show the 3D polar antenna plot generated in HFSS.

Figure 3.1: Chen's Antenna Layout

	l_s (mm)	d (mm)	l_t (mm)	ΔL (mm)	F_c (MHz)
Design A	9.7	—	7.4	3.3	2183
Design B	9.8	3.0	10.8	3.6	1775
Design C	10.8	3.0	10.8	3.9	1653
Reference	—	—	—	3.2	2480
GPS Modification	10.8	4.5	10.8	4.2	1570

Table 3.1: Chen's Designs Compared to the GPS Modification

Label	Dimension (mm)
P_W	32
P_H	32
G_W	45
G_H	45
L_S	10.8
ΔL	4.2
S_D	70
A	6.5
B	1.95
C	10.4

Table 3.2: Antenna Dimensions for the GPS CP Antenna

At a cursory glance, the antenna performed well and appeared to meet expectations. The S_{11} is below -6 dB for 1.54 GHz to 1.63 GHz as seen in Figure 3.6. The VSWR is below three for 1.54 GHz to 1.63 GHz as seen in Figure 3.7. This met the specifications outlined earlier in this thesis to classify as successful operation. Unfortunately, looking at additional parameters led to a less positive result. The antenna pattern was dipole-like for total gain, but it had a poor overall gain. The maximum total gain simulated was approximately -3 dBi as seen in Figure 3.4. The antenna was a less efficient CP radiator as the gain was an order of magnitude lower. The pattern was also less isotropic, which is to be expected for a CP radiating patch. The pattern for the CP directivity can be seen in Figure 3.5.

The antenna proved to be insufficient for the eMote system. A driving factor for the probe was to reduce the mass. This antenna was already relatively large, 32 mm by 32 mm. This antenna also requires a 1.6 mm (62 mil) thick substrate for optimal operation. This
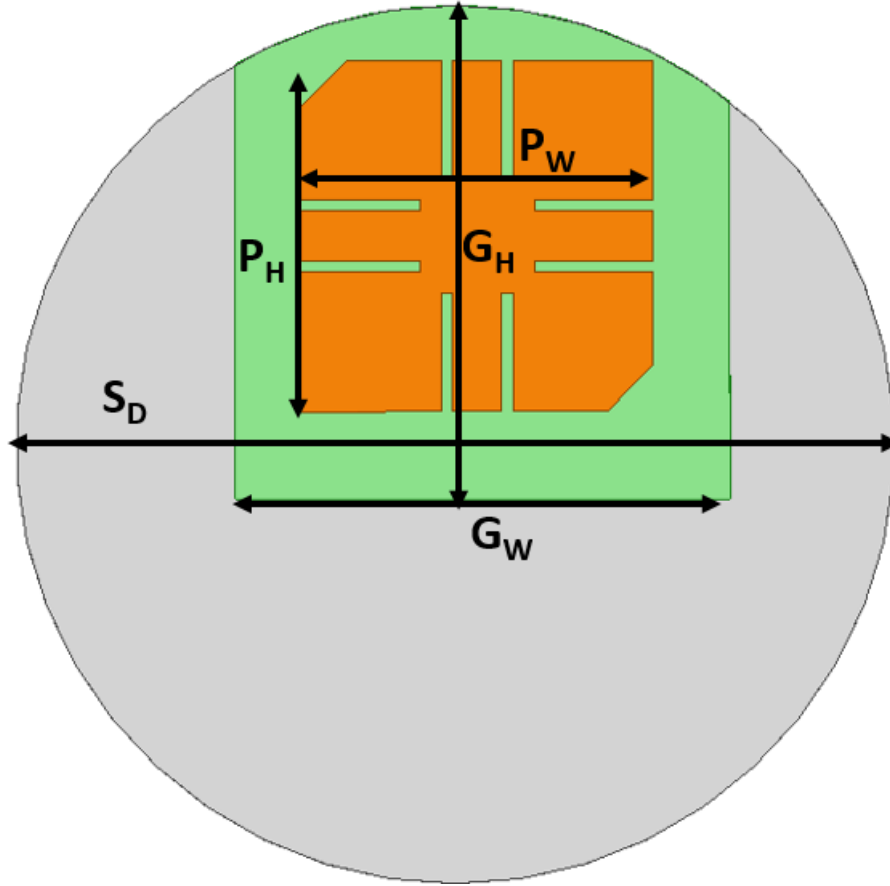
Figure 3.2: Initial GPS Antenna Design in HFSS with Primary Dimensions Labeled

design would require a 70 mm diameter cap. Assuming the density of the FR4 substrate to be 1.850 $\frac{grams}{cm^3}$, the antenna board would weigh 11.39 grams as it exceeded the goal of 5 grams. Therefore, future design iterations focused on reducing the size and mass of the antenna and improving its performance in the GPS L1 band.

3.2   ISM Antenna

After the completion of the design of the preliminary GPS antenna, the ISM band antenna was created. This antenna design was based off of a planar inverted-F antenna, PIFA.
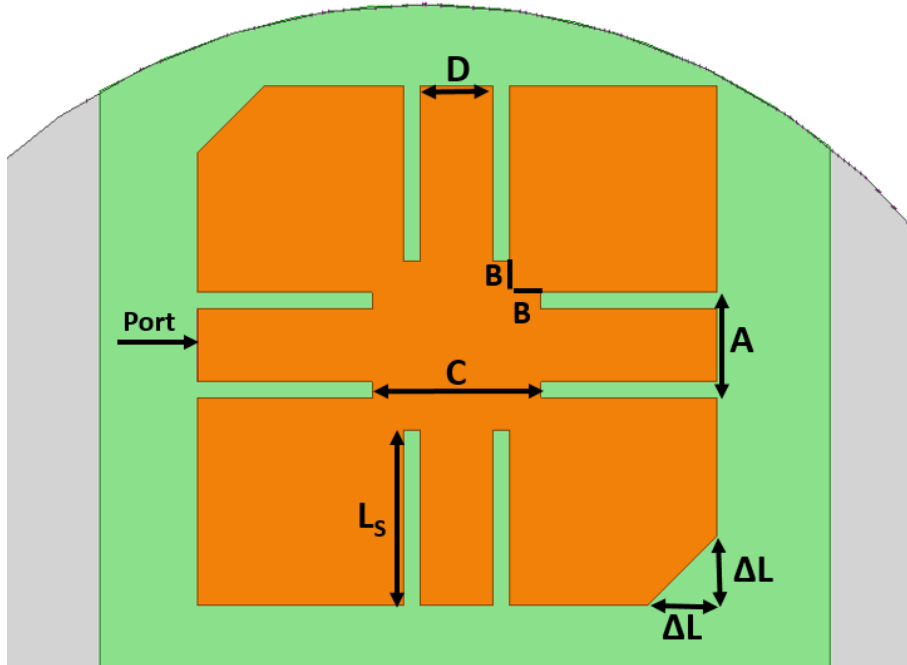
Figure 3.3: Initial GPS Antenna Design in HFSS with Secondary Dimensions Labeled
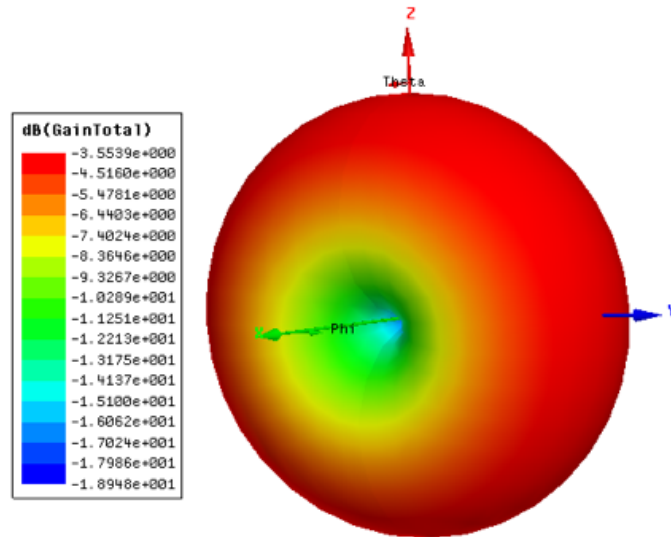

Figure 3.4: Simulated GPS L1 Band Antenna Pattern for Total Gain

3.2.1 Basic PIFA Design Parameters

In order to fully understand the characteristics of the PIFAs that were being designed, preliminary simulations were completed to test how modifications to the antenna changed its behavior. The PIFA is a modification of the inverted-F antenna, which is a modification
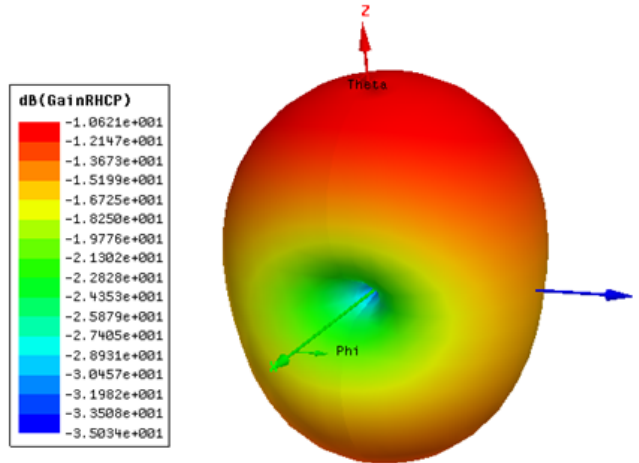
Figure 3.5: Simulated GPS L1 Band Antenna Pattern for the RHCP Gain
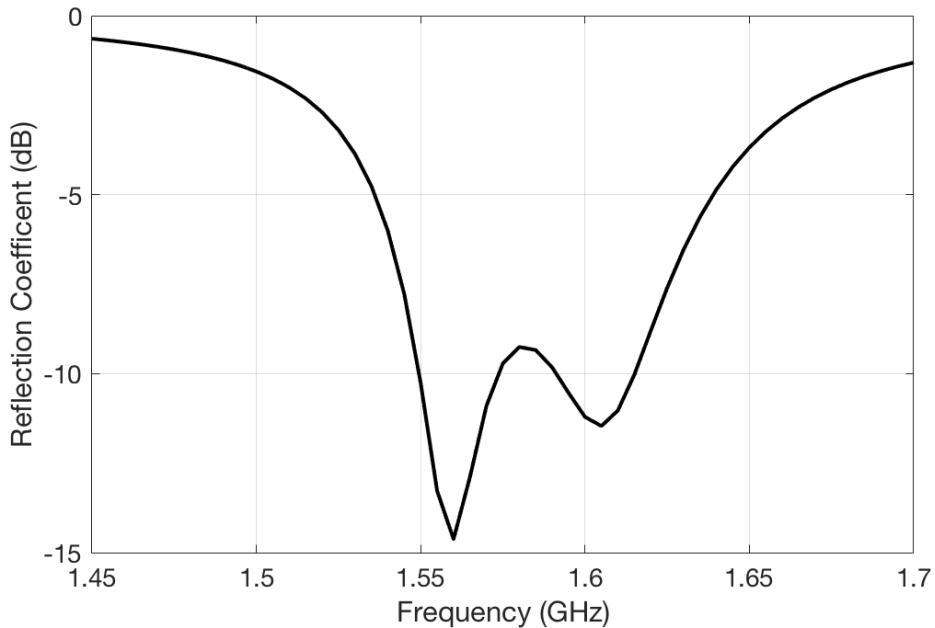
Figure 3.6: Simulated GPS L1 Band Reflection Coefficient

of the inverted-L antenna, which itself is a modification of the quarter-wave monopole [14]. Figure 3.8 shows the basic layout of an inverted-L antenna and an inverted-F antenna in HFSS. The green (lower) plate is the ground plane, the orange is the inverted-L antenna wire, and the blue is the addition of the wire for the inverted-F antenna. The height of the antenna above the ground plane is h, the length of the radiating element is L, and

Figure 3.7: Simulated GPS L1 Band VSWR

the additional length of the addition is s. To create the inverted-L antenna, the wire of a quarter-wave monopole is bent so that it is parallel to the ground plane as seen in Figure 3.8a. The inverted-L antenna has a low radiation resistance and 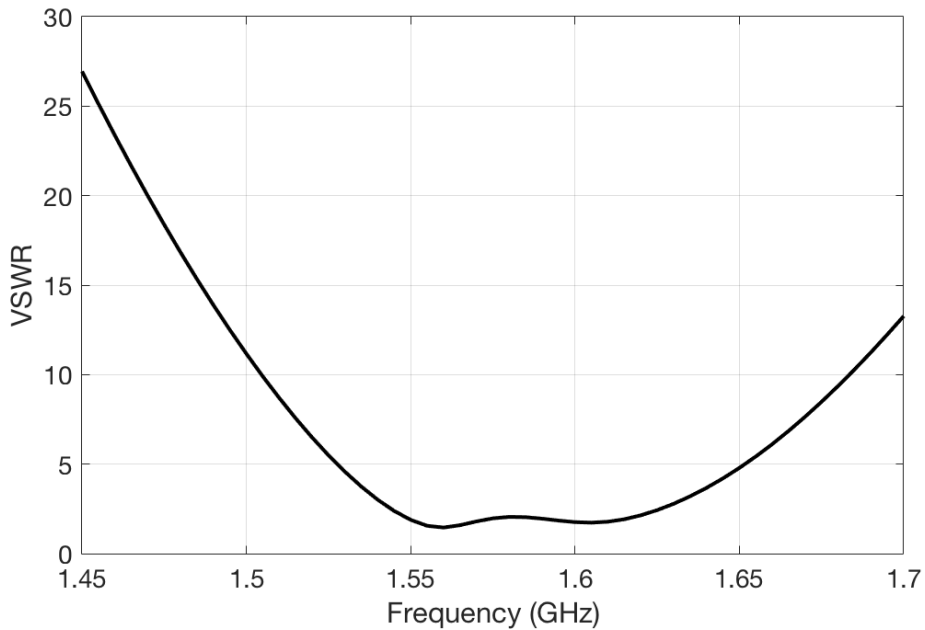a large reactance. When the inverted-L antenna's size is further reduced to create an electrically small antenna the radiation resistance drops further and the antenna becomes very capacitive [14]. To improve the input impedance of the inverted-L antenna, a second wire can be added connecting the end of the antenna to the ground with a distance s, see Figure 3.8b. The addition of this shorting wire creates a conducting loop and the value s can be varied to changed the input impedance while only adding a modest length to the antenna [14]. The distance s can be modified by the designer to better match the antenna to the feeding network.
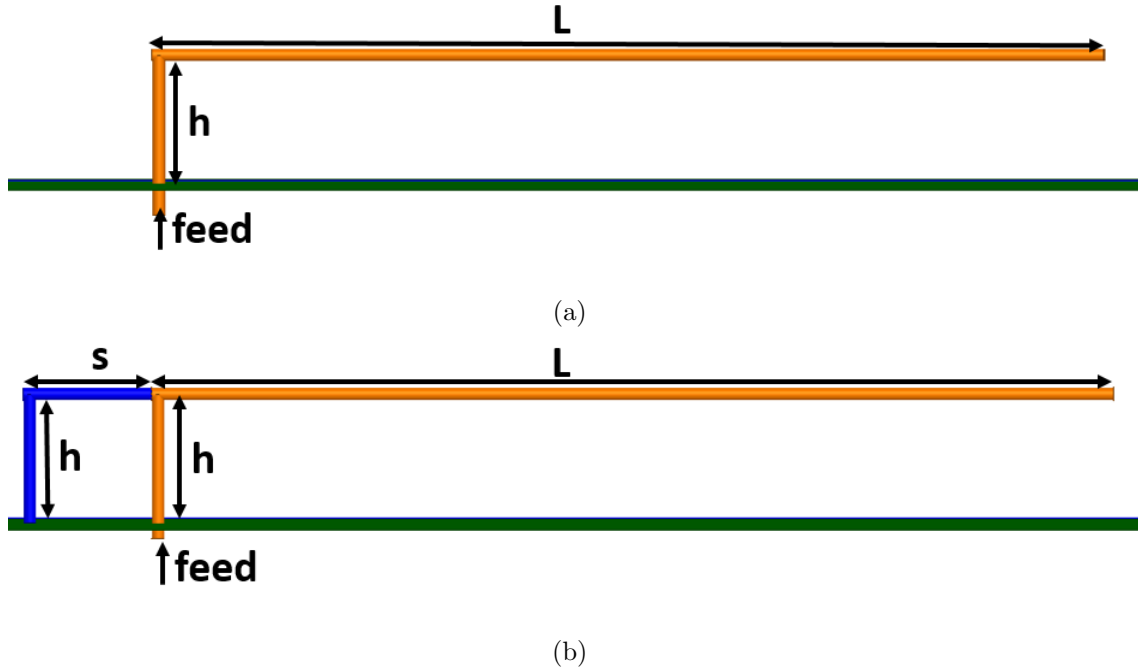
Figure 3.8: Basic Layout and Dimensions of Inverted-L (a) and Inverted-F (b) Antennas

The inverted-F antenna is then modified by exchanging the wire for conductive plates to create a planar inverted-F antenna, PIFA. The design utilizing thin plates of conductive material is generally used when the goal is to use an air gap or foam as a substrate as it is not easy to implement plates in a printed circuit board, PCB. The use of plates gives the antenna designer more parameters to modify than the wire inverted-F antenna. The basic design of a PIFA consists of a ground plane, radiating patch, a via shorting the ground plane and the radiating patch, and a feeding via. A simple PIFA antenna utilizing an air gap can be seen in Figure 3.9. The key dimensions of the PIFA are the length and width of the patch, the shape of the ground plane, the structure of the feed, and the separation between the feed via and the shorting via.
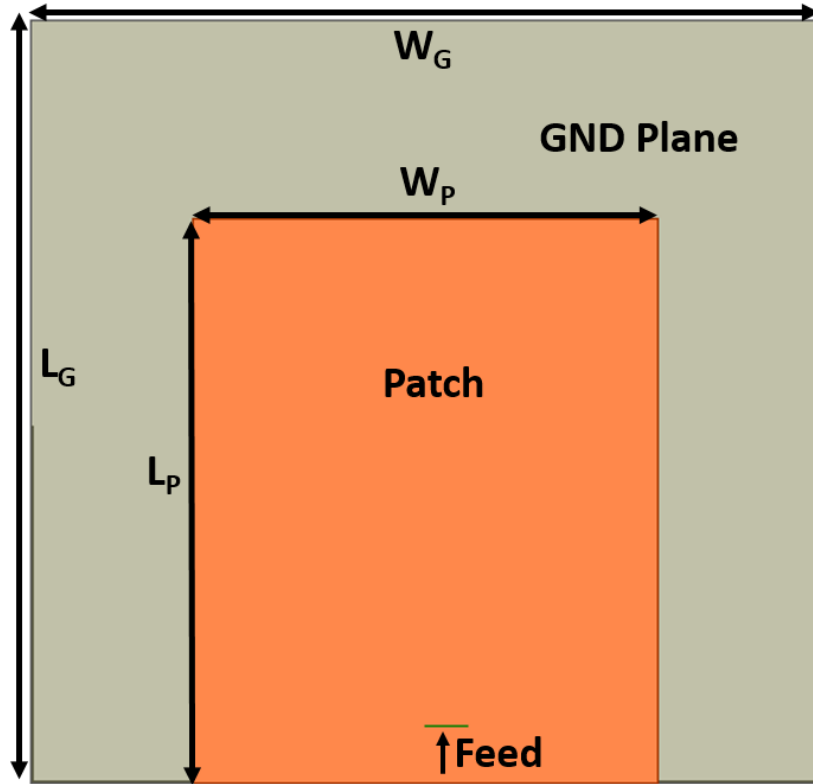
(a)
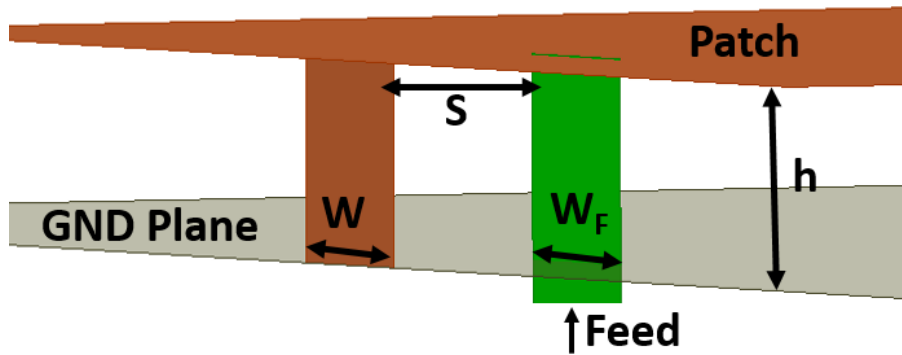
(b)

Figure 3.9: Basic Layout and Dimensions of PIFA in HFSS (a)Top Down (b) Side View

Since this antenna type can be designed to fit within a sphere of radius less than 0.16λ, it is an electrically small antenna. The length and width of the radiating patch minus the feed plate width should add to a quarter of the effective wavelength as seen in Equation 3.1 [46] where c is the free space speed of light.

Equation 3.1 *Resonant Frequency of PIFA [46]*

$$f_r = \frac{c}{4\sqrt{\epsilon_r}(W_P + L_P - W_s + h)}$$

Both the feed and shorting plate widths affect the bandwidth of the antenna. A narrower shorting via increases the bandwidth of the antenna compared to a wider shorting plate. If the width of the shorting plate is increased, the resonant frequency drops as can be seen in Equation 3.1. Therefore, the antenna designer has to adjust both the width of the shorting plate and the antenna size to get the desired bandwidth at the correct operating frequency. The feed plate width has the opposite effect where a wider plate increases the bandwidth and a narrower plate decreases the bandwidth [47].

When implementing a PIFA on a PCB, feed and shorting vias are used instead of plates for manufacturability. The vias are used as they are easy to implement on a PCB with typical manufacturing processes. When a via is used, w practically goes to zero due to the effect of skin depth [47], and the new f_r is simplified.

**Equation 3.2** *Resonant Frequency of PIFA on PCB*

$$f_r = \frac{c}{4\sqrt{\epsilon_r}(W_P + L_P + h)}$$

Other parameters that can be modified include the height, h, the placement of the antenna relative to the ground plane, the size and shape of the top (radiating) plate, and the size and shape of the bottom (ground) plate. Increasing the height of the top plate over the ground plate increases the bandwidth and decreases the radiation frequency [45]. Moving the antenna over the ground plane changes the behavior of the antenna, but to get the maximum bandwidth, the antenna should be placed at the edge of the ground plane as seen in Figure 3.9. The orientation and design of the top plate and bottom plate affects the bandwidth and the radiation pattern. The larger the ground plane, the more directive the the PIFA becomes. When the ground plane is the same size as the PIFA, the antenna

pattern becomes dipole-like. To achieve an antenna with a gain of 3 dB the ground plane needs to be at least 0.5λ [48]. For small ground planes, the ground plane can be given slots or meanders to decrease the resonant frequency [49, 50].

3.2.2 Integration of PIFA onto Circular Substrate

The PIFA was designed to work in the eMote system so it needed to be implemented on a 1.6mm thick, 70mm diameter circular board. The design was simulated in HFSS. The cap of the cap-and-stem design is where the antennas are being implemented in the current eMote design. The layout of the simulated antenna on the circular board can be seen in Figure 3.10. The antenna was fed through a via and the radiating patch (orange); whereas, the port was defined on the via and uses the ground (green) as a reference.
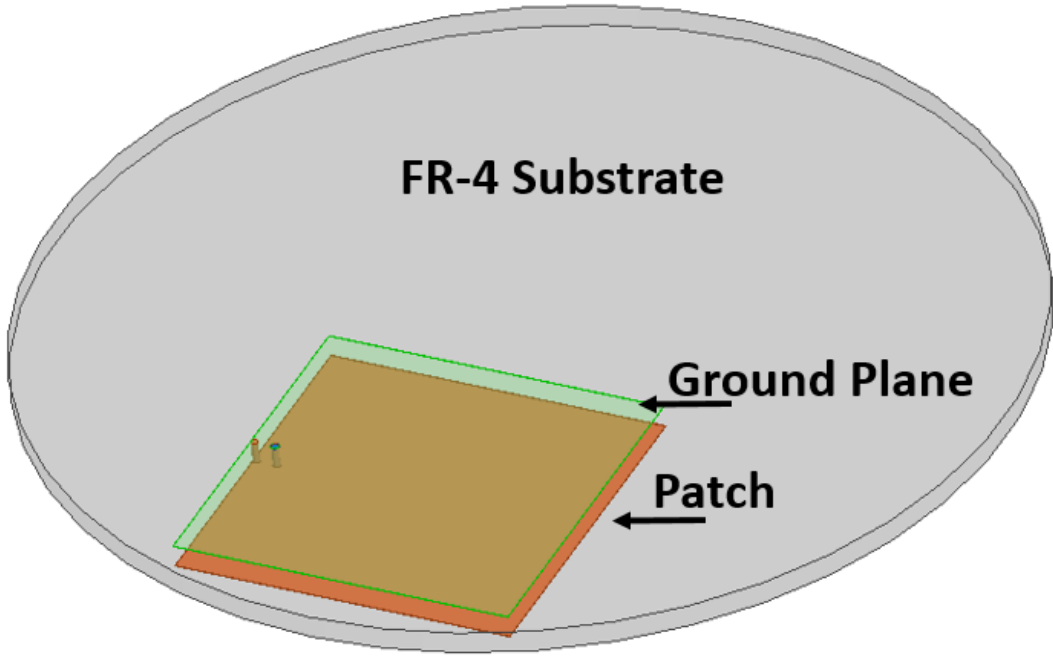
(a)
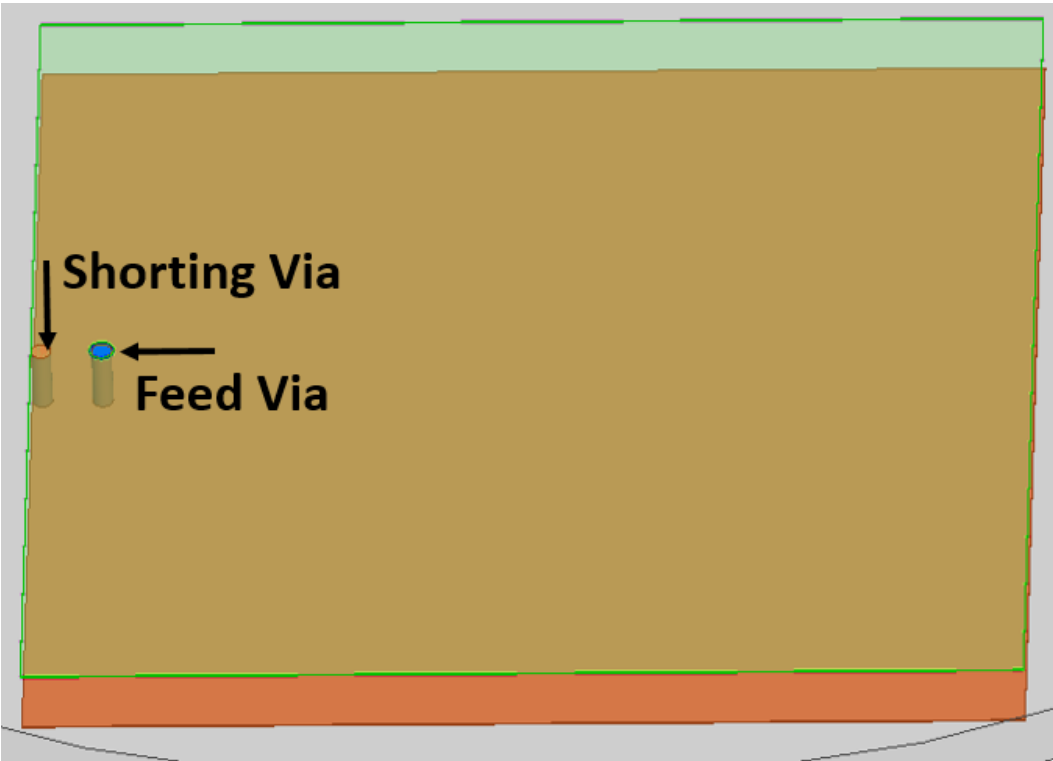
(b)

Figure 3.10: PIFA on Thick Substrate in HFSS (a)Top Down (b) Feed view

Figure 3.11 shows the reflection coefficient and Figure 3.12 shows the VSWR for the simulated ISM band antenna. From the plot of the reflection coefficient, it can be seen that the antenna does not quite make the required ISM bandwidth of 902 – 928 MHz. The VSWR plot also demonstrates this as it is below 3 only between 903 and 928 MHz.

The antenna was not very efficient as seen by the directivity plot in Figure 3.13. This was determined to be caused by the orientation of the antenna on the substrate. As can be seen in Figure 3.10, the antenna was placed where the feed via was towards the side of the cap. When this antenna design was implemented on the circular substrate, the shorting and feed vias were placed on the side of the antenna closest to the edge of the substrate. Implementing this in future design iterations corrected the issue with the directivity.
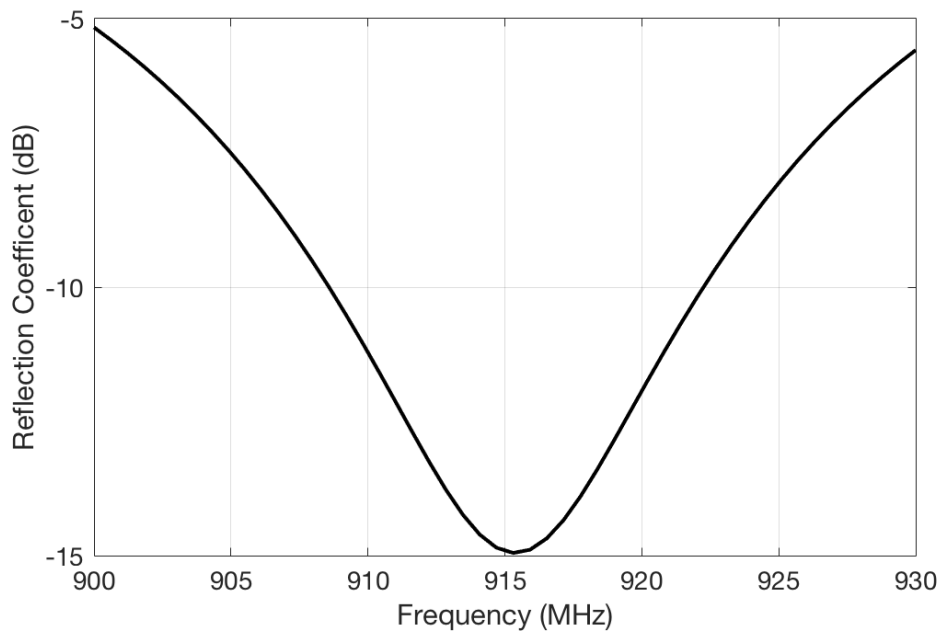
Figure 3.11: Simulated ISM Band PIFA S11

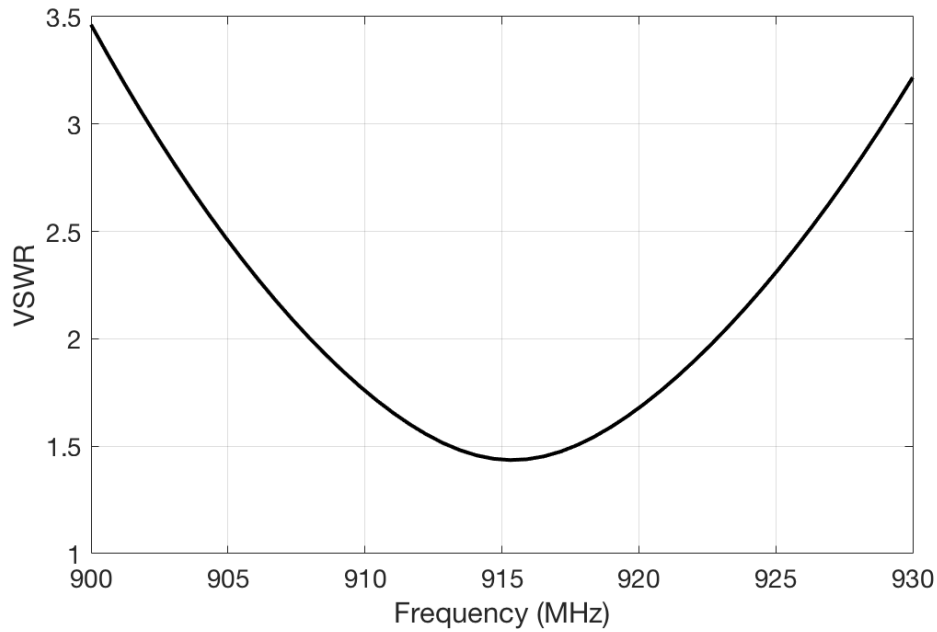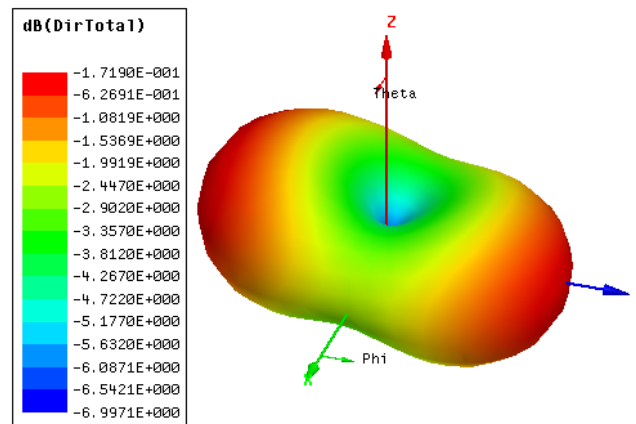Figure 3.12: Simulated ISM Band PIFA VSWR

Figure 3.13: Simulated Directivity of the Antenna in dB

3.3   Integration of Preliminary Antennas

The two antennas were placed together on a 70 mm diameter, 1.6 mm thick circular FR-4 substrate and simulated in HFSS as seen in Figure 3.14. Per the HFSS standard, the FR-4 substrate was assumed to have a dielectric constant of 4.4. The board was then simulated

and parameters extracted from the simulation. Figure 3.15 shows the reflection coefficient of the GPS L1 band antenna and Figure 3.16 shows the VSWR. From these two parameters, the simulated antenna bandwidth meets the 1.563 – 1.587 GHz bandwidth. Figure 3.17 shows the antenna pattern for the RHCP directivity and Figure 3.18 shows the total gain for the antenna. The plot of the total gain shows that the antenna is not an effective radiator or receiver of linearly polarized signals.

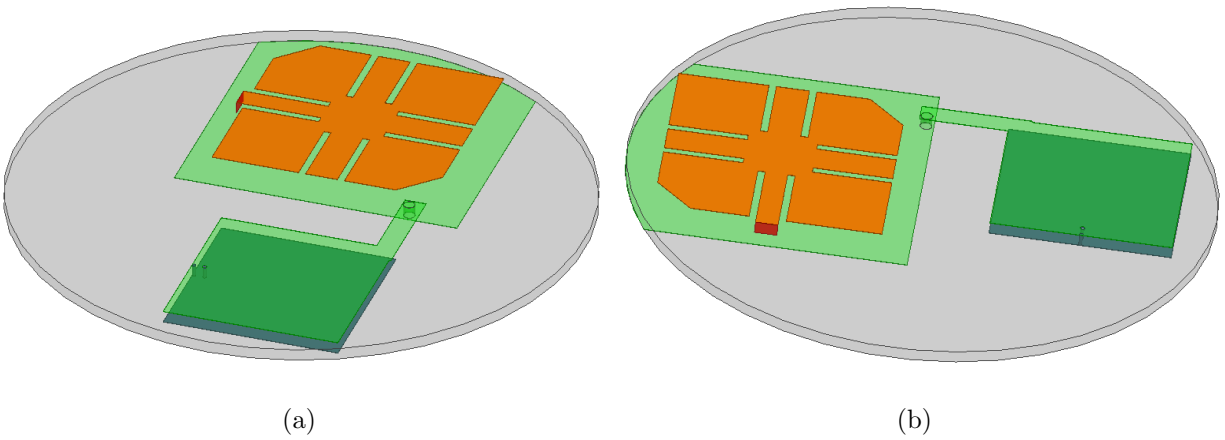(a)   (b)
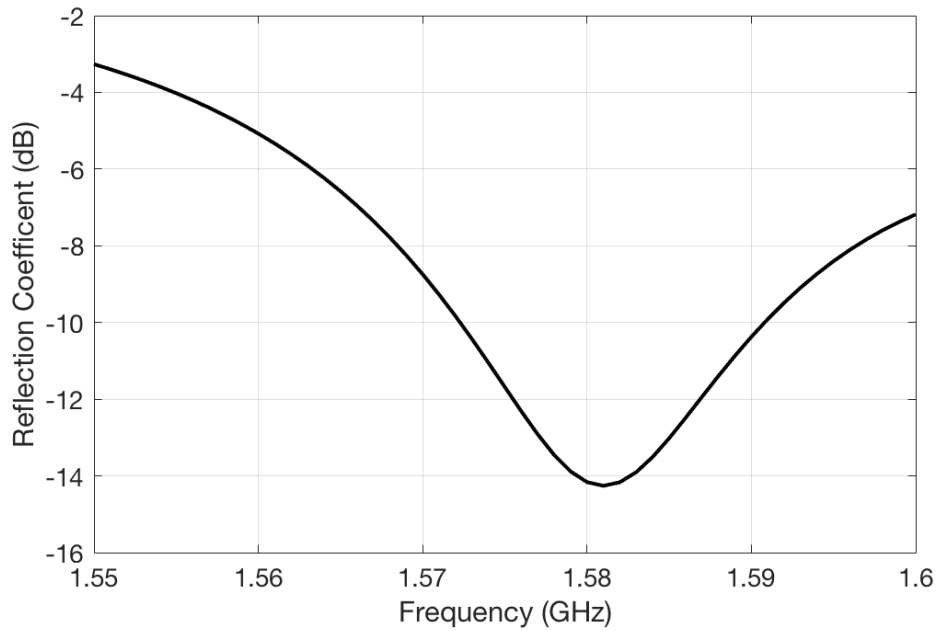
Figure 3.14: Preliminary Antenna Board

Figure 3.15: Simulated Preliminary Board GPS L1 S11
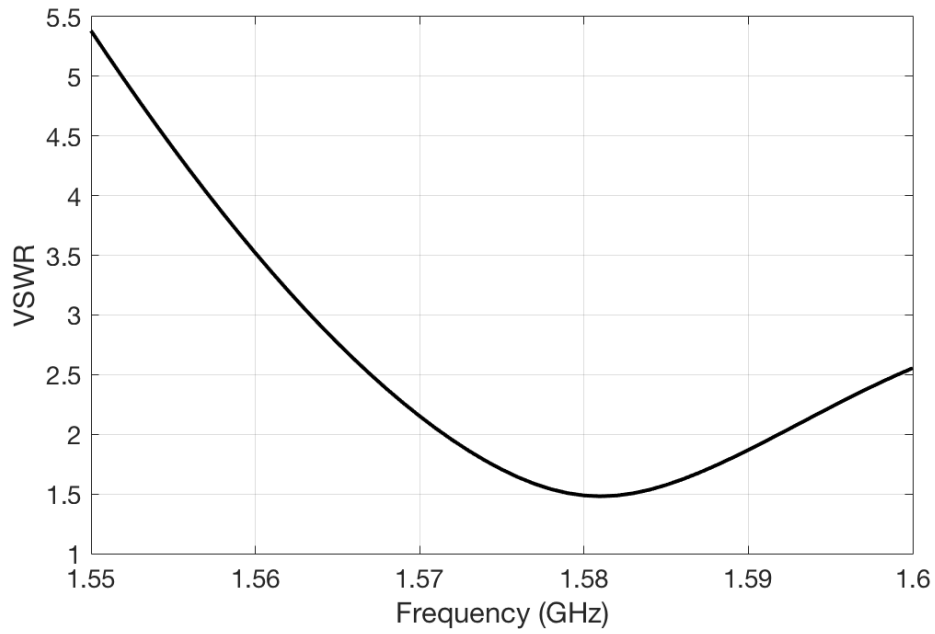
Figure 3.16: Simulated Preliminary Board GPS L1 VSWR
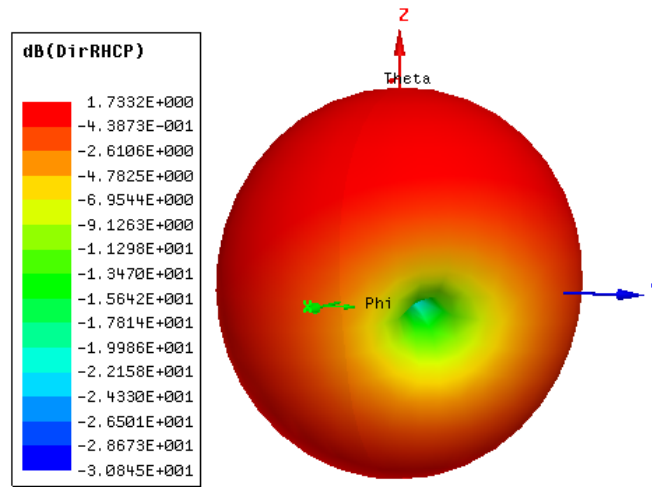
Figure 3.17: Simulated Preliminary Board GPS L1 RHCP Antenna Pattern (Directivity)

dB(GainTotal)

-8.7679E+000
-9.5890E+000
-1.0410E+001
-1.1231E+001
-1.2052E+001
-1.2873E+001
-1.3694E+001
-1.4516E+001
-1.5337E+001
-1.6158E+001
-1.6979E+001
-1.7800E+001
-1.8621E+001
-1.9442E+001
-2.0263E+001
-2.1084E+001
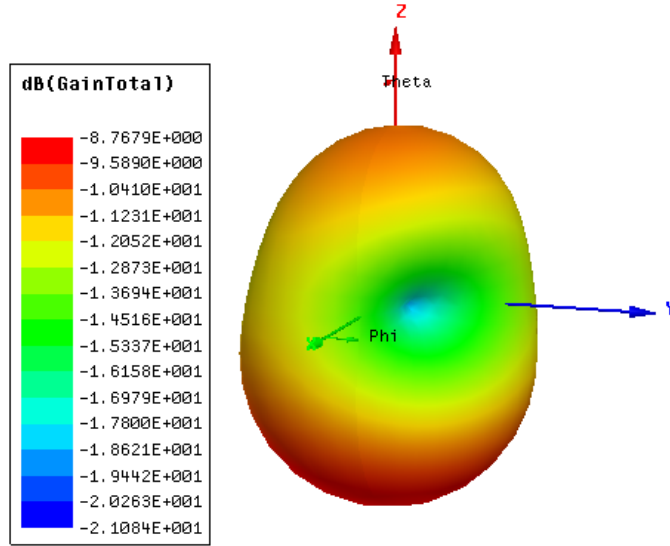
Figure 3.18: Simulated Preliminary Board GPS L1 Total Gain Antenna Pattern

The ISM band antenna implemented was the PIFA designed previously. From the plots of the reflection coefficient and the VSWR, Figure 3.19 and Figure 3.20 respectively, the bandwidth of the antenna is deemed sufficient over the desired operating range of 902 – 928 MHz. Figure 3.21 shows the total gain. The antenna pattern shows that the antenna is not an efficient radiator as the max total gain is approximately -8.75 dB. This was an issue that was addressed in subsequent revisions.
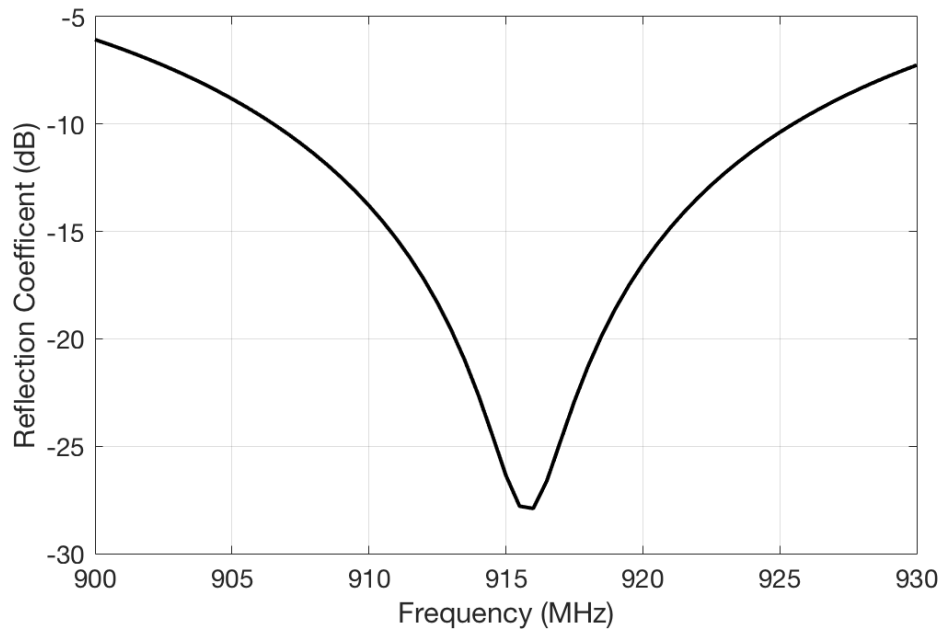
Figure 3.19: Simulated Preliminary Board ISM S11
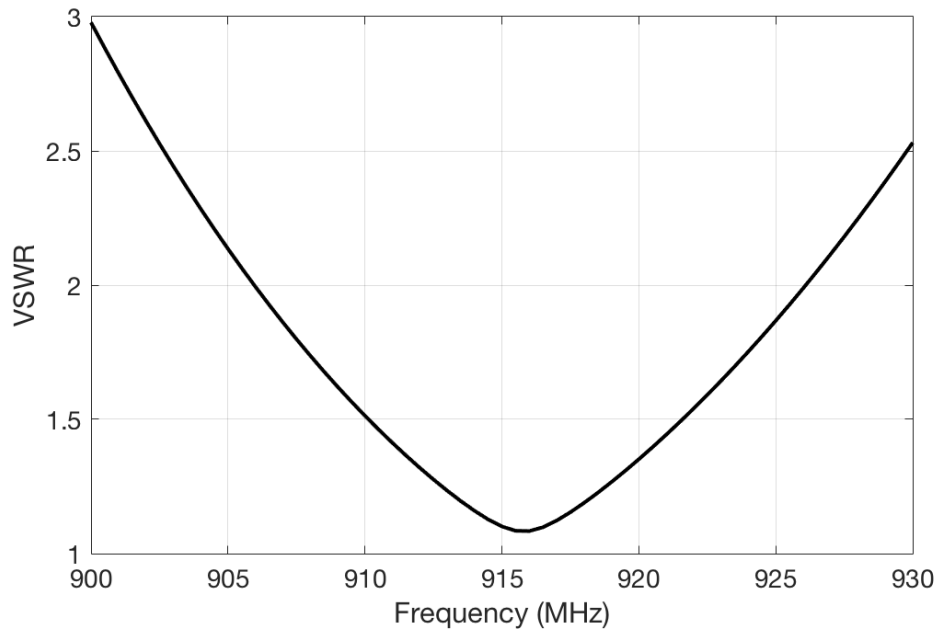
Figure 3.20: Simulated Preliminary Board ISM SWR
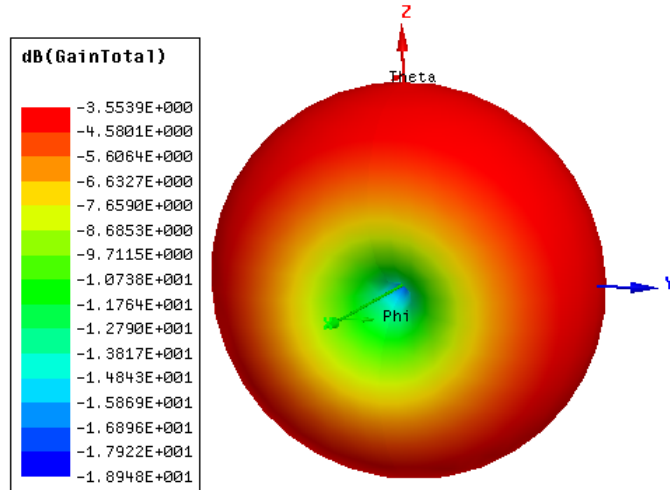
Figure 3.21: Simulated Preliminary Board ISM Antenna Pattern

3.4   Board Revision

The first design iteration of the board was too massive for the eMote application and the performance was sub par. With a typical FR-4 density of 1.85 $\frac{g}{cm^3}$, the weight of the PCB would have been approximately 11.4 grams which was more than twice the target weight of 5 grams. This led to the decision to design an alternate GPS antenna as the preliminary antenna required a 1.6 mm thick substrate to operate effectively. The antenna board was redesigned to utilize a PIFA antenna for the GPS L1 band. Since a PIFA is a linear antenna and not a RHCP antenna, there will be a 3 dB loss due to the polarization mismatch. The new antenna board layout can be seen in Figure 3.22. Refer to the Appendix, Section A.2, for the antenna dimensions.
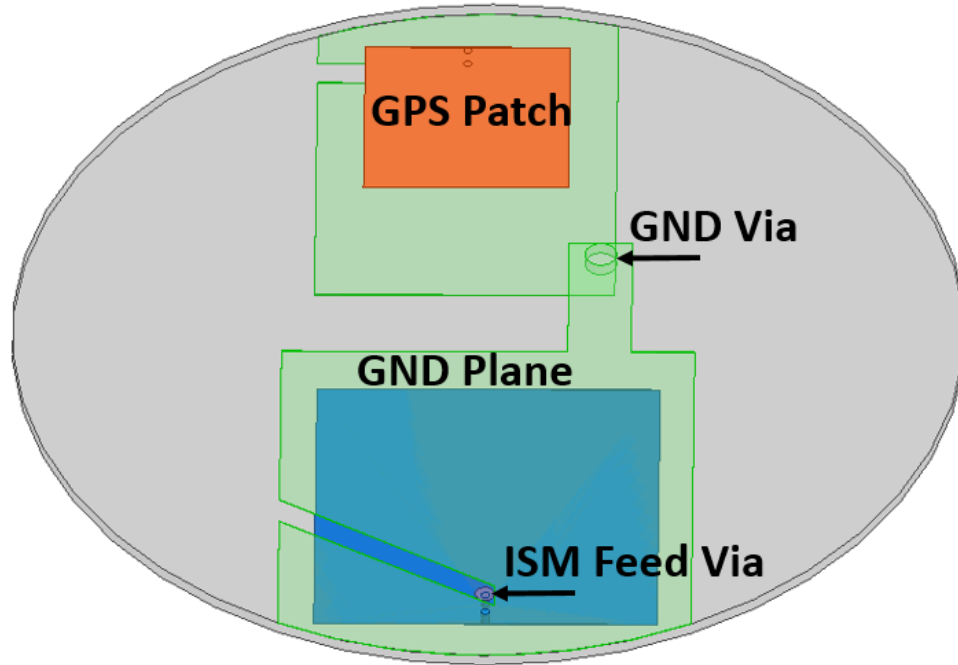
(a)
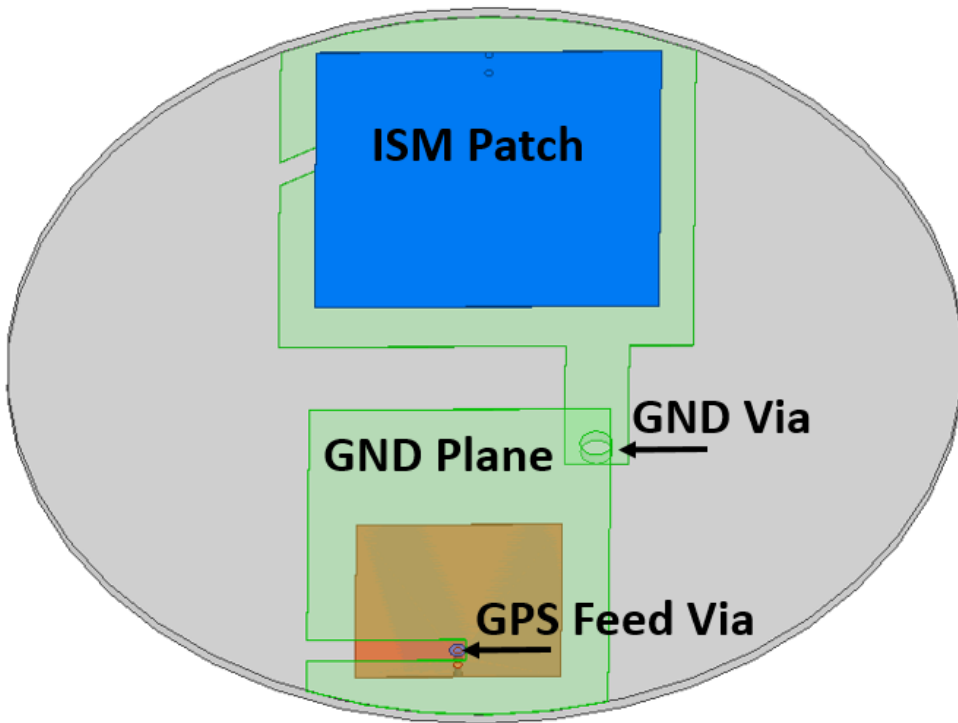
(b)

Figure 3.22: Antenna Board (a) Top View (b) Bottom View

The revised board has a thickness of 0.8 mm and a diameter of 60 mm. This reduction in size reduced the weight to approximately 4.2 grams. This weight was deemed more practical for the application of the device. The newly designed GPS L1 band antenna has the appropriate bandwidth for GPS L1 band frequencies, 1.563 − 1.587 GHz, as can be seen from the reflection coefficient in Figure 3.23 and the VSWR as seen in Figure 3.24. The antenna pattern of the revised GPS antenna can be seen in Figure 3.25. When the eMote device is used, it should be oriented with the cap facing upward. Therefore, the pattern was designed to have the maximum gain pointed upward and slightly to the side for optimum GPS reception. Since this product will eventually be falling from a plane or unmanned aerial vehicle, the new antenna pattern will be pointed towards the sky and the GPS satellites.

Figure 3.23: Simulated Antenna Board GPS S11
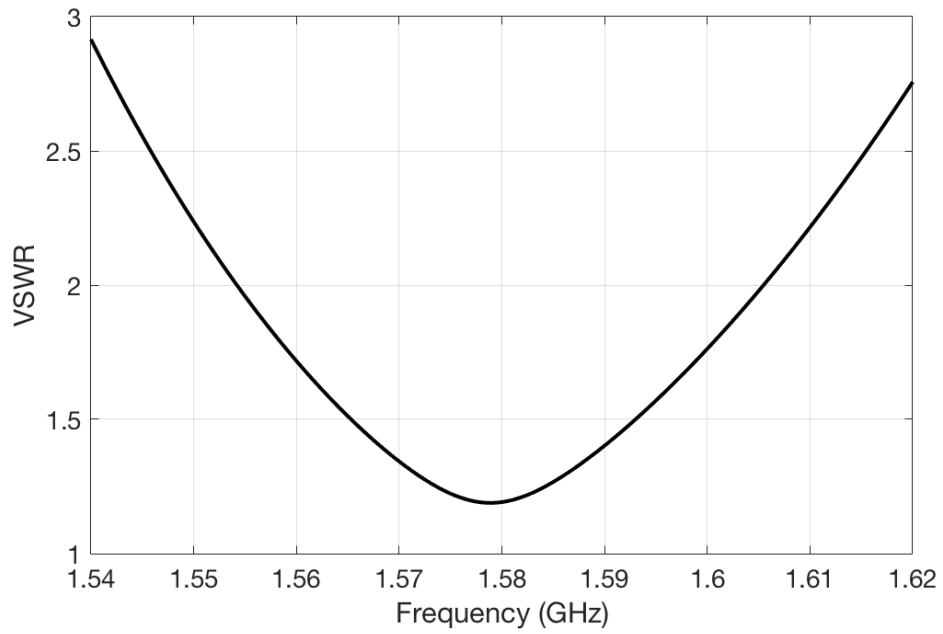
Figure 3.24: Simulated Antenna Board GPS VSWR
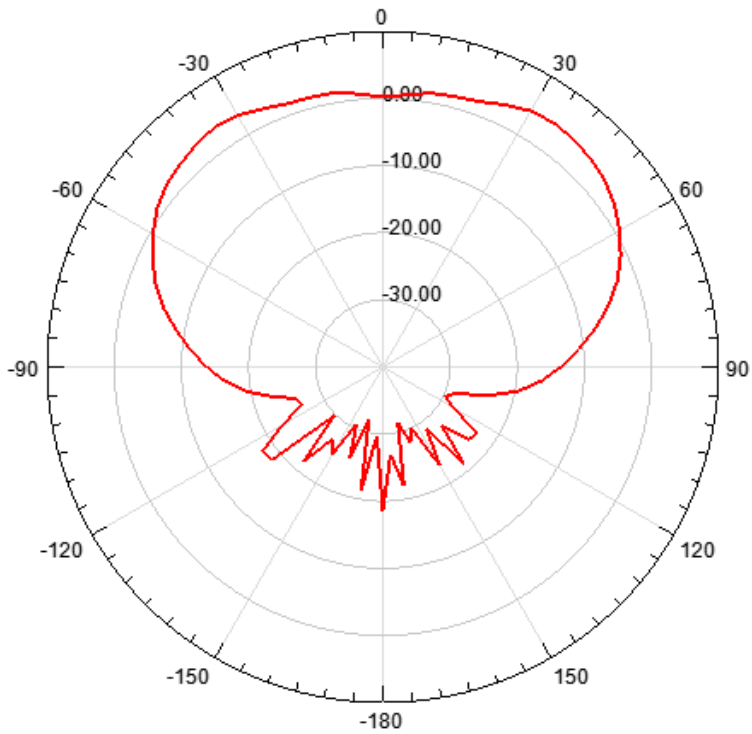
Figure 3.25: Simulated Antenna Board Radiation Pattern GPS L1 Band

The antenna board still utilizes a PIFA for the ISM band transmissions. The PIFA was modified to operate properly on the new thinner substrate. Shrinking the height of the substrate reduced the bandwidth of the device. The addition of the slot in the ground plane for the antenna compensated for the reduction in the substrate thickness [49, 50]. As can be seen from the ISM plot in Figure 3.26 and the VSWR plot in Figure 3.27, the antenna operates in the 902 – 928 MHz band with a steep roll off outside of that band. The radiation pattern is somewhat isotropic and can be seen in Figure 3.28. The steep roll off in the effectiveness of the antenna outside of the designed band minimizes adverse coupling with the nearby GPS antenna. Since the two antennas were designed on a substrate less than one half-wavelength apart [51] the mutual coupling needed to be simulated. The S_{21} or S_{12} parameter for two antennas is also known as the isolation and is a practical way to measure the coupling. The S_{21} plot in Figure 3.29 shows no issue with mutual coupling as S_{21} is always below -25 dB. Therefore, the antennas can be defined as well isolated [52].

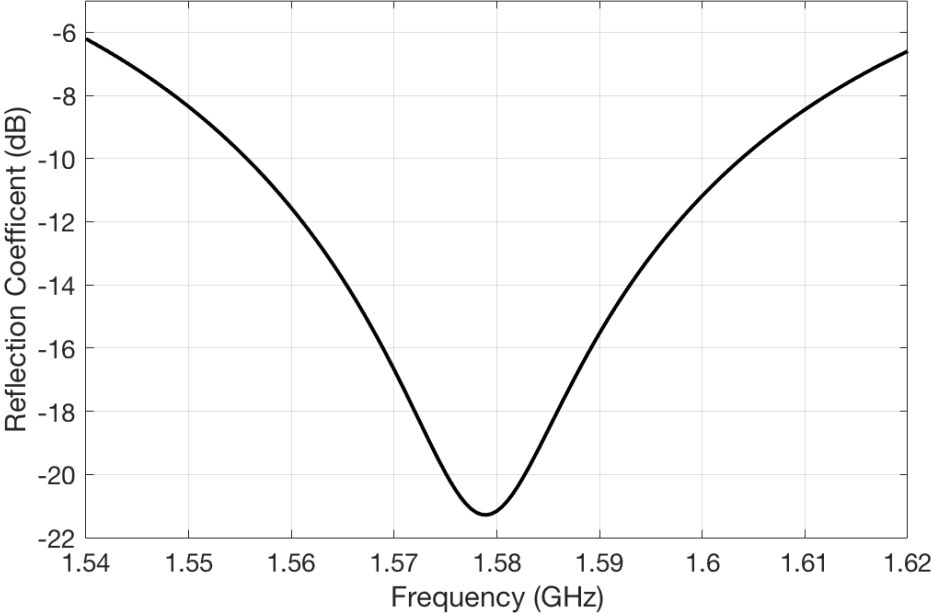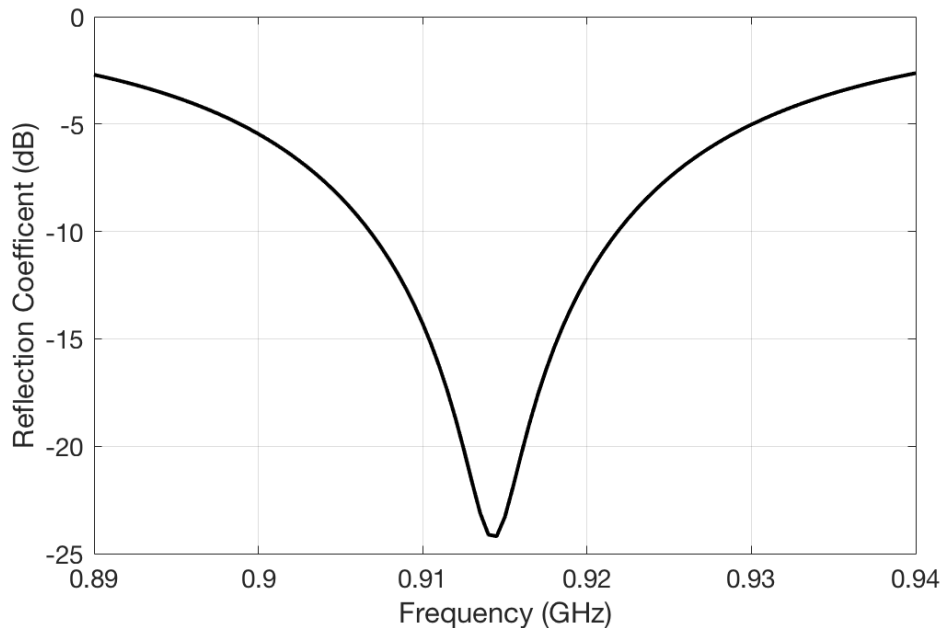Figure 3.26: Simulated Antenna Board ISM S11
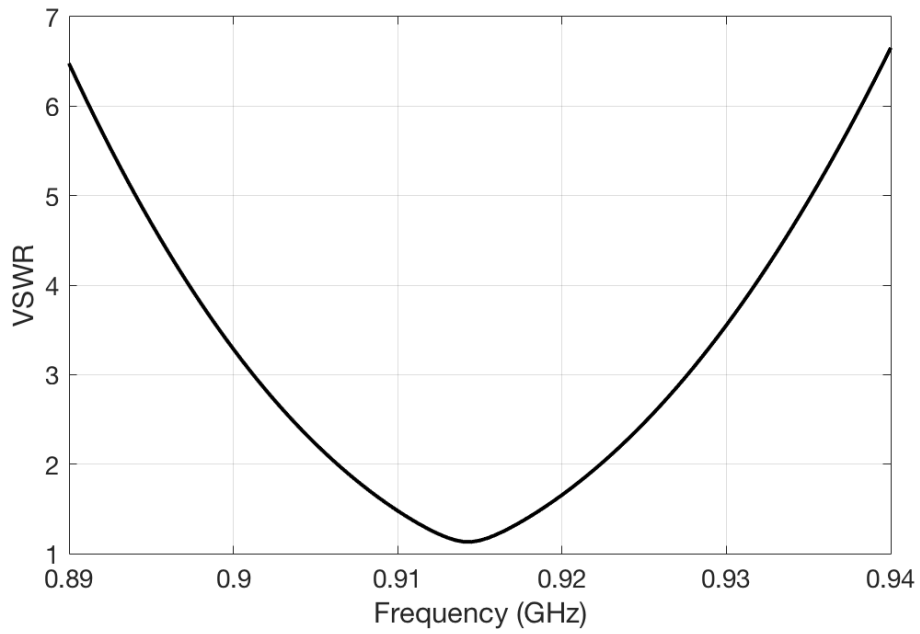
Figure 3.27: Simulated Antenna Board ISM VSWR
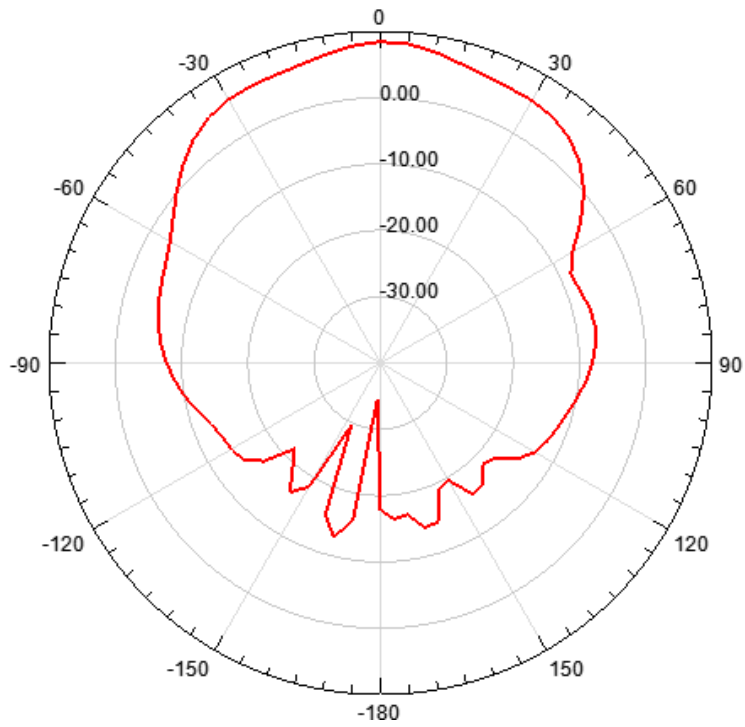
Figure 3.28: Simulated Antenna Board Radiation Pattern ISM Band
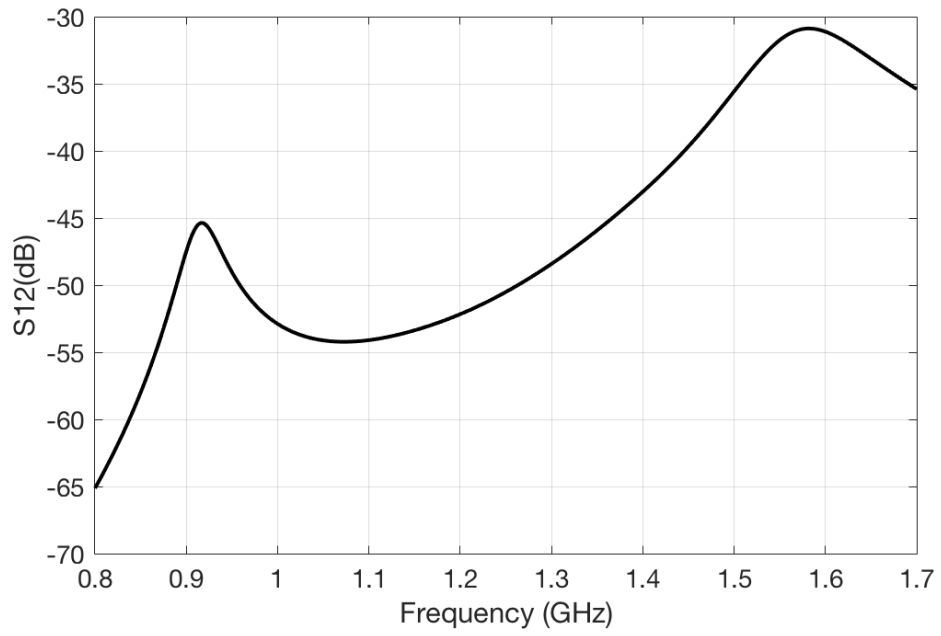
Figure 3.29: Simulated Antenna Board S21

Chapter 4

Fabrication and Testing

4.1 Testing of Fabricated Boards

The final design of the antenna board was replicated in Cadence Allegro PCB Designer. The board was fabricated by Advanced Circuits using gerber board files generated in Cadence Allegro. The board was designed for a FR-4 type substrate with a permittivity of 4.4; however, Advanced Circuits did not have an exact matching substrate so Isola Group's 370HR substrate with a stated permittivity of 4.37 at 1 GHz was selected. Since the permittivity variation was within one percent it should have given acceptable results. Twenty boards were fabricated with the goal of having at least ten working assembled eMotes which allowed for a few boards to be used solely for antenna characterization and testing. Figure 4.1 shows the fabricated antenna board.

(a)   (b)
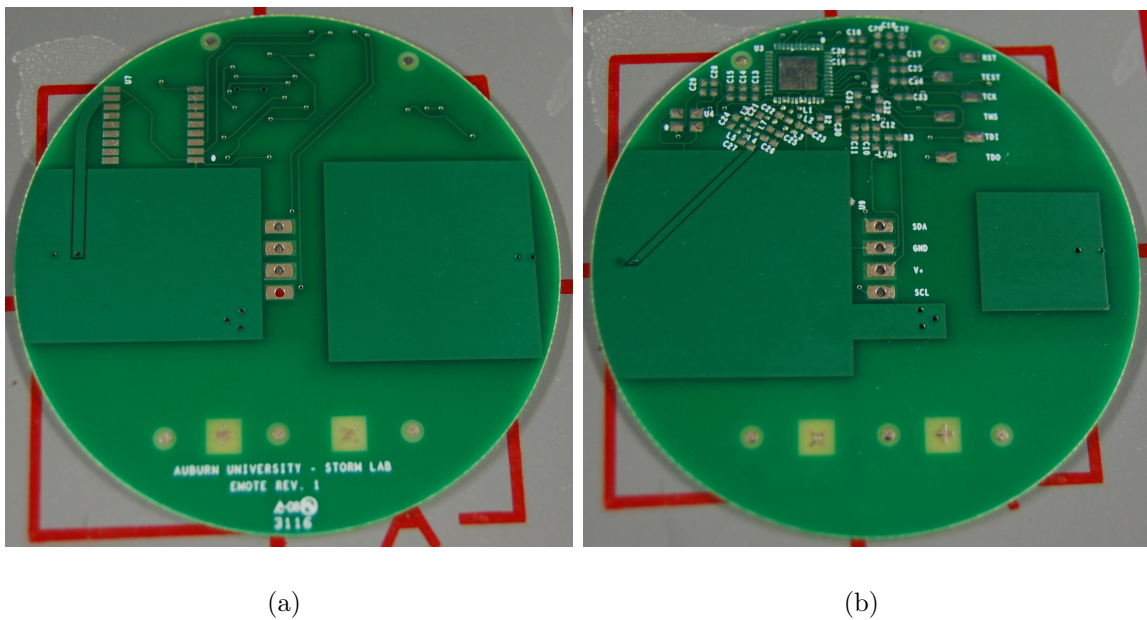
Figure 4.1: Bottom (a) and Top (b) of the Fabricated Antenna Board

When the boards were received, ten boards were populated with components. These boards are now being used by the group to test the probe firmware and the transmission of the sensor data from the eMote probe to the receiver base station.

In order to test and verify the antennas, five boards were modified with an RF connector that could be connected directly to a network analyzer as seen in Figure 4.2. These boards were then tested using a Keysight FieldFox N9918A [8] network analyzer. The testing set-up can be seen in Figure 4.3.

(a)   (b)
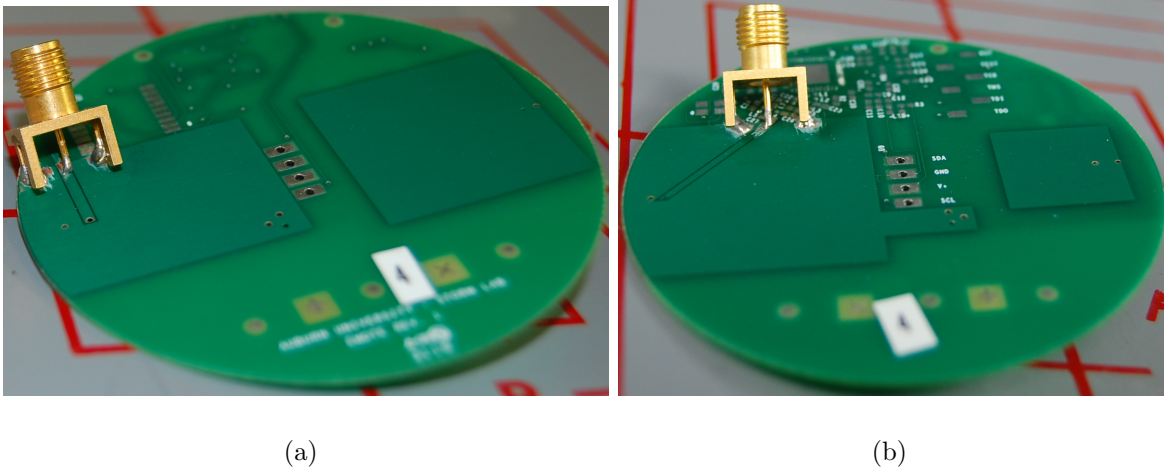
Figure 4.2: Bottom (a) and Top (b) of the Fabricated Antenna Board with Connectors

<div align="center">(a)   (b)</div>

<div align="center">Figure 4.3: Antenna Board Testing Setup</div>

Using the FieldFox network analyzer, the S-parameters and the voltage standing wave ratios were measured on five antenna boards. Five boards were selected as the test size as that was the largest sample size achievable using the available connectors and fabricated boards. If cost was not a limiting factor, several more boards would have been tested to increase the sample size. The reflection coefficient, voltage standing wave ratio, and the S_{21} parameters were measured on all five boards. This data from the antenna boards along with the average of the measured values are shown in Figures 4.4–4.8. Plots of the individual antennas without the average can be seen along with plots of the standard deviation of the antennas in the Appendix, Section A.3.
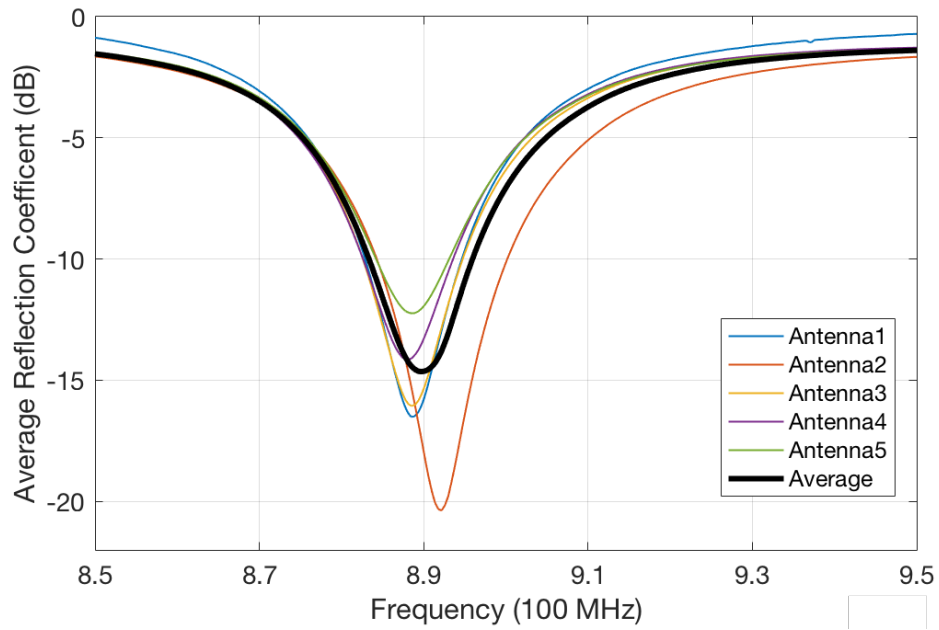
Figure 4.4: Measured ISM Band S11 of the Antenna Boards
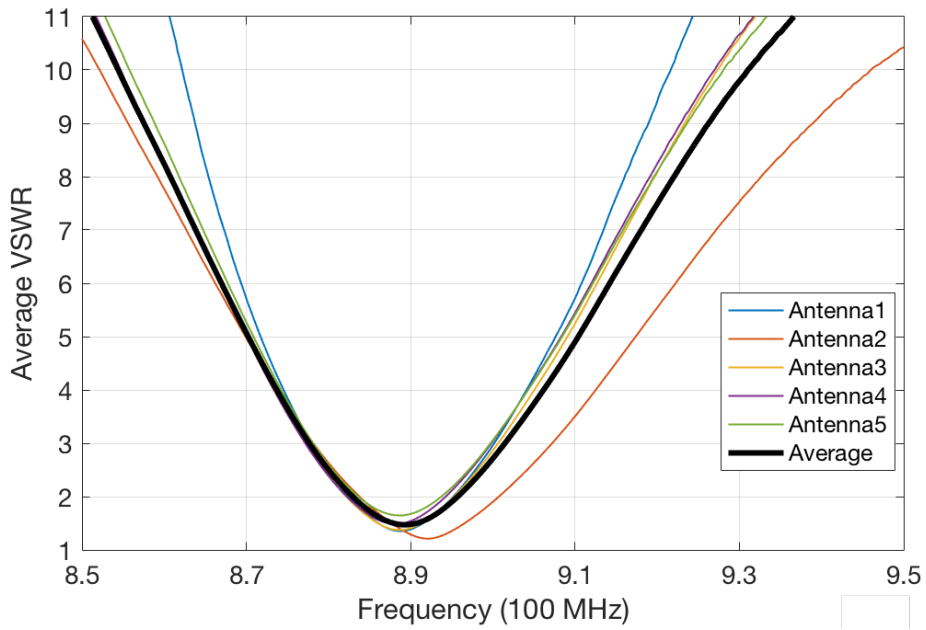
Figure 4.5: Measured ISM Band VSWR of the Antenna Boards
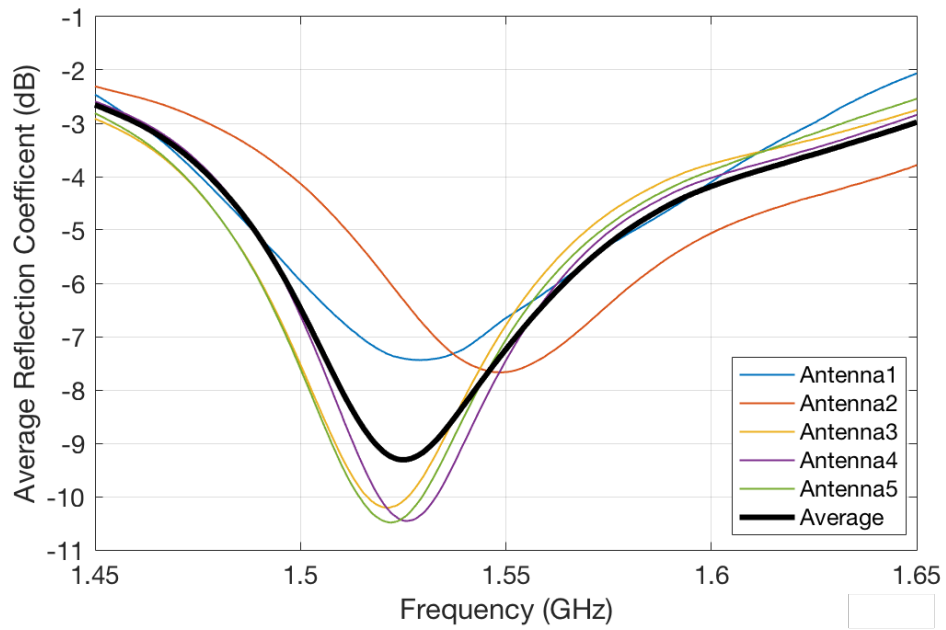
Figure 4.6: Measured GPS L1 Band S11 of the Antenna Boards
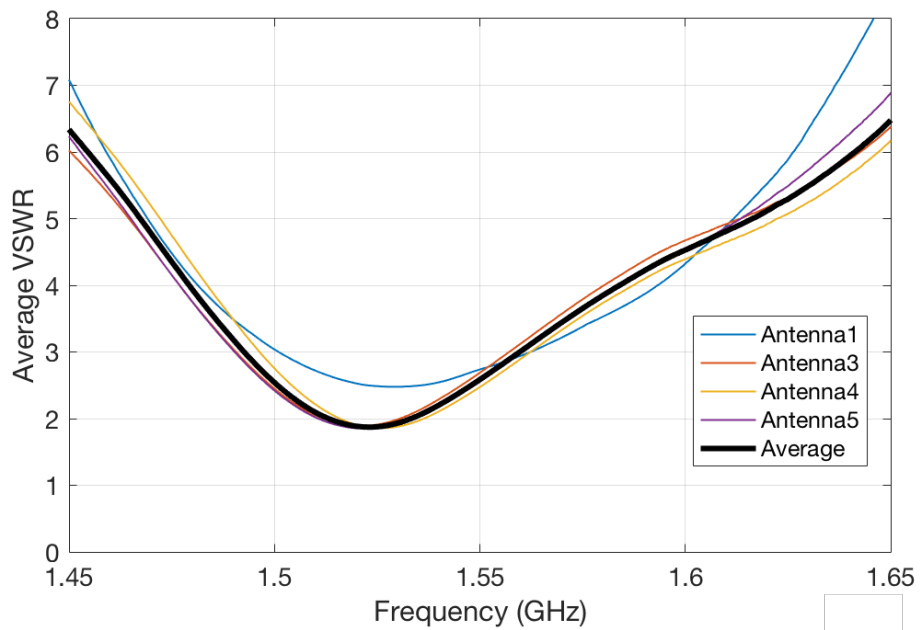
Figure 4.7: Measured GPS L1 Band VSWR of the Antenna Boards
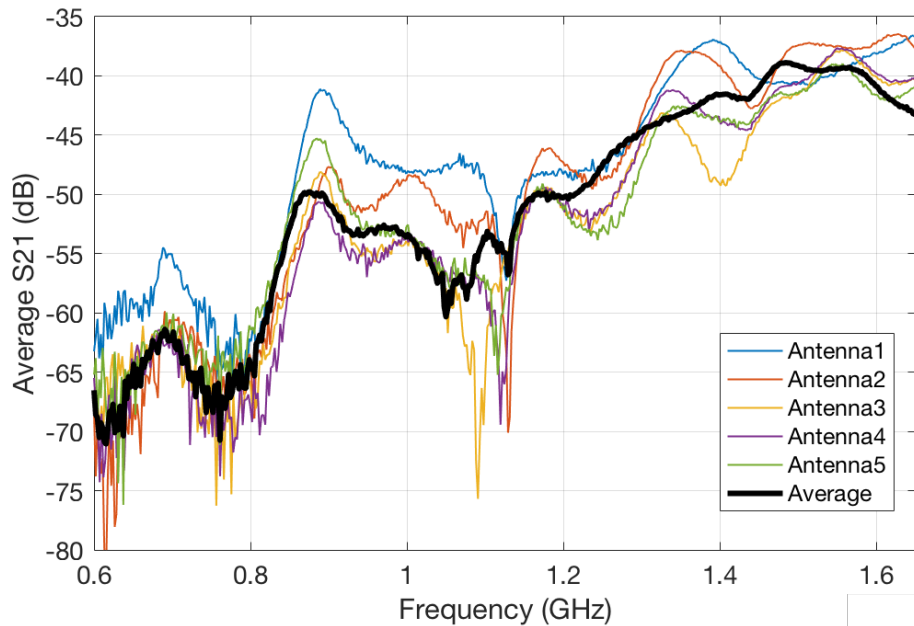
Figure 4.8: Measured S21 Antenna Boards

As seen in Figures 4.4–4.8, the antennas do not operate as simulated. This was a disappointing discovery after the many hours of simulation that went into the board design and creation. Additional effort was required to elucidate the primary sources of difference between the modeled and measured results.

After consulting with subject matter experts in the department, the error was deemed to most likely be with the substrate. One of the redeeming and simultaneously unfortunate qualities of FR-4 substrate is that it is inexpensive. This material is an epoxy resin reinforced with a glass fabric [53]. While an ideal substrate type for most applications, this material can be lossy and less reliable at higher frequencies than more expensive substrates designed for higher frequency operations. Substrates designed for higher frequency applications have more controlled relative permittivity values from board to board.

4.2 Tee Resonator

In order to extract the permittivity of the substrate, a microstrip tee resonator method was used [54, 55]. The permittivity of the substrate changes the effective permittivity of waves on the microstrip and effects their velocity and wavelength. The velocity of a propagating wave can be approximated.

Equation 4.1 *Velocity of Propagating Wave*

$$u_p = \frac{c}{\sqrt{\epsilon_{eff}}}$$

Where u_p denotes the velocity of a propagating wave, c is the speed of light, and ϵ_{eff} is the effective relative permittivity for the microstrip transmission line.

For the microstrip tee resonator test, a microstrip line is created with a stub designed to be a quarter wavelength long at the design frequency.

Equation 4.2 *Length of Stub*

$$L + \Delta L = \frac{[2(N-1)+1]\lambda_G}{4}$$

$N = 1, 2, 3$, etc and is termed the resonance number. For this calculation, N = 1 corresponds to the fundamental resonance where L is equal to a quarter of the effective guide wavelength and is the length of the stub. ΔL is a correction due to fringing fields and is calculated using the approach of Kirshning et al. [56] using the equations given by Schrader [57].

Equation 4.3 *Effective Guide Wavelength*

$$\lambda_G = \frac{c}{f_r \sqrt{\epsilon_{eff}}}$$

Manipulation of Theorem 4.2 and Theorem 4.3 gives [54]:

Equation 4.4 *Effective Permittivity*

$$\epsilon_{eff} = \left[\frac{(2N-1)c}{4f_r(L + \Delta L)} \right]^2$$

The resonant frequency is then seen as:

Equation 4.5 *Resonant Frequency [22]*

$$f_r \cong \frac{Nc}{2(l + 2\Delta L)\sqrt{\epsilon_{eff}}}$$

Following the approach of Fulford and Wentworth [54] the following iterative procedure was used to calculated ϵ_{eff}, ϵ_r, and ΔL using the MATLAB code seen in the Appendix, Section A.1.

1. Enter known values: N, L, w, and h.

2. Compute f_r using measured S_{12} data.

3. Initially assume $\Delta L = 0$.

4. Compute ϵ_{eff}.

5. Compute ϵ_r using equations found in Schrader [57].

6. Compute ΔL using the Kirschning approach [56].

7. Repeat steps 4 – 6 until the changes in ϵ_{eff}, ϵ_r, and ΔL are insignificant [54].

4.2.1   Fabrication and Results of Microstrip Tee Resonator Test

For the microstrip tee resonator testing, a "calibration" line was designed for 1 GHz, a line with a quarter-wave stub designed for 915 MHz, and a line with a quarter-wave stub designed for 1.575 GHz was created. The line widths were calculated using Keysight's LineCalc which is a part of the Advanced Design System software, ADS, and the PCB pattern was created in ADS [58]. The layout can seen in Figure 4.9.
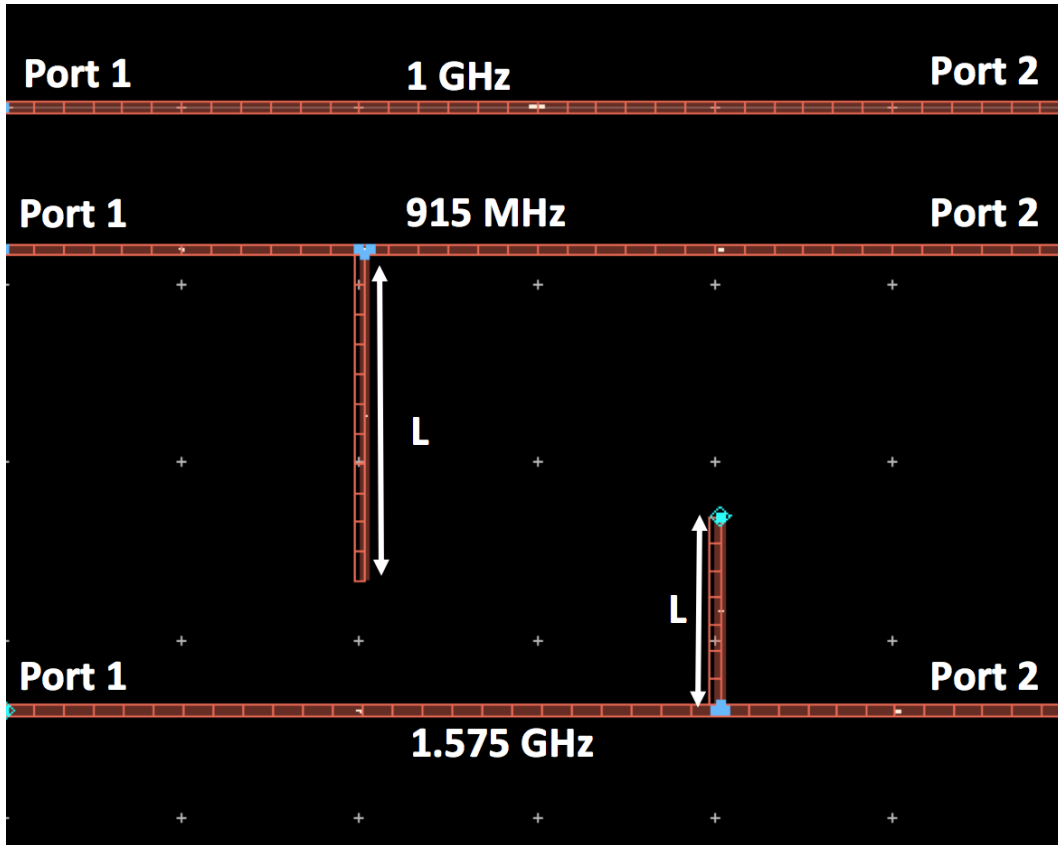
Figure 4.9: Microstrip Tee Resonator Layout in Keysight's ADS

The microstrip lines were then milled using the LPKF circuit board plotter [7]. Two iterations of the test were completed in order to extract the permittivity of the substrate. The tested circuit boards can be seen in Figure 4.10. The first design assumed the relative permittivity of the substrate to be the value quoted by Advanced Circuits, 4.37. The second iteration assumed the permittivities calculated from the first iteration. The results can be seen in Table 4.1.
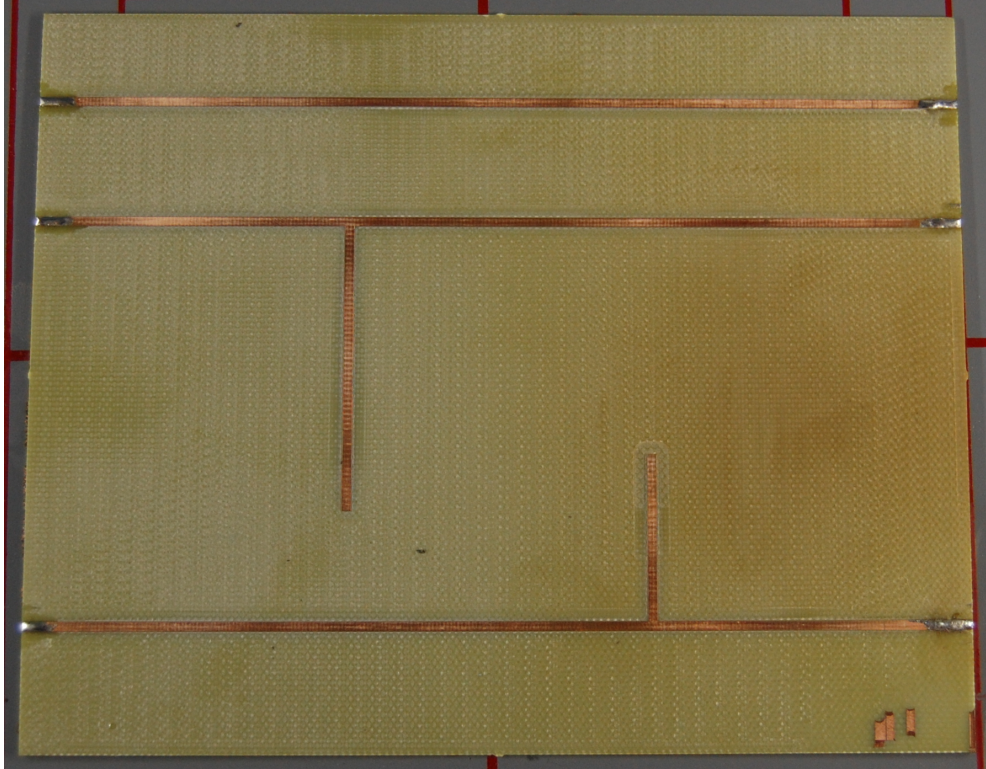
(a)
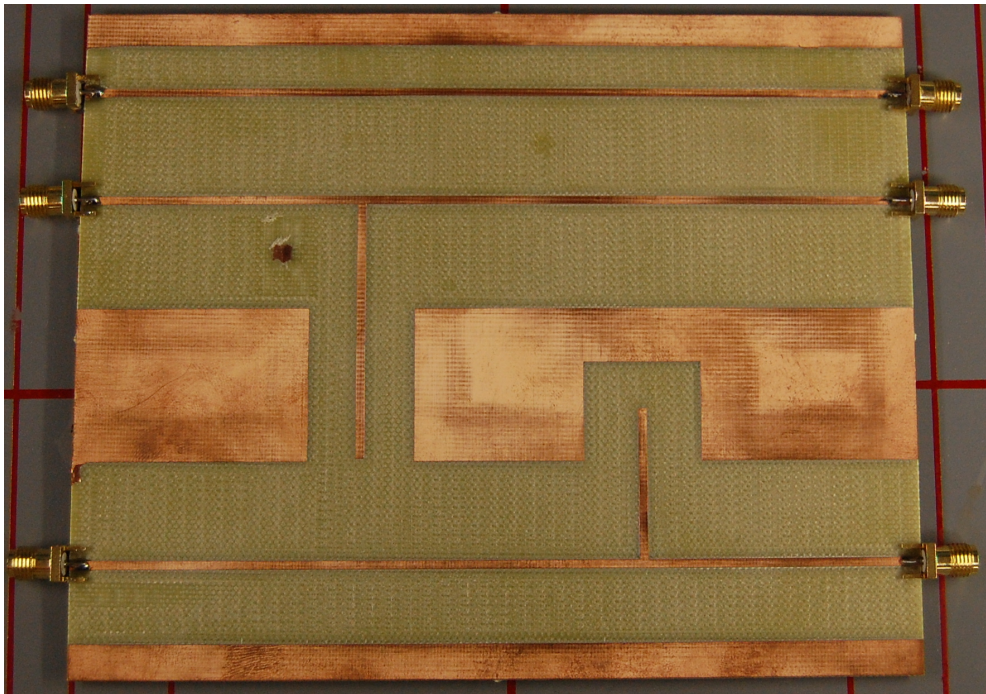
(b)

Figure 4.10: Microstrip Tee Resonator Boards

Iteration	Short Stub (1.575 GHz)	Long Stub (915 MHz)
1	4.14	4.09
2	4.22	4.27

Table 4.1: Calculated Relative Permittivity

As can be seen in Table 4.1, the numbers are less than the cited permittivity values. Unfortunately, time constraints prevented further iterations to verify the exact permittivity of the substrate, but additional revisions should settle on a permittivity value near the results of the second test. The LPKF circuit board plotter does over cut the traces and has a precision on the order of 4 mils. A wet etching process would have increased the precision, but due to unforeseen issues the system was inoperable during the testing phase. The testing does demonstrate that the permittivity is not the permittivity stated by either Advanced Circuits, 4.37, but is closer to the typical value stated by Isola Group, 4.17 at 1 GHz.

The difference in stated versus actual permittivity does cause issues with the antenna design. As seen in Equation 4.5 a decrease in the permittivity of the substrate should lead to an increase in the resonant frequency of the antenna structure, but the opposite was observed. As can be evidenced from the results presented in Section 4.1 this did not account for all of the error of the designed and tested antennas; therefore there were additional issues that needed to be addressed.

4.3   Other Sources of Error

After revisiting the literature on the PIFA, another potential cause of error was found. In PIFA antennas, meandering the ground plane can cause a decrease in the resonant frequency [49, 50, 59]. When the antenna board was fabricated, the DC ground traces were connected to the RF ground plane effectively meandering the ground plane. This unintentional meander of the ground plane decreased the resonant frequency of the antenna. This, combined with the

different permittivity of the substrate would account for the discrepancies in the resonance of the designed and simulated antenna since the PCB traces were not accounted for during the antenna design process.

Another major issue with the antennas were layout inconsistencies. This is due primarily to the difficulty integrating ANSYS Electronics Desktop and Cadence Allegro PCB Designer. As the antennas were designed in ANSYS Electronics Desktop, they had to be separately drawn in Allegro PCB. The antennas were created and measured multiple times, but a few parameters were slightly different after manufacturing. The most critical error was the placement of the GPS L1 Band antenna feed via which was misplaced by 0.4 mm. This accounts for the impedance mismatch seen in Figures 4.6 and 4.7.

4.4   Anechoic Chamber Testing

In order to characterize additional antenna parameters, an anechoic chamber was used to test the feed structure, to test the total radiated power of the probe system, and to test the gain of the antenna. Pictures of the chamber with an L band horn pointed at the antenna board can be seen in Figures 4.11 and 4.12.
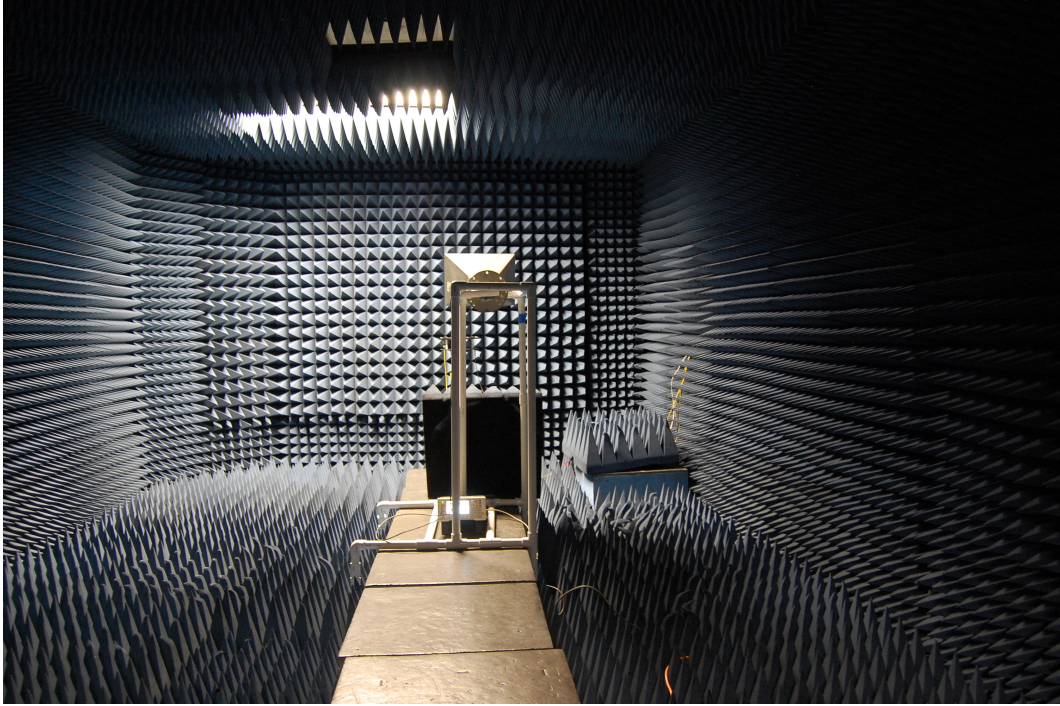
Figure 4.11: Anechoic Chamber
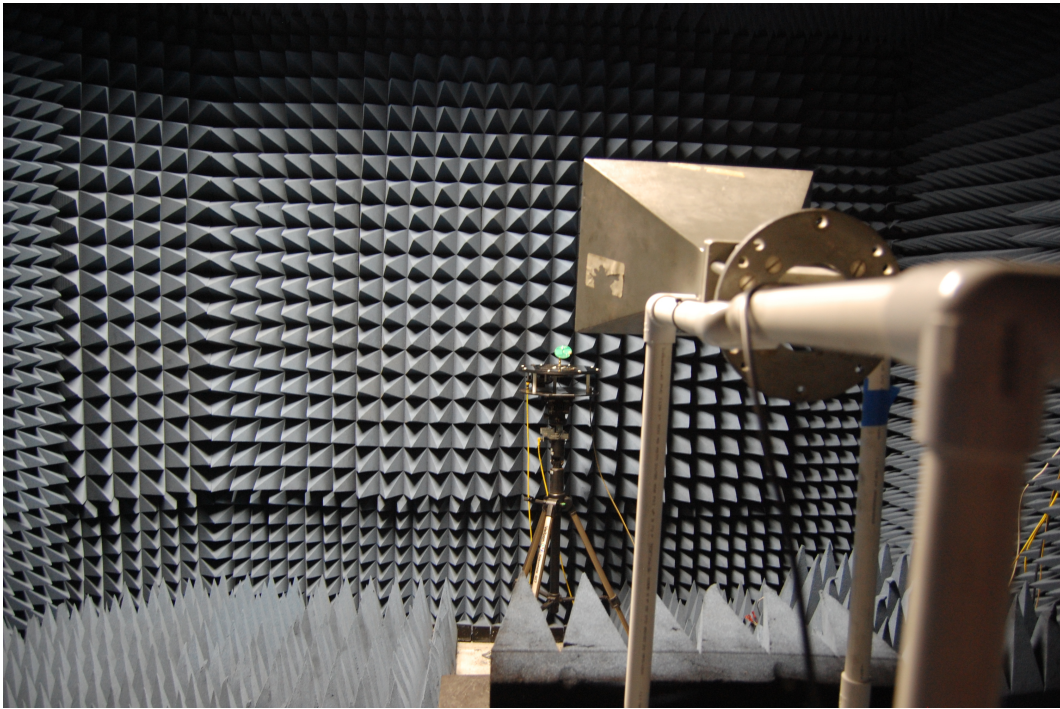
Figure 4.12: L Band Horn Pointed at Antenna Board

In the anechoic chamber, there is a turntable that can rotate 360 degrees and tilt ±45 degrees. The turntable with the antenna board attached can be seen in Figure 4.13. In order to calculate the maximum radiated power, an assembled probe was attached to the turntable and an 8.5 dBi Yagi-Uda antenna was attached to the non-reflective PVC pipe stand set-up 1.5748 meters (62 inches) away from the transmit antenna. A Tektronix spectrum analyzer was attached to the Yagi-Uda and the received power level was measured and can be seen in Table 4.2. The maximum received power level was used to calculate the efficiency of the antenna. Due to the compact nature of the designed antenna board, the feed-matching structure to couple the antenna to the microcontroller was very compact and had multiple bends along the feed path. In order to calibrate the loss of the feed structure, the ISM band antenna from the antenna board was connected directly to the microcontroller development kit which has an optimized feed structure. Finally, a function generator was directly connected to the ISM band antenna and the received power level was recorded.
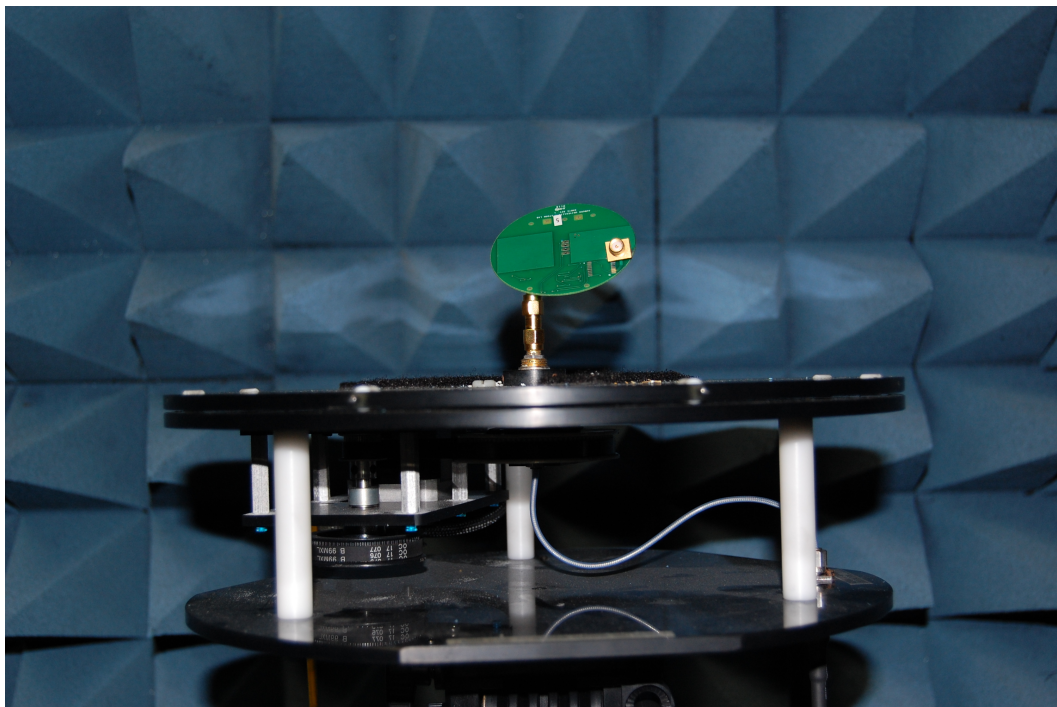
Figure 4.13: Antenna Board on Turn Table

Feed Type (Transmit Power 0 dBm)	Received Power Level (dBm)
eMote Probe	-43.17
Development Board	-37.21
Function Generator	-36.93

Table 4.2: Received Power Levels of the ISM Band Antenna

From the received power measurements, the quality of the feed structure can be analyzed. The non-ideal feed structure of antenna board causes approximately 7.5 dBm loss (including the 1.5 dB of insertion loss from connecting the antenna to the development board) which reduces the voltage delivered to the antenna by more than a factor of four. With this data, the gain of the antenna can be extracted. The free space path loss equation of an antenna system can be found using the Friis transmission equation. The equation has been modified to a convenient dBm form [14].

Equation 4.6 *Transmission Equation*

$$P_r(dBm) = P_t(dBm) + G_t(dBm) + G_r(dBm) - 20log(R(km)) - 20log(MHz) - 32.44$$

Where P_r is the received power, P_t is the transmitted power, G_t is the transmit antenna gain, and G_r is the receive antenna gain. The equation can be rearranged to calculate the gain of the transmit antenna.

Equation 4.7 *Gain of transmit antenna*

$$G_t(dBm) = P_r(dBm) - P_t(dBm) - G_r(dBm) + 20log(R(km)) + 20log(MHz) + 32.44$$

The free space path loss are the last three terms of Equation 4.6.

Equation 4.8 *Free Space Path Loss*

$$L_{fs} = 20log(R(km)) + 20log(MHz) + 32.44$$

From the above equations, the free space path loss at 902 MHz (channel 0 for the transmitter) at the range of 1.5748 meters is 35.484 dB. To calculate the gain of the antenna, Equation 4.7 is used with the received power from Table 4.2. The measurement is used where the antenna is connected directly to the function generator with 3 dB added to account for the insertion loss of the connectors. The calculated max gain of the antenna is therefore -6.94 dB. This loss correlates with the previously documented issues with the antenna board. The system gain of the entire probe can then be calculated to be approximately -16.18 dB incorporating the loss in the feed structure.

4.5   Range and Field Tests

To quantify the operational range of the probe system, a field test was completed and in-situ data were collected. For the test, the receiver base station was installed on the roof of Broun Hall and the probes were placed along a walkway on campus. The receiver base station consisted of the receiver hardware, a Texas Instruments CC1101 module, a laptop for data logging, and an 8.5 dBi gain Yagi-Uda receive antenna, which can be seen in Figure 4.14. The Yagi-Uda receive antenna was pointed down the road toward the probes as can be seen in Figure 4.15

Figure 4.14: Receiver Set-up

Figure 4.15: Receive Antenna View

To test the maximum operational range of the eMote, it was moved until the receiver was unable to reliably receive the preamble and the sync word. The maximum observed range was 260 meters. It was determined that this range could be extended and still allow the reception of good data packets if the sync word quality was lowered or if the sync word and the preamble utilized an encoding scheme to decrease the issues with signal-to-noise ratio. The data packets that are transmitted after the preamble and sync word are currently utilizing a forward error correction, FEC, encoding scheme, but due to time constraints the team was not able to implement an encoding scheme on the preamble or sync word as this would require a major revision of the receiver and transmitter firmware. A FEC encoding scheme was chosen as it has been well proven to improve the signal-to-noise ratio [60, 61]. During this test, every data packet that was received after a correct sync word and preamble contained valid data; therefore the data packets could be transmitted over a much longer range with only a small percentage of bad packet data that could easily be filtered out in the post-processing of the data.

4.5.1 Field Testing October 11

After a range test was completed, three eMotes were placed along a 145 meter path and the data were collected for several hours. In Figure 4.16 the received data are plotted. The probes were started around 9 am on October 11 and were stopped around 5 pm. Probe 1 failed early in the testing phase as it was poorly mounted and the antenna shifted and was no longer pointed at the receiver station. Probe 2 became intermittent and it is believed there was an issue with the sensor board on the probe that caused it to enter an error state and not transmit data to the receiver station. Probe 2 also shows higher temperatures than the other probes as it was placed on a brick structure in the sun. This placement could have also caused the microcontroller to overheat as after reaching a high maximum temperature around noon the probe stops collected data until around 3 pm. The increased temperature of the probes placed in direct sunlight is due to solar radiative heating errors [62]. The probe locations can be seen in Figure 4.19. Probe 3 was placed closest to the receiver and was robustly mounted in partial shade, therefore it had the most consistent data transfer.
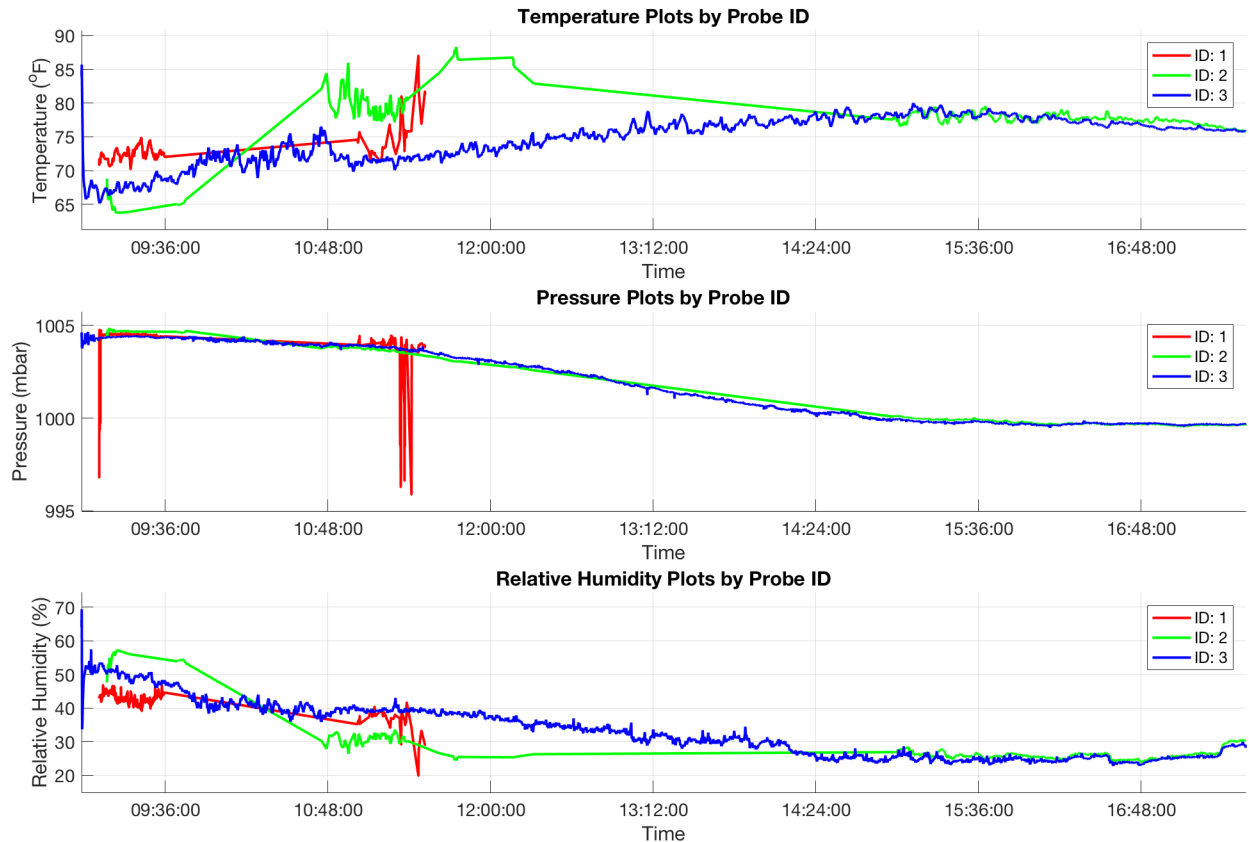
Figure 4.16: Plot of Probe Data Test Day 1

4.5.2 Field Testing October 12

A second day was spent on range testing the probes and collecting the data. Steps were taken to improve the mounting of the probes to increase the consistency of the data transfer so they were mounted on tripods similar to the receiver in Figure 4.14. The sync word and preamble quality was also slightly lowered in order to increase the range of the eMotes. A range test was performed on the probes and the range was increased from 260 meters to 505 meters. After the range testing, three probes were set-up along a 160 meter path as can be seen in Figure 4.19. The data collection phase of the test started at approximately 10 am and concluded at approximately 9 pm and the data can be seen in Figure 4.17. Probes 2 and 3 were in direct sunlight and wind for most of the day so they show higher temperatures. The perturbations in the temperature data are due to the wind and occasional cloud coverage.

Probe 1 shows the most accurate data as it was placed in full shade and had some wind protection. All the probes' data closely correlates after sunset. The data recorded by Probe 1 matches weather forecasts and measurements made by local weather stations.
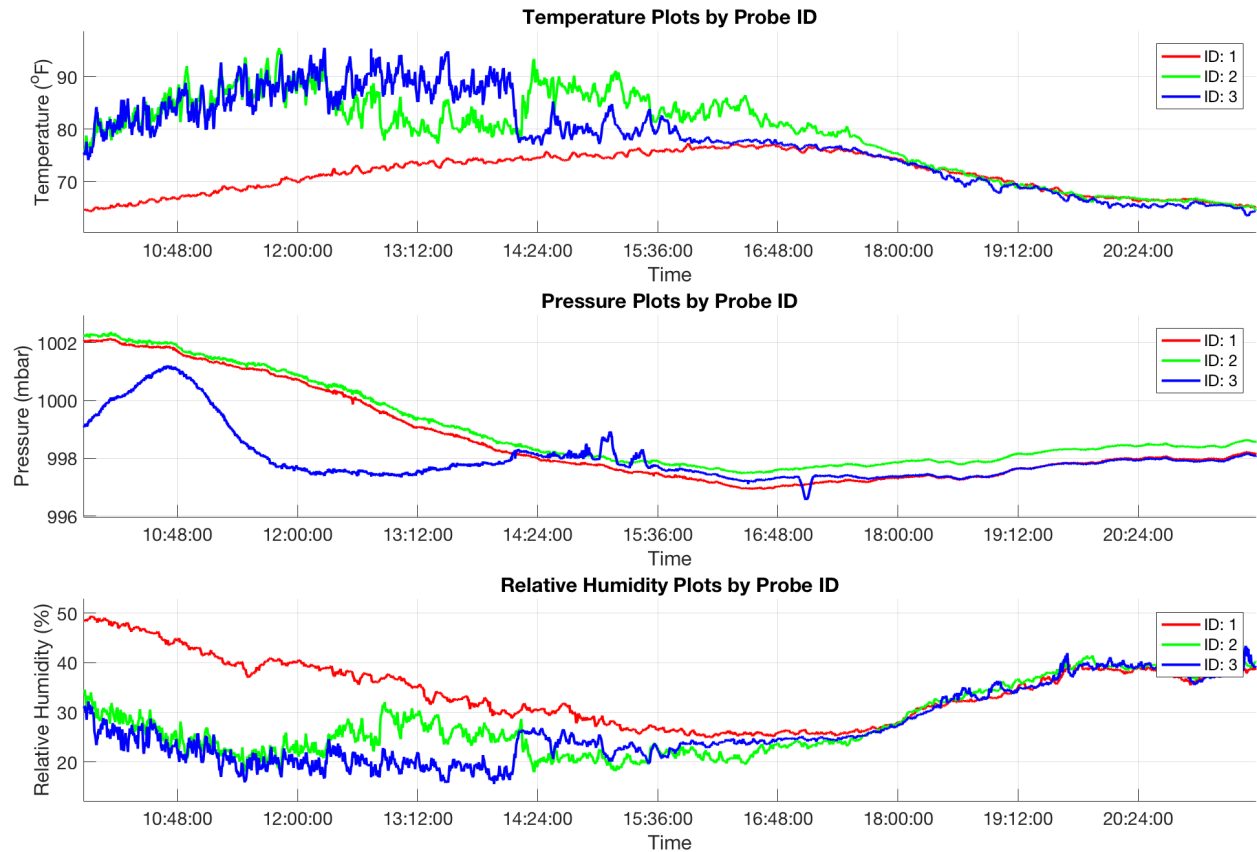

Figure 4.17: Plot of Probe Data Test Day 2

4.5.3   Field Testing October 13

For the final day of field testing, a fourth probe was added. The probes were spaced further apart; Probe 1 was 335 meters from the probe station and the other three probes were placed along the 335 meter path as can be seen in Figure 4.19. The probes were further spaced and two were placed in full to partial shade to further verify the correct operation of the probes. Measurements were taken for a longer period of approximately 9 am October 13 to 2 am October 14 as can be seen in Figure 4.18. Probe 4 was placed in full shade and Probe 1 was placed in partial shade. The data from Probe 1 aligned closely with weather

measurements made by local weather stations. Probes 2 and 3 were placed in the sun which lead to some variance in the temperature and humidity measurements. All the probes' data closely correlate after sunset.
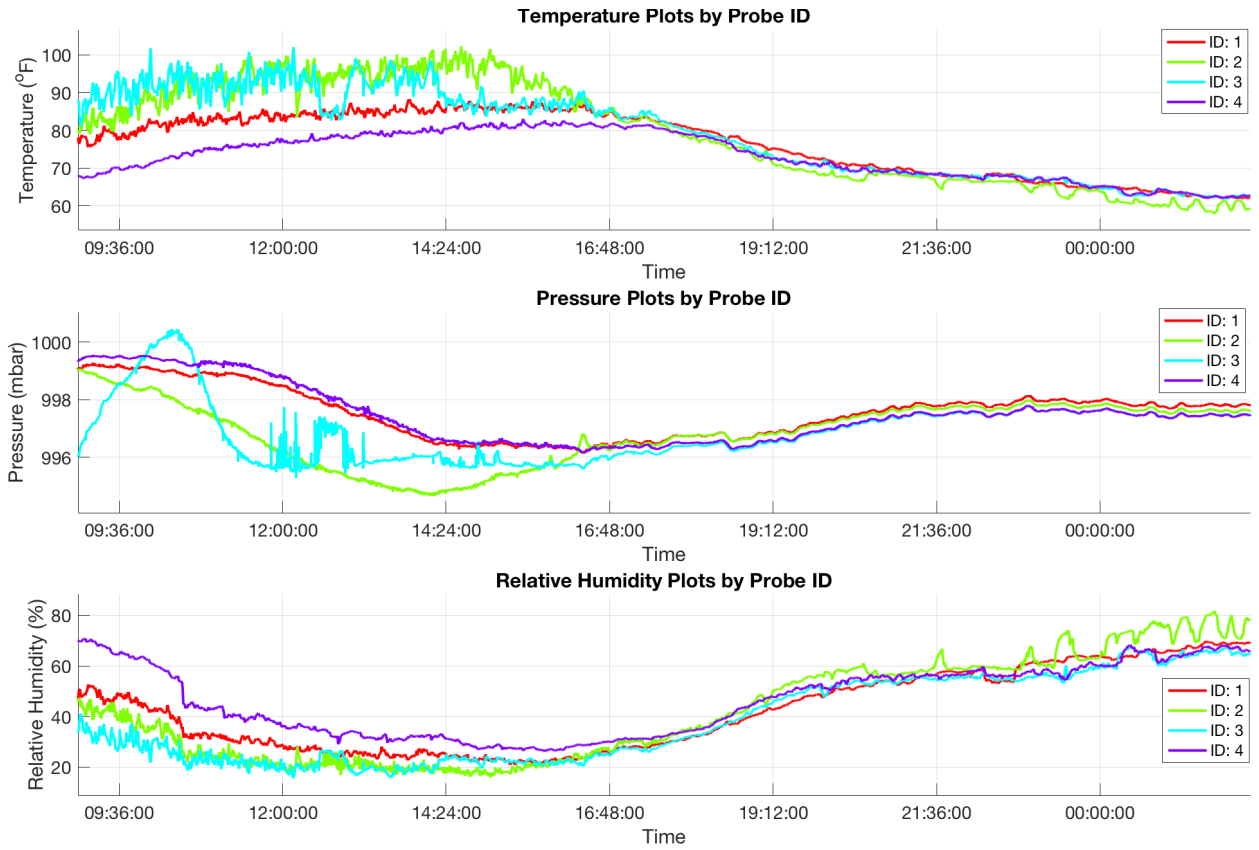
Figure 4.18: Plot of Probe Data Test Day 3
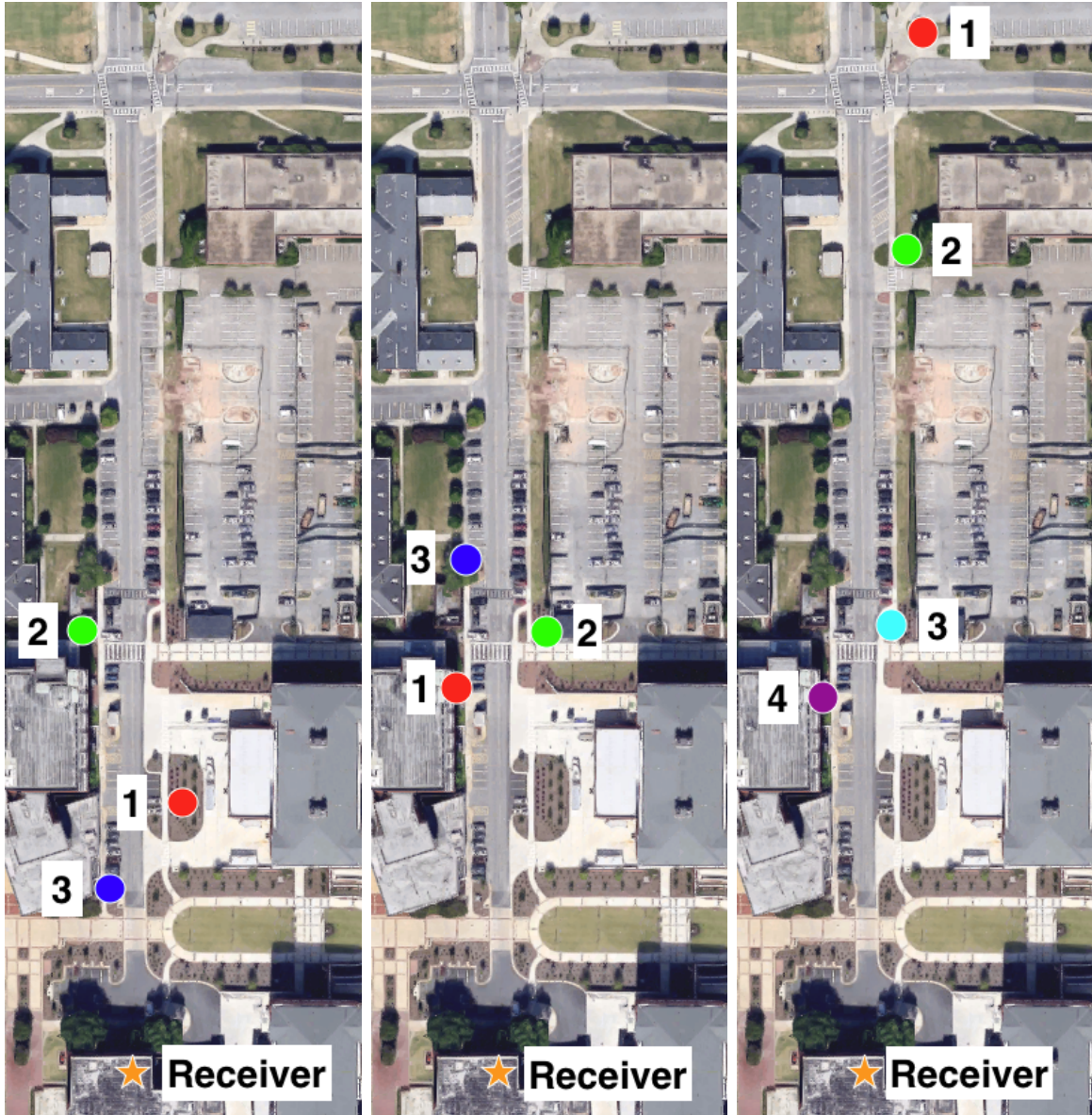
Figure 4.19: Location of the Probes on Oct 11 (a) Oct 12 (b) Oct 13 (c)

During the range testing, the GPS systems were not tested. The GPS antennas are designed to be integrated with a ublox MAX-M8 receiver. Unfortunately, there is currently an issue with the integration of the GPS receiver on the antenna board that is either a software issue, assembly issue, or board layout issue. This issue is currently being researched, but will not be solved before the submission of this thesis.

Chapter 5

Conclusions and Future Work

In this thesis, the design and characterization of dual antennas for a novel airborne probe has been presented. While the antennas did not operate as well as desired, future work will be completed to address these concerns. The antennas were designed to fit on a compact, circular FR-4 printed circuit board.

At the onset, a thorough investigation of the commercial off-the-shelf antennas and state-of-the-art in antenna research was completed. This investigation demonstrated that a custom design would be needed for the Global Sense eMote system. The initial design attempted to create a circularly polarized GPS L1 band, 1.563 – 1.587 GHz, antenna based off of the design by Chen [37]. This design was thoroughly simulated and modified to radiate at the GPS L1 band. The industrial, scientific, and medical band, 902 – 928 MHz, antenna was designed based on the linearly polarized planar inverted-F antenna. The antenna was modified to operate on a circular substrate with an irregular ground plane. The preliminary design required a large, 70 mm diameter 1.6 mm thick, FR-4 printed circuit board that would have weighed approximately 11.39 grams, which exceeded the target of 5 grams. Due to the low radiation efficiency of the circularly polarized GPS L1 band antenna and large size of the antenna board, the first design was deemed inadequate for the eMote system.

Further design work focused on decreasing the mass of the eMote antenna board. In order to reduce the mass of the antenna board, the GPS L1 band antenna was transitioned to a linearly polarized planar inverted-F antenna. Transitioning to the planar inverted-F antenna permitted a reduction in the thickness of the antenna board to 0.8 mm. This reduced the mass of the antenna board by 50 percent. Then the diameter of the antenna board was decreased to 60 mm, thereby reducing the mass by an additional 26.5 percent to

approximately 4.2 grams meeting the desired target of less than 5 grams. The two antennas were designed and simulated, utilizing ANSYS Electronics Desktop, to operate in the ISM and GPS L1 bands on the circular substrate. The design was then replicated in board layout software, Cadence Allegro PCB Editor, and the design files were sent to a boardhouse, Advanced Circuits, for fabrication.

The eMote boards were then populated and tested. The testing data showed the antenna boards did not operate as designed. Tests were then completed to determine the cause of the discrepancies. Following the methods presented by Fulford and Wentworth [54], the permittivity of the substrate was extracted. This process demonstrated that the substrate did not have the permittivity that was simulated. Following this, it was found that there were a few errors in the layout of the antennas that occurred during the board layout process. Finally, the perturbations in the high frequency ground plane caused by the DC ground plane connections effectively meandered the ground plane and decreased the radiation frequency. These three issues were responsible for the discrepancies in the radiation characteristics of the antennas.

The final testing of the eMotes were system tests. The fabricated and assembled eMotes were tested around campus for operational range. The max operational range achieved was approximately 500 meters. eMote range will be increased through firmware by reducing the baud rate and required sync word quality, and through hardware by increasing the transmit power in future iterations. Design improvements of the antennas will also increase the effective eMote range.

Future work will focus on minimizing the mass and increasing the range of the eMote by creating a dual band antenna. Another major change to the current design of the probe will be moving all of the active and passive components to the stem of the eMote which should mitigate potential issues with electromagnetic compatibility. Since the components will be moved to the stem board, it will be easier to prevent unintentional meanders of the conductors which caused an issue in the current design. This redesign will also address

mechanical concerns with the eMote. In the current eMote design, the weakest point is the interconnection between the cap and stem PCBs. The new design will utilize a flexible RF cable or substrate instead of a solid connector between the stem and cap boards. This will also lower the center of gravity which should improve the stability of the probes while falling and allow the creation of additional drag enhancing structures. The future design of the stem board will also provide more space for the matching network which should minimize the loss across the feed path. The dual antenna design will additionally necessitate the design of a compact, lightweight circulator or diplexer.

Another primary revision in future designs will be to change of the substrate type. For future design iterations there will be an enhanced effort to test and verify the dielectric properties of the substrates prior to fabrication and design. Substrates will also be used that are specifically designed for high frequency operations which have a more stringent quality control for dielectric substrates and planarity. The new substrate will most likely be a Rogers RT/Duriod or similar type of substrate.

In future efforts, a method will be found to easily transfer designs between ANSYS HFSS and Cadence Allegro PCB Editor. The ability to integrate the design programs will allow high frequency simulations of the entire device instead of just the antennas. Also, the integration between the two software packages will help prevent inconsistencies of the antenna boards during the layout phase of the design. Finally, additional work will be completed on the software and integration. Work will be completed to lower the signal-to-noise ratio on the sync word and preamble to increase the effective operational range of the eMote probes along with increasing the transmit power of the eMotes.

Bibliography

[1] Vaisala. Vaisala dropsonde rd94, 2010.

[2] Murty Divakarla, Christopher Barnet, Mitchell Goldberg, Eric Maddy, Walter Wolf, Lawrence Flyn, Xiaozhen Xiong, Jennifer Wei, Lihang Zhou, and Xingpin Liu. Validation of atmospheric infrared sounder temperature and water vapor retrievals with matched radiosonde measurements and forecasts. *Journal of Geophysical Research*, 111(D9), 2006.

[3] John Manobianco. Global environmental mems sensors (gems): A revolutionary observing system for the 21st century. *NOAA SBIR Phase I Final Report.*, 2002.

[4] John Manobianco. Global environmental mems sensors (gems): A revolutionary observing system for the 21st century. *Phase II Final Report.*, 2005.

[5] ANSYS HFSS v15, 2015. http://www.ansys.com/Products/Electronics/ANSYS-HFSS.

[6] ANSYS Electronics Desktop, 2016. http://www.ansys.com/Products/Electronics/ANSYS-Electronics-Desktop.

[7] LPKF Laser and Electronics. Lpkf protomat s62 a new generation of advanced circuit board plotters. http://www.lpkfusa.com/datasheets/prototyping/s62.pdf.

[8] Keysight. Keysight technologies fieldfox handheld analyzers. http://literature.cdn.keysight.com/litweb/pdf/5990-9783EN.pdf?id=2210837.

[9] Tektronix. Rsa306b usb real time spectrum analyzer datasheet. http://www.tek.com/datasheet/rsa306b-usb-real-time-spectrum-analyzer-0.

[10] Stuart Wentworth. *Applied Electromagnetics: Early Transmission Lines Approach*. Wiley, Hoboken, NJ, 2007.

[11] John Arthur. The fundamentals of electromagnetic theory revisited. *IEEE Antennas and Propagation Magazine*, 50(1):19–65, 2008.

[12] Umran S Inan, Aziz S Inan, and Ryan K Said. *Engineering Electromagnetics and Waves*. Prentice Hall, 2nd edition, 2015.

[13] David M. Pozar. *Microwave Engineering*. Wiley, New York, 4th edition, 2012.

[14] W. L. Stutzman and G. A. Thiele. *Antenna Theory and Design*. John Wiley and Sons, Inc., 3rd edition, 2013.

[15] D. Rialet, A. Sharaiha, A. C. Tarot, and C. Delaveaud. Characterization of antennas on dielectric and magnetic substrates effective medium approximation. In *2009 3rd European Conference on Antennas and Propagation*, pages 3163–3166, March 2009.

[16] Keysight's momentum 3d planar em simulator, Version 2015. http://www.keysight.com/en/pc-1887116/momentum-3d-planar-em-simulator?nid=-33748.0&cc=US&lc=eng.

[17] Interface Specification IS-GPS-200H. Technical report, United States. Global Positioning Systems Directorate. Systems Engineering and Integration, 2013.

[18] Interface Specification IS-GPS-705 Revision d. Technical report, United States. Global Positioning Systems Directorate. Systems Engineering and Integration, September 2013.

[19] J. Garcia, A. Arriola, F. Casado, X. Chen, J. I. Sancho, and D. Valderas. Coverage and read range comparison of linearly and circularly polarised radio frequency identification ultra-high frequency tag antennas. *IET Microwaves, Antennas Propagation*, 6(9):1070–1078, June 2012.

[20] Joe Dichoso. FCC Basics of Unlicensed Transmitters. Technical report, Federal Communications Commission Office of Engineering Technology Laboratory Division, October 2007.

[21] Understanding the FCC Regulations for Low-Power, Non-Licensed Transmitters. Technical report, Office of Engineering and Technology Federal Communications Commission, February 1996.

[22] Y. T. Lo and S. W. Lee, editors. *Antenna Handbook*, volume 2. Van Nostrand Reinhold, New York, 1993.

[23] Kin-Lu Wong, editor. *Compact and Broadband Microstrip Antennas*. John Wiley and Sons, New York, 2002.

[24] D. H. Smithgall and G. A. Wright. Quarter wave patch antenna, November 30 1999. US Patent 5,995,048.

[25] H. Iwasaki. A circularly polarized small-size microstrip antenna with a cross slot. *IEEE Transactions on Antennas and Propagation*, 44(10):1399–1401, Oct 1996.

[26] P. Sharma and K. Gupta. Analysis and optimized design of single feed circularly polarized microstrip antennas. *IEEE Transactions on Antennas and Propagation*, 31(6):949–955, Nov 1983.

[27] Chih-Yu Huang, Jian-Yi Wu, and Kin-Lu Wong. Cross-slot-coupled microstrip antenna and dielectric resonator antenna for circular polarization. *IEEE Transactions on Antennas and Propagation*, 47(4):605–609, Apr 1999.

[28] C. W. Su and J. S. Row. Slot-coupled microstrip antenna for broadband circular polarisation. *Electronics Letters*, 42(6):318–319, March 2006.

[29] X. L. Bao and M. J. Ammann. Dual-frequency circularly-polarized patch antenna with compact size and small frequency ratio. *IEEE Transactions on Antennas and Propagation*, 55(7):2104–2107, July 2007.

[30] F. Ferrero, C. Luxey, G. Jacquemod, and R. Staraj. Dual-band circularly polarized microstrip antenna for satellite applications. *IEEE Antennas and Wireless Propagation Letters*, 4:13–15, June 2005.

[31] Adam Z. Narbudowicz. *Advanced Circularly Polarised Microstrip Patch Antennas*. PhD thesis, Dublin Institute of Technology, 2013.

[32] Upadhyaya N. Rijal, Junping Geng, Xianling Liang, Ronghong Jin, Xiang Liu, and Kun Wang. Study on the planar circularly polarized antennas with swastika slot. *Progress In Electromagnetics Research C*, 39:11–24, 2013.

[33] N. C. Karmakar and M. E. Bialkowski. Circularly polarized aperture-coupled circular microstrip patch antennas for l-band applications. *IEEE Transactions on Antennas and Propagation*, 47(5):933–940, May 1999.

[34] D. M. Pozar and S. M. Duffy. A dual-band circularly polarized aperture-coupled stacked microstrip antenna for global positioning satellite. *IEEE Transactions on Antennas and Propagation*, 45(11):1618–1625, Nov 1997.

[35] Fa-Shian Chang, Kin-Lu Wong, and Tzung-Wern Chiou. Low-cost broadband circularly polarized patch antenna. *IEEE Transactions on Antennas and Propagation*, 51(10):3006–3009, Oct 2003.

[36] J. W. Baik, T. H. Lee, S. Pyo, S. M. Han, J. Jeong, and Y. S. Kim. Broadband circularly polarized crossed dipole with parasitic loop resonators and its arrays. *IEEE Transactions on Antennas and Propagation*, 59(1):80–88, Jan 2011.

[37] Wen-Shyang Chen, Kin-Lu Wong, and Chun-Kun Wu. Inset microstripline-fed circularly polarized microstrip antennas. *IEEE Transactions on Antennas and Propagation*, 48(8):1253–1254, Aug 2000.

[38] A. Petosa, N. Simons, R. Siushansian, A. Ittipiboon, and M. Cuhaci. Design and analysis of multisegment dielectric resonator antennas. *IEEE Transactions on Antennas and Propagation*, 48(5):738–742, May 2000.

[39] B. Mukherjee, P. Patel, and J. Mukherjee. Hemispherical dielectric resonator antenna based on apollonian gasket of circles - a fractal approach. *IEEE Transactions on Antennas and Propagation*, 62(1):40–47, Jan 2014.

[40] K. L. Wong and C. H. Chang. Printed $\lambda/8$-pifa for internal penta-band mobile phone antenna. In *2009 3rd European Conference on Antennas and Propagation*, pages 533–537, March 2009.

[41] C. R. Rowell and R. D. Murch. A capacitively loaded pifa for compact mobile telephone handsets. *IEEE Transactions on Antennas and Propagation*, 45(5):837–842, May 1997.

[42] A. Cabedo, J. Anguera, C. Picher, M. Ribo, and C. Puente. Multiband handset antenna combining a pifa, slots, and ground plane modes. *IEEE Transactions on Antennas and Propagation*, 57(9):2526–2533, Sept 2009.

[43] D. M. Nashaat, H. A. Elsadek, and H. Ghali. Single feed compact quad-band pifa antenna for wireless communication applications. *IEEE Transactions on Antennas and Propagation*, 53(8):2631–2635, Aug 2005.

[44] R. Feick, H. Carrasco, M. Olmos, and H. D. Hristov. Pifa input bandwidth enhancement by changing feed plate silhouette. *Electronics Letters*, 40(15):921–922, July 2004.

[45] K. L. Virga and Y. Rahmat-Samii. Low-profile enhanced-bandwidth pifa antennas for wireless communications packaging. *IEEE Transactions on Microwave Theory and Techniques*, 45(10):1879–1888, Oct 1997.

[46] Yves-Thierry Jean-Charles, Vichate Ungvichian, and Juciana A. Barbosa. Effects of substrate permittivity on planar inverted-f antenna performances. *Journal of Computers*, 4(7):610–614, July 2009.

[47] Hassan Tariq Chatta, Yi Huang, Muhammad Kamran Ishfaq, and Stephen J. Boyes. A comprehensive parametric study of planar inverted-f antenna. *Wireless Engineering and Technology*, 3:1–11, January 2012.

[48] M-C Huynh and W. Stutzman. Ground plane effects on planar inverted-f antenna (pifa) performance. *IEE Proceedings - Microwaves, Antennas and Propagation*, 150(4):209–213, 2003.

[49] M. F. Abedin and M. Ali. Modifying the ground plane and its effect on planar inverted-f antennas (pifas) for mobile phone handsets. *IEEE Antennas and Wireless Propagation Letters*, 2(1):226–229, 2003.

[50] Jieh-Sen Kuo and Kin-Lu Wong. A compact microstrip antenna with meandering slots in the ground plane. *Microwave and Optical Technology Letters*, 29(2):95–97, 2001.

[51] T. Svantesson and A. Ranheim. Mutual coupling effects on the capacity of multielement antenna systems. In *Acoustics, Speech, and Signal Processing, 2001. Proceedings. (ICASSP '01). 2001 IEEE International Conference on*, volume 4, pages 2485–2488 vol.4, 2001.

[52] H. Li, J. Xiong, and S. He. A compact planar mimo antenna system of four elements with similar radiation characteristics and isolation structure. *IEEE Antennas and Wireless Propagation Letters*, 8:1107–1110, 2009.

[53] Isola Group. 370 hr data sheet. http://www.isola-group.com/wp-content/uploads/2016/04/370HR-Laminate-and-Prepreg-Data-Sheet-Isola.pdf.

[54] Andrew R. Fulford and Stuart M. Wentworth. Conductor and dielectric property extraction using microstrip tee resonators. *Microwave and Optical Technology Letters*, 47(1):14–16, October 2005.

[55] J. Carroll, M. Li, and K. Chang. New technique to measure transmission line attenuation. *IEEE Transactions on Microwave Theory and Techniques*, 43(1):219–222, Jan 1995.

[56] M. Kirschning, R.H. Jansen, and N.H.L. Koster. Accurate model for open end effect of microstrip lines. *Electronics Letters*, 17(3):123 – 125, 1981.

[57] D.H. Schrader. *Microstrip Circuit Analysis*. Prentice Hall PTR, 1995.

[58] Keysight advanced design system (ads) [computer software], Version 2015. http://www.keysight.com/find/eesof-technicalreference.

[59] C. Picher, J. Anguera, A. Cabedo, C. Puente, and S. Kahng. Multiband handset antenna using slots on the ground plane: considerations to facilitate the integration of the feeding transmission line. *Progress In Electromagnetics Research C*, 7:95–109, 2009.

[60] C. Perkins, O. Hodson, and V. Hardman. A survey of packet loss recovery techniques for streaming audio. *IEEE Network*, 12(5):40–48, Sept 1998.

[61] H.L. Wolfgang. Method for packet-level fec encoding, in which on a source packet-by-source packet basis, the error correction contributions of a source packet to a plurality of wildcard packets are computed, and the source packet is transmitted thereafter, August 19 2003. US Patent 6,609,223.

[62] Steven P. Anderson and Mark F. Baumgartner. Radiative heating errors in naturally ventilated air temperature measurements made from buoys. *Journal of Atmospheric and Oceanic Technology*, 15(1):157–173, 1998.

Appendices

A.1 Microstrip Tee Resonator MATLAB Code

```matlab
1  %T res er extract
2  %8/30/16 SMW (with Craig Prather)
3  clc;clear;
4  N=1;                %resonance number
5  c=3e8;              %speed of light, m/s
6  cin=c/.0254;        %c in in/s
7  fres=1.5396;        %res freq
8  Lin=1.06118;        %length of stub
9  dLi=.099;           %init correction length
10 dL = .099;          %correction length
11 h=31.5;             %height in mils
12 w=56;               %microstrip width, mils
13
14 while (dLi ~= dL)
15     dLi = dL
16     ee=((2*N-1)*cin/(4*fres*(Lin+dL)))^2;
17     A=sqrt(1+12*h/w);
18     er=(A*(2*ee-1)+1)/(A+1);
19     % Kirschning approach to find dL
20     % replace epsilon1 etc with e1 etc
21     e1num=0.434907*(ee^.81+0.26)*((w/h)^.8544+0.236);
22     e1den=(ee^.81-0.189)*((w/h)^0.8544+0.87);
23     e1=e1num/e1den;
24     e2=1+((w/h)^.371)/(2.358*er+1);
25     e3=1+(0.5274*atan(0.084*(w/h)^(1.9413/e2))/ee^.9236);
```

```matlab
26      e4=1+0.0377*atan(0.067*(w/h)^1.456)*(6-5*exp(.036*(1-er)));
27      e5=1-0.218*exp(-7.5*w/h);
28      dL=(h/1000)*e1*e3*e5/e4;
29  end
30  dL          %Correction  Length
31  er          %permitivitty
```

A.2 Antenna Board Measurements
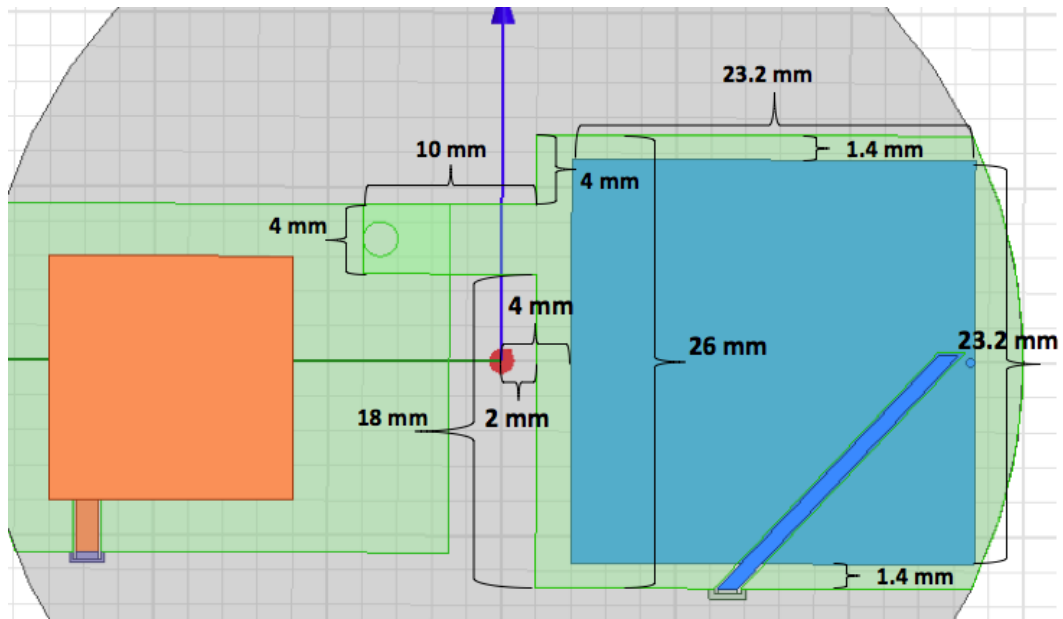
Figure A.1: Dimensions of ISM Band Patch Antenna
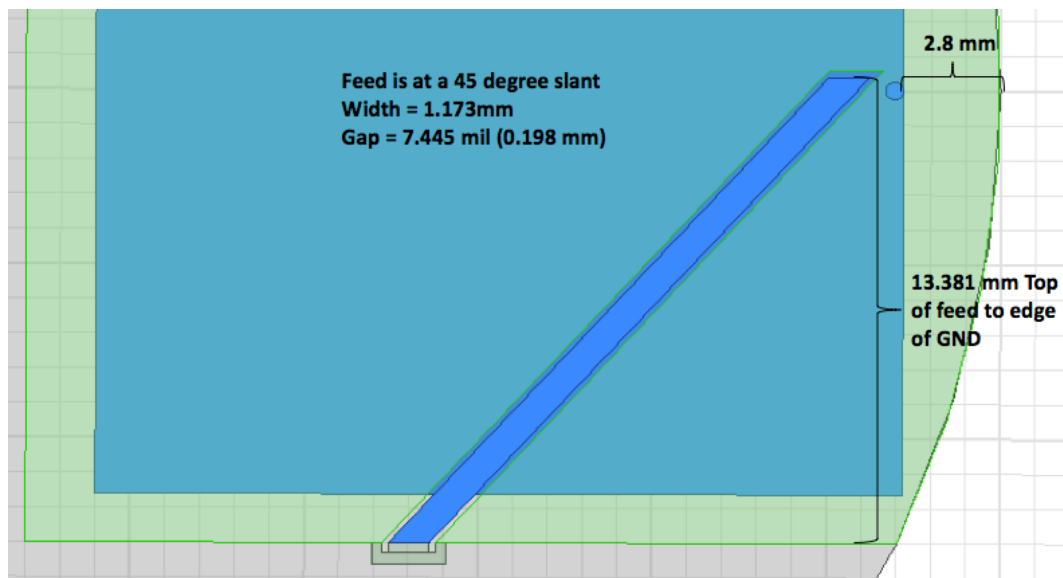
Figure A.2: Dimensions of ISM Band Patch Antenna
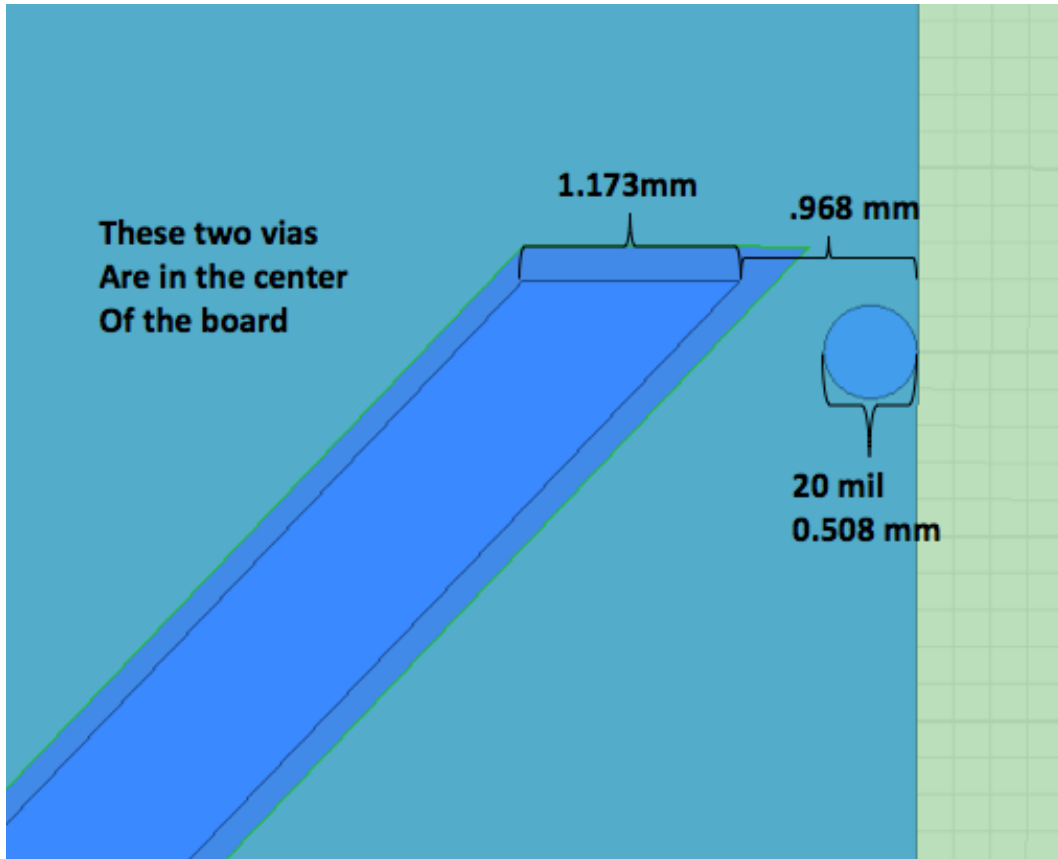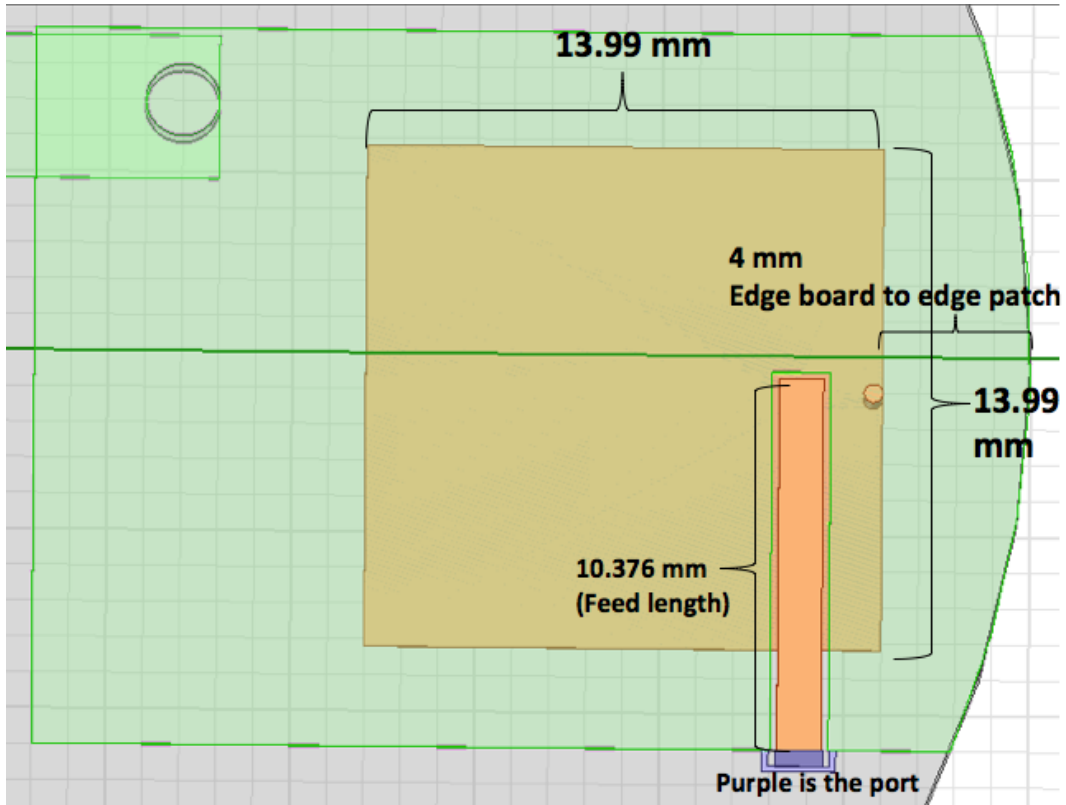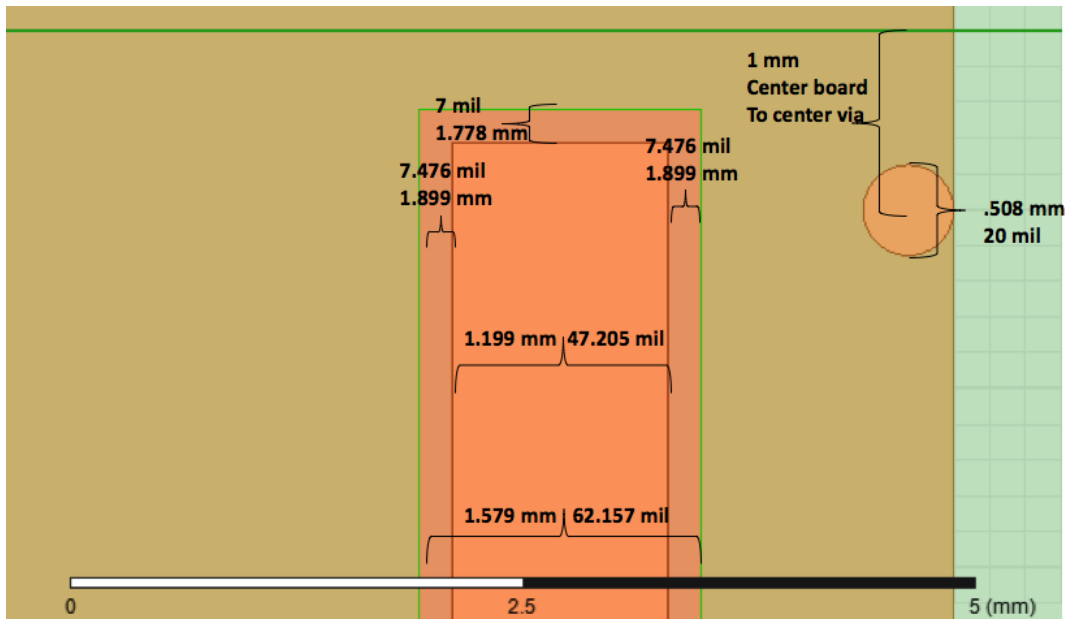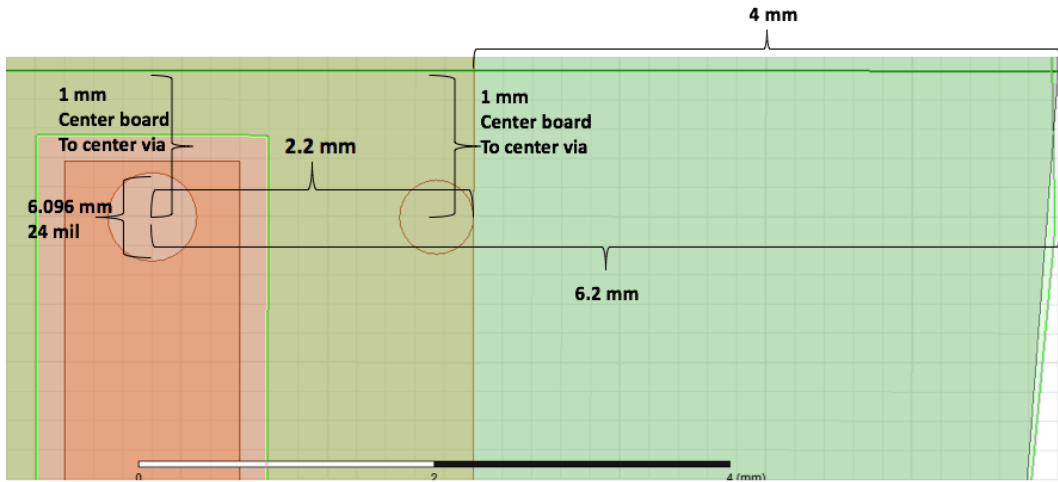
Figure A.3: Dimensions of ISM Band Patch Antenna
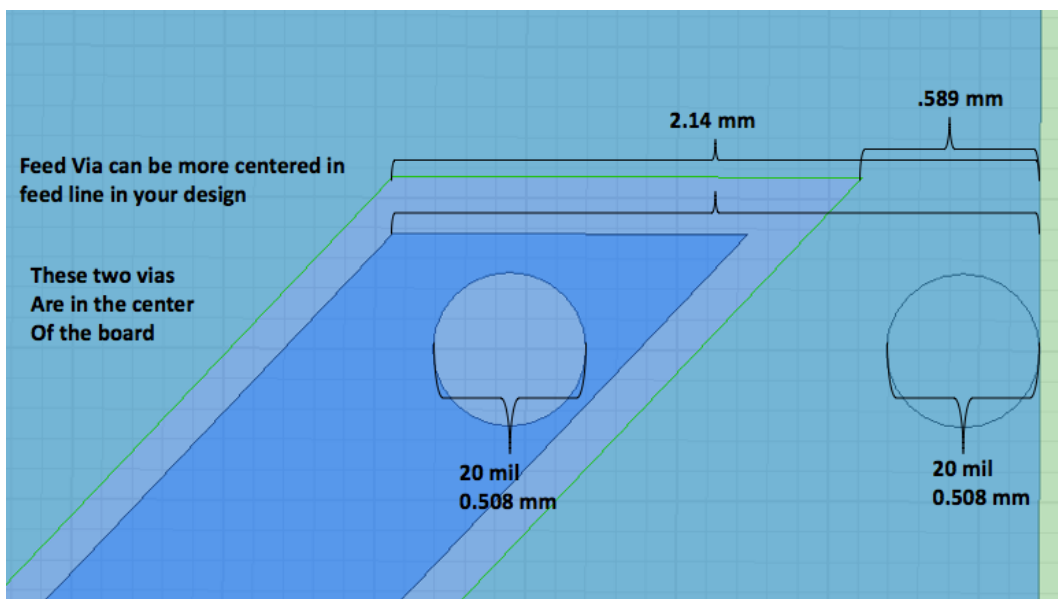
Figure A.4: Dimensions of ISM Band Patch Antenna
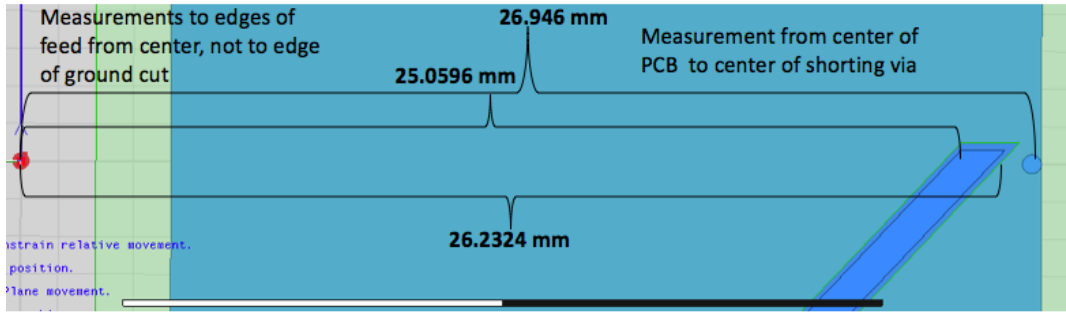
Figure A.5: Dimensions of ISM Band Patch Antenna
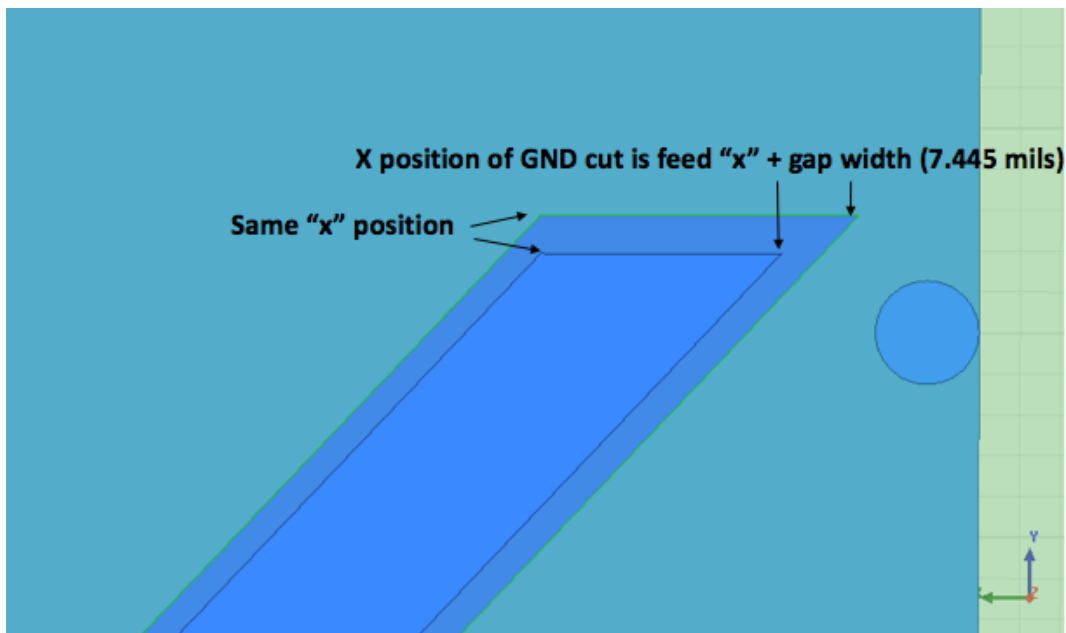
Figure A.6: Dimensions of ISM Band Patch Antenna
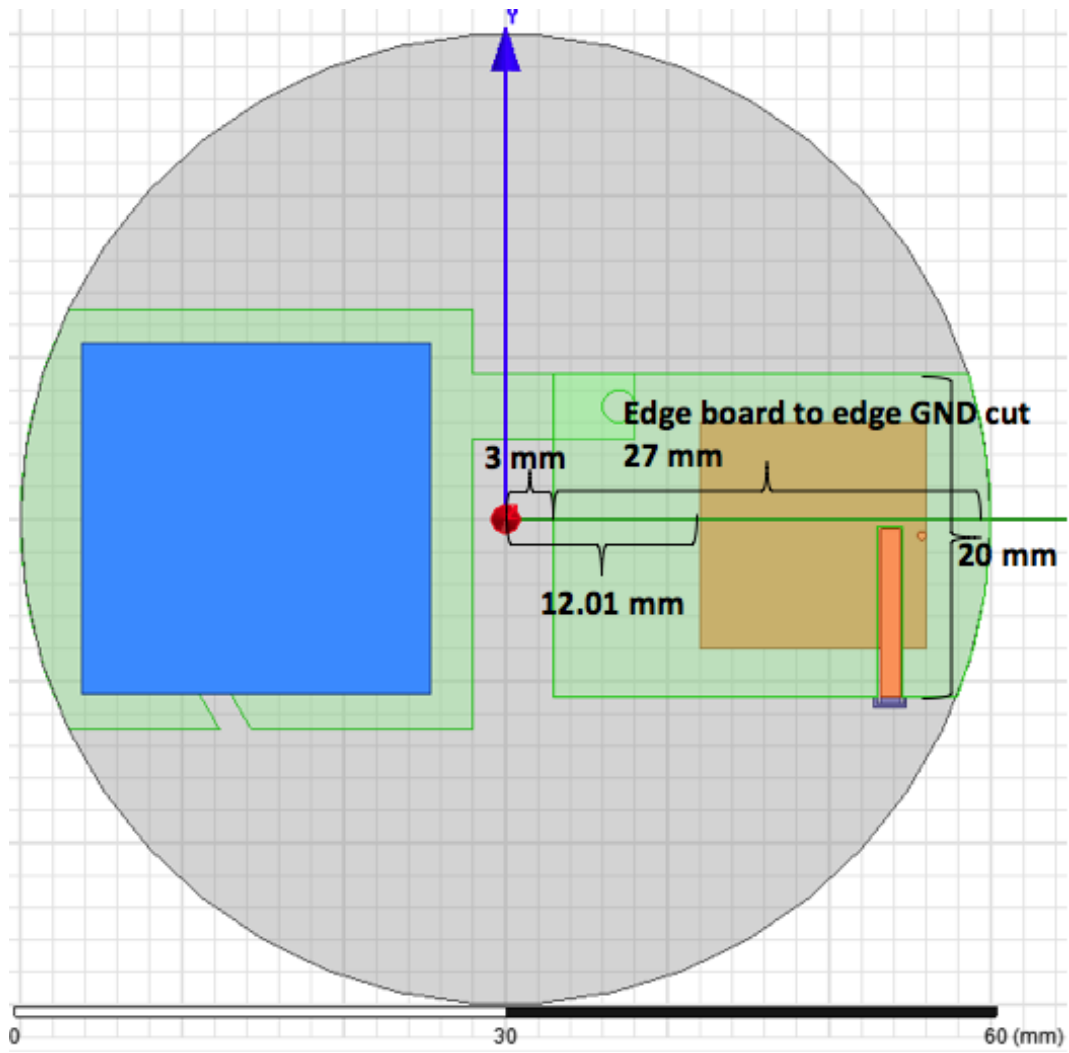
Figure A.7: Dimensions of GPS L1 Band Patch Antenna

Figure A.8: Dimensions of GPS L1 Band Patch Antenna

Figure A.9: Dimensions of GPS L1 Band Patch Antenna

Figure A.10: Dimensions of GPS L1 Band Patch Antenna

A.3   Antenna Board Test Results
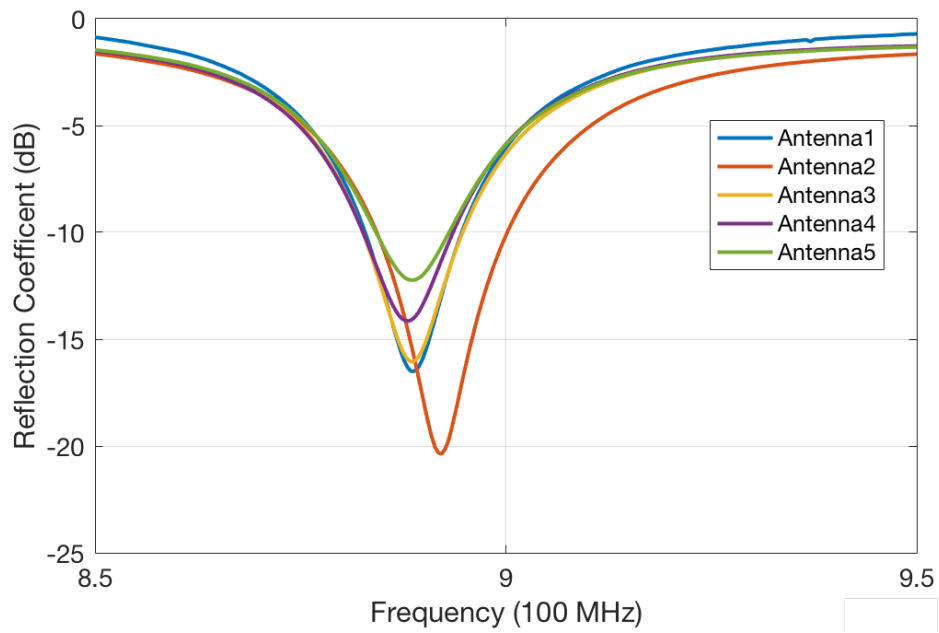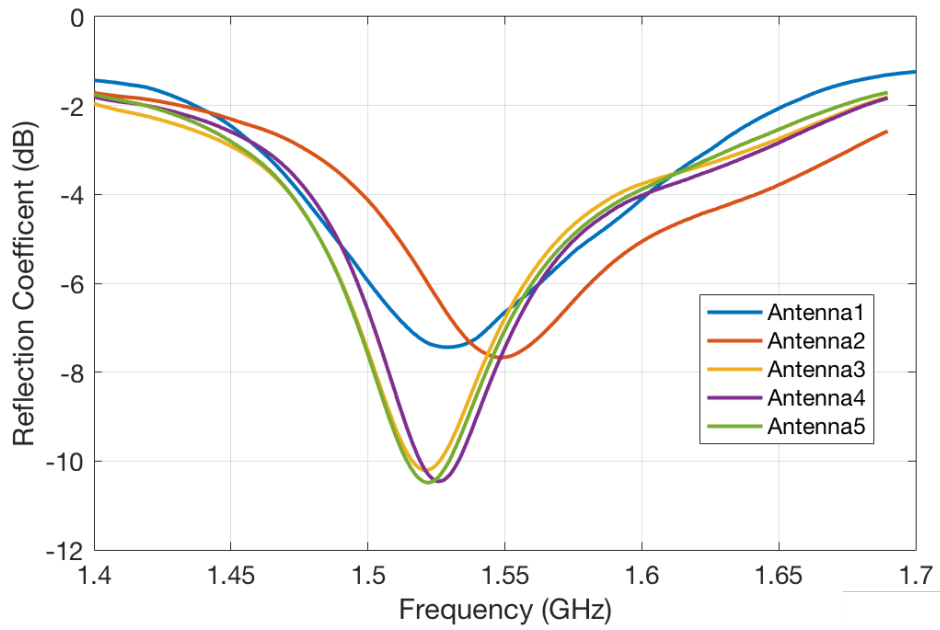

Figure A.11: Measured ISM Band S11 of the Antenna Boards
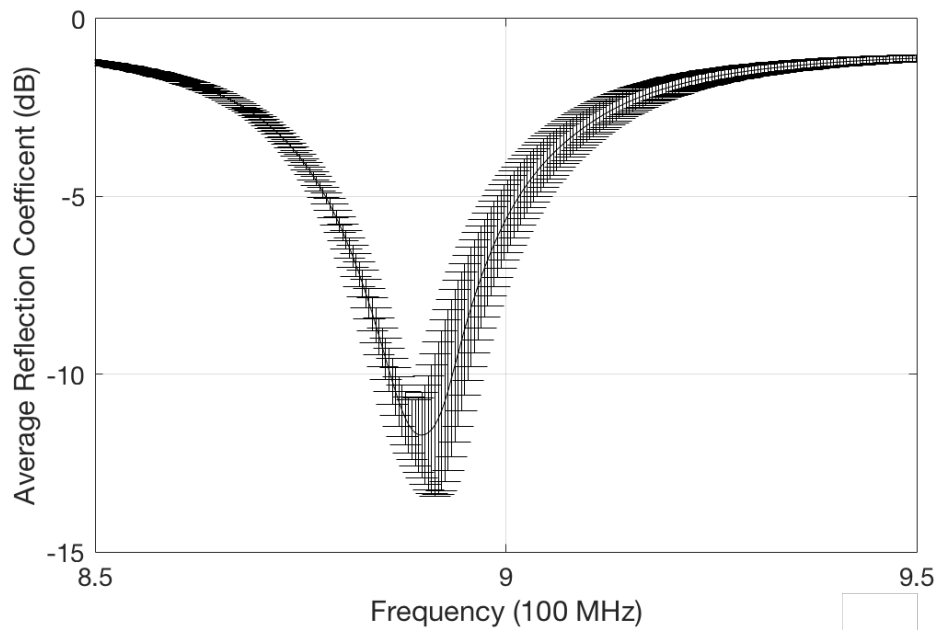
Figure A.12: Average Measured ISM Band S11 with Standard Deviation Error Bars
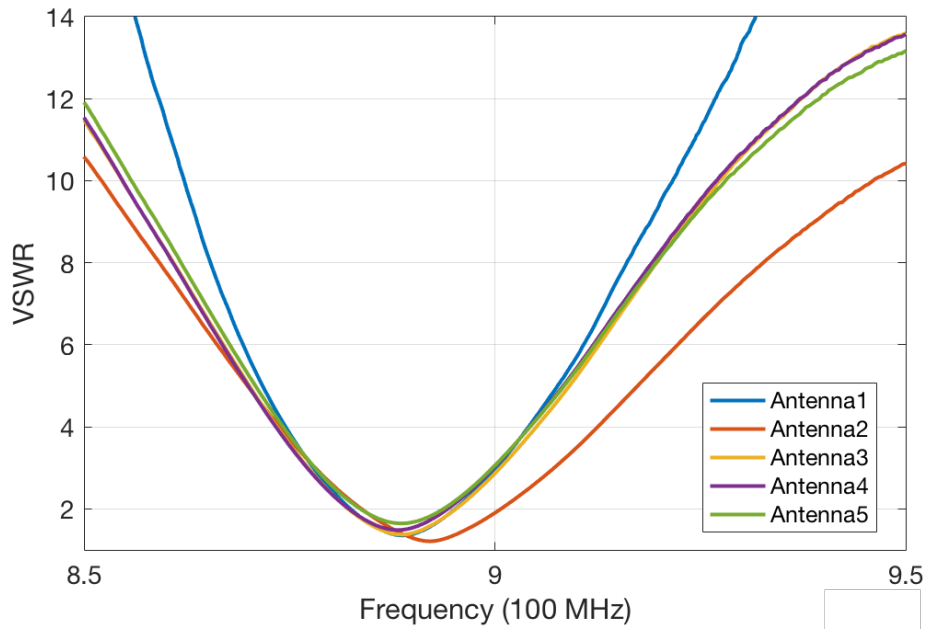
Figure A.13: Measured ISM Band VSWR of the Antenna Boards
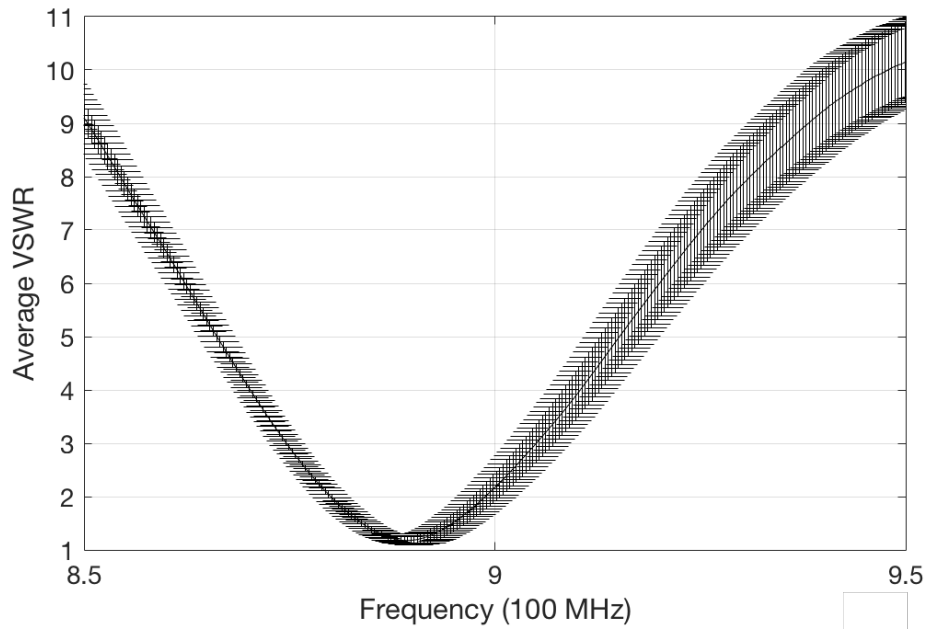
Figure A.14: Average Measured ISM Band VSWR with Standard Deviation Error Bars

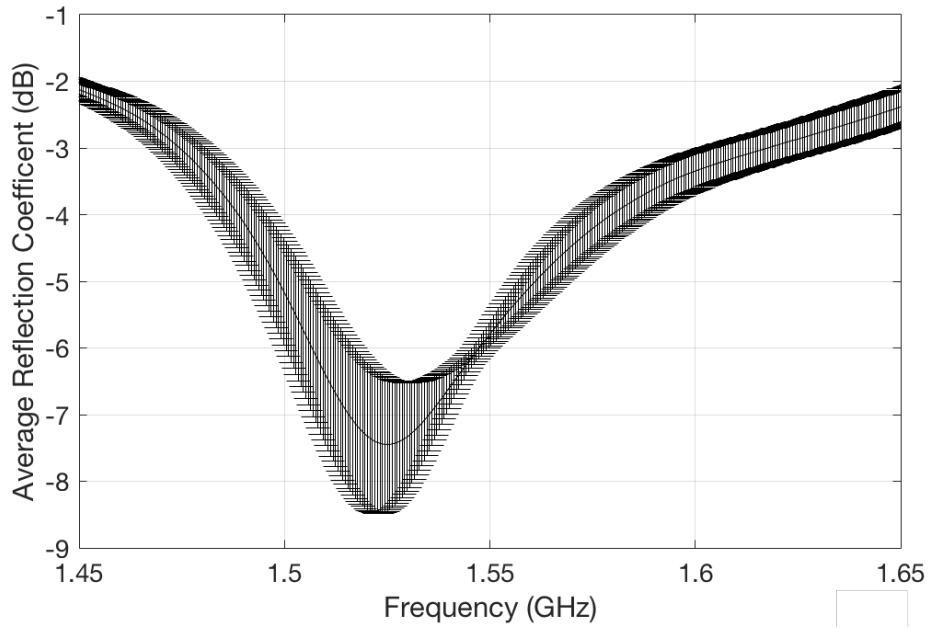Figure A.15: Measured GPS L1 Band S11 of the Antenna Boards

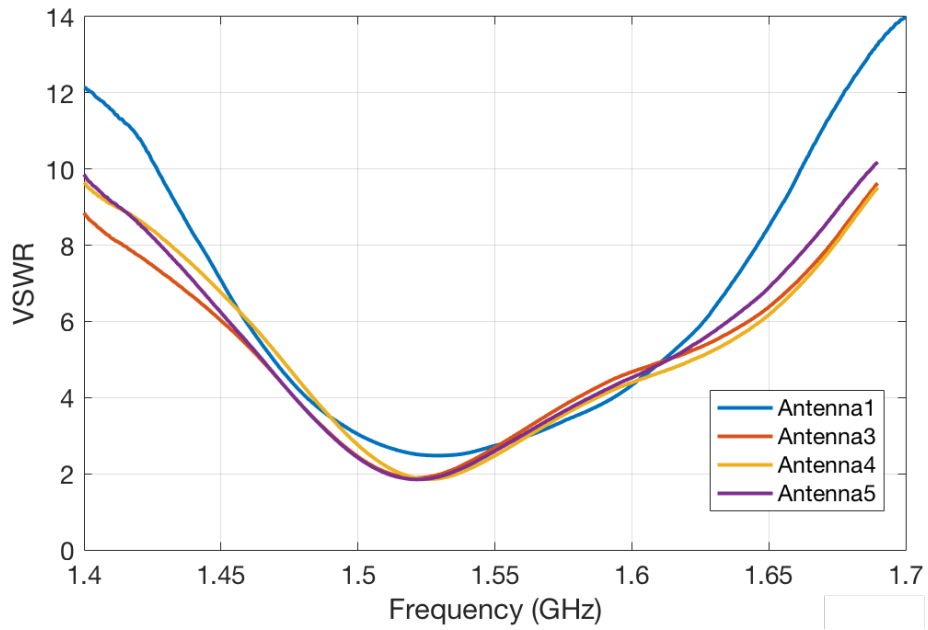Figure A.16: Average Measured GPS L1 Band S11 with Standard Deviation Error Bars

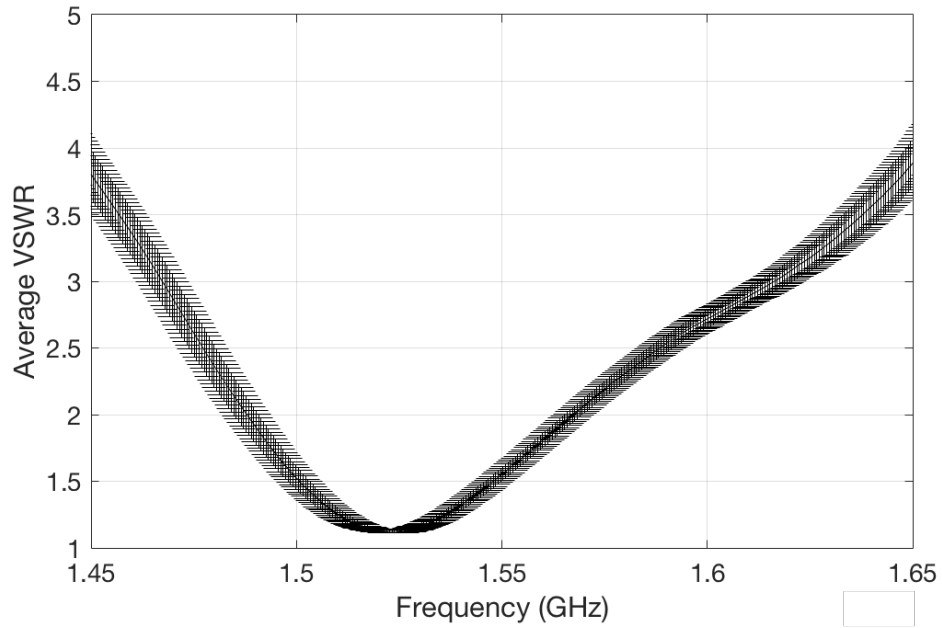Figure A.17: Measured GPS L1 Band VSWR of the Antenna Boards

Figure A.18: Average Measured GPS L1 Band VSWR with Standard Deviation Error Bars
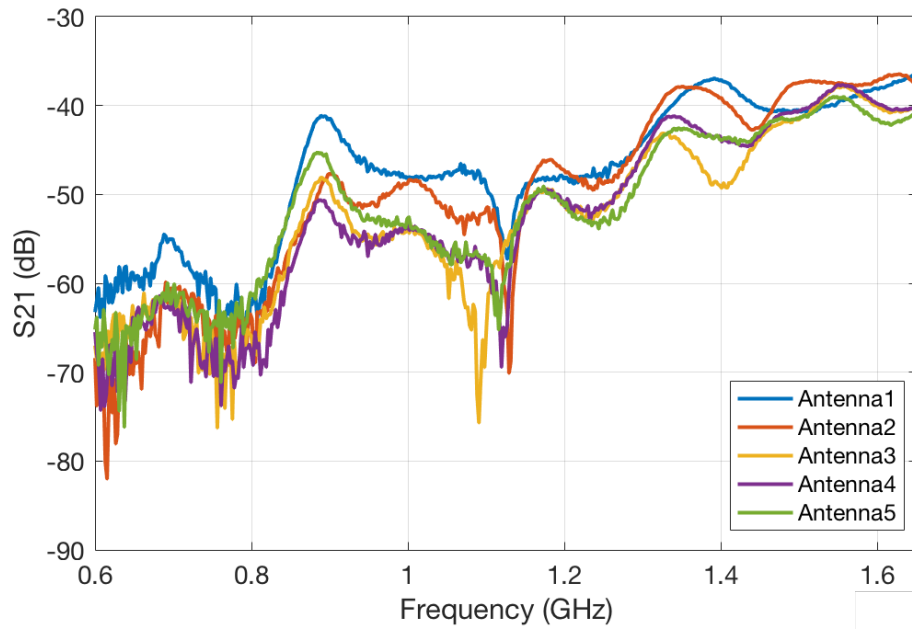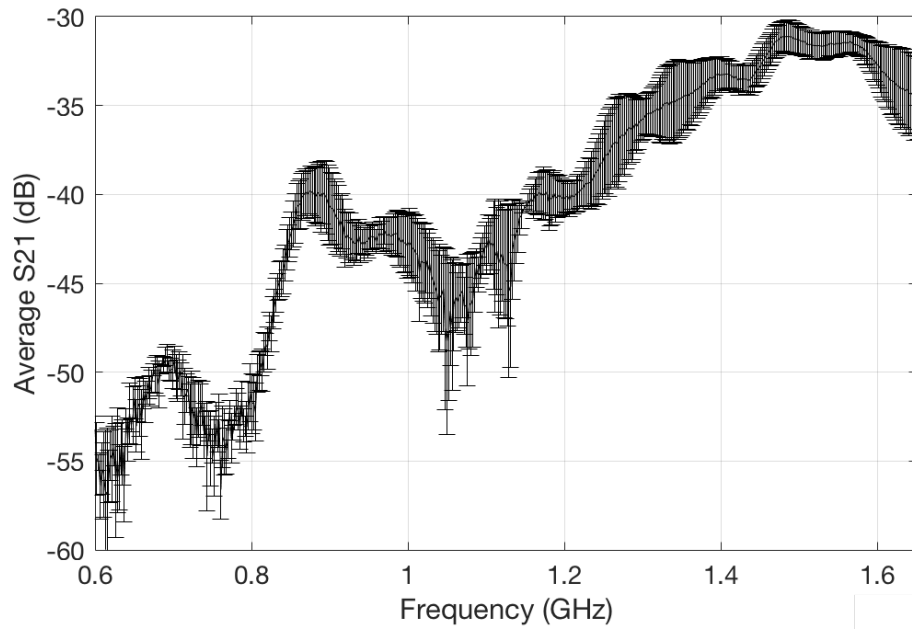
Figure A.19: Measured S21 Antenna Boards

Figure A.20: Average Measured S21 Antenna Boards with Standard Deviation Error Bars

Publications

Peer-Reviewed Journal

J. Craig Prather, Michael Bolt, Haley Harrell, John Manobianco, and Mark L. Adams. Antenna Design for a Massive Multiple Input Environmental Sensor Network. Digital Communications and Networks, 2016. (Accepted)

Conference Proceedings

J. Craig Prather, Michael Bolt, Brent Bottenfield, Thaddeus Roppel, Stuart Wentworth, and Mark L. Adams. Robotic Outreach to Attract P12 Students to Engineering. 2017 ASEE Annual Conference and Exposition. (Submitted).

Haley Harrell, J. Craig Prather, and Stuart Wentworth. Guided Design in RF Systems Lab. 2017 ASEE Annual Conference and Exposition. (Submitted).

J. Craig Prather, Haley Harrell, Lesley Bartlett, and Stuart Wentworth. Enhanced radio lab experience using eportfolios. In 2016 ASEE Annual Conference Exposition, June 2016.

Mark L. Adams, Audrey Rose Shapland, Matthew Gutierrez, Haley Harrell, Jessica Blume, and Craig Prather (2016). Enhancements of an In Situ Atmospheric System for Real Time Weather Monitoring. Additional Conferences (Device Packaging, HiTEC, HiTEN, & CICMT): January 2016, Vol. 2016, No. DPC, pp. 881–900